UCL Université catholique de Louvain

École polytechnique de Louvain (EPL)

epl

Electronic transport properties of thermoelectric Zintl compounds $Ca_5Al_2Sb_6$ and Ca_3AlSb_3

An *ab initio* study

Dissertation presented by
Grégoire THUNIS

for obtaining the Master's degree in
Physical Engineering
Option: Nanotechnology

Supervisors
Geoffroy HAUTIER, Gian-Marco RIGNANESE

Readers
Jean-Christophe CHARLIER, Pascal JACQUES

Academic year 2015-2016

Abstract

Zintl phases $Ca_5Al_2Sb_6$ and Ca_3AlSb_3 exhibit interesting thermoelectric properties in various experimental studies. These *p*-type semiconductors act indeed like phonon-glass electron-crystal materials. Their complexity (large unit cells with covalent anionic chains) leads to very low lattice thermal conductivity (0.5 W/mK) while their covalent chains lead to low electrical resistivity. In this dissertation, the electronic transport properties of these two Zintl phases are theoretically investigated using the density functional theory and the Boltzmann transport theory.

As a first step, the covalent character of the chains in both compounds is confirmed using electron density difference maps. The band structures are computed with ABINIT and are used to calculate the transport coefficients in BOLTZTRAP. Constant relaxation times of 10^{-14}s and $4 \cdot 10^{-14}$s correctly reproduce the electrical resistivity of $Ca_5Al_2Sb_6$ and Ca_3AlSb_3 at high temperature, respectively. The validity of this constant approximation is justified by the constant behaviour of the electrical resistivity in both compounds. The electron scattering mechanisms are therefore studied to understand this constant behaviour and the different doping dependences of the resistivity in both phases. Ionized impurity and acoustic phonon scattering are identified as dominant mechanisms from an experimental fitting. Unlike many other materials, the acoustic phonon contribution is small compared to the ionized impurity contribution, even at high temperature, so that they compensate each other above 650 K. It is precisely this compensation that leads to the constant electrical resistivity and therefore explains the validity of a constant relaxation time. Since acoustic phonon scattering differs the most between the two phases, it is then theoretically studied. The sound velocities (derived from computed elastic constants), the band effective masses and the deformation potential constants related to the Bardeen and Shockley model are computed. This analysis highlights the origins of the different acoustic phonon relaxation times and allows one to understand the different variations of the electrical resistivity with the doping level in $Ca_5Al_2Sb_6$ and Ca_3AlSb_3.

Finally, the anisotropy in the transport properties in $Ca_5Al_2Sb_6$ is studied and shows promising results in the direction of the covalent chains. The combination of two flat bands and a very dispersive one around the valence band edge is indeed beneficial as it leads to a large Seebeck coefficient while the electrical resistivity remains low in the direction of the light effective mass. At a doping level of $7{\cdot}10^{19}$ cm^{-3}, a figure of merit of 0.41 is reached in this direction while the average value is 0.23. These figures of merit can still be increased by tuning the doping level.

Acknowledgments

I would like to thank my supervisors Prof. Geoffroy Hautier and Prof. Gian-Marco Rignanese. Their advices and the insightful discussions we had helped me to work through this master thesis and understand the strategy of the theoretical study of materials. I would also like to thank Prof. Jean-Christophe Charlier and Prof. Pascal Jacques for reading this dissertation. Finally, I would like to thank everyone in the NAPS lab who took time to help me during these last months.

Computational resources have been provided by the supercomputing facilities of the Université catholique de Louvain (CISM/UCL) and the Consortium des Équipements de Calcul Intensif en Fédération Wallonie Bruxelles (CÉCI) funded by the Fond de la Recherche Scientifique de Belgique (F.R.S.-FNRS) under convention 2.5020.11.

Contents

List of Figures

List of Tables

Introduction

The energy requirement is growing every year in our civilization, leading to new challenges in its production. Despite this important need, almost 35% of the produced energy is wasted in heat according to the U.S. Department of Energy [1]. The search for efficient heat recovery techniques is therefore part of the energy challenge. Thermoelectric materials are interesting candidates as they are capable of transforming a heat flow into an electric flow which can then be exploited to generate electricity. In addition, thermoelectric applications are compact, noiseless and very reliable due to their solid state construction and lack of moving parts. Their main flaw is their low efficiency – less than a third of the Carnot efficiency [2].

The thermoelectric efficiency of a material is characterized by the figure of merit, which depends directly on the Seebeck coefficient and the electrical conductivity and inversely on the thermal conductivity. Its improvement is therefore tricky as the charge-carriers conductivities are linked by the Lorentz constant. However the lattice contribution to the thermal conductivity can be reduced, e.g. by using materials with complex unit cells. Jeffrey Snyder's group from the California Institute of Technology[1] is worldwide leader in the research of thermoelectric materials and their main study materials are the large and complex Zintl structures. The two Zintl compounds $Ca_5Al_2Sb_6$ and Ca_3AlSb_3 have been presented as promising candidates with figure of merit reaching 0.6 at 1000 K when correctly doped [3, 4]. A theoretical background about thermoelectricity is given in the first chapter of this thesis.

Beside experimental studies, theoretical analysis like *ab initio* calculations help to correctly understand the physics behind observed phenomena. In this thesis, the purpose was to theoretically investigate the electronic transport properties of the two Zintl compounds, more specifically the Seebeck coefficient and the electrical resistivity, using *ab initio* calculations. The second chapter is therefore a presentation of the computational theories, i.e. the density functional theory and the Boltzmann transport theory, used in this work. The two Zintl structures $Ca_5Al_2Sb_6$ and Ca_3AlSb_3 are then characterized using the density functional theory in the third and fourth chapter, respectively. The covalent character of the chains is deduced from calculated electron density difference maps. The densities of states and the electronic structures are computed and studied. The transport properties are investigated from these electronic structures using the Boltzmann transport theory in the constant relaxation time approximation as a first step. This

[1] Website of the CalTech thermoelectric research team: `http://thermoelectrics.matsci.northwestern.edu/`

approximation gave satisfying results for both compounds since the electrical conductivity is indeed constant at high temperature.

The fifth chapter goes beyond the latter approximation. The different dominant types of electron scattering – ionized impurity and acoustic phonon scattering – are identified through an experimental fitting of the electrical resistivities. This analysis highlights the compensation of these two mechanisms above 650 K, which explains the constant behaviour of the resistivity with the temperature for both compounds and therefore the validity of the constant relaxation time approximation. A theoretical investigation of the acoustic phonon scattering is done since this mechanism differs the most between the two phases. The deformation potential constants are therefore computed using a simplified Bardeen and Shockley method and the sound velocities are derived from the elastic constants using the Voigt-Reuss-Hill approximation. This analysis allows one to understand the origin of the different behaviours of the electrical resistivity with the doping level in $Ca_5Al_2Sb_6$ and Ca_3AlSb_3.

Finally, the sixth chapter investigates the anisotropy in the electronic transport properties of $Ca_5Al_2Sb_6$. In addition to the electrical resistivity and the Seebeck coefficient, the electronic and the lattice contribution to the thermal conductivity are also computed. The transport along the covalent ladders of this structure is identified as a promising option for thermoelectric application since the figure of merit is then twice its average value.

Chapter 1

Thermoelectricity

Contents

In developed countries, everyone is constantly surrounded by energy-consuming equipments. The increase in population and our growing needs lead to more energy production. From 1973 to 2013, the world total primary energy supply increased from 6100 to 13 541 MToe. Despite their well-known consequences on the environment, fossil fuels remain the main sources to produce energy – more than 70 % according to the International Energy Agency [5]. Most of the time, those fossil fuels are burned in order to generate electricity or mechanical work, which comes with many heat losses (as much as 20 to 50 % of the produced energy [1]). Thermoelectric materials are capable of transforming a heat flow induced by a temperature gradient into an electric flow or, conversely, of producing a temperature gradient by applying an electric current. The heat flow conversion into electrical power can be exploited to generate electricity while the reverse conversion allows cooling or heating applications. Those materials are therefore very interesting in the world energy challenge as they could help to recover the wasted heat, that is to say to consume less in the end.

From 1950 to 1990, the thermoelectric industry remained confined to technological niches: cooling components for electro-optics, cooling of small volumes, space applications or more. But since 1990, the energy concerns of the planet have created a new interest in thermoelectricity for recycling the heat lost by many systems. New applications have already been developed in this context. For example, researchers have already managed, in cooperation with the car manufacturer BMW, to convert into electricity the heat emitted at the exhaust of a car to power

the electronic system of the vehicle. This thermoelectric system ultimately reduces the fuel consumption of the vehicle by 5 % [6]. It is estimated that doubled-efficiency thermoelectric-modules could produce enough energy to replace the alternator. The application of thermoelectric devices to industrial smokestacks is of course the next step and could make possible the production of cleaner and cheaper electricity by recycling the heat losses.

Unfortunately, thermoelectric devices only reach 30 % of the Carnot efficiency in the temperature range of 300-900 K [2]. In order to become truly competitive with existing energy generators or refrigerators, this performance should be tripled. If this efficiency, through hard progress in research, supposedly greatly increase, a whole new field of application would arise. One can think of recycling body temperature through clothes, recycling building heating losses through the walls or painting or simply using the temperature gradient induced by the sun radiation in every exposed material.

This chapter, mainly based on Refs. [7–15], explains the thermoelectricity itself and the efficiency of basic-thermoelectric devices. The understanding of the physics behind this property is important in order to correctly target the relevant candidate materials. The influence of material dimension on thermoelectricity is explained through the presentation of suitable compounds. Finally the relevance of Zintl structures is explained and their formalism is briefly introduced.

1.1 Characterization [7, 8]

Three reversible thermoelectric phenomena linking the electric current and heat flux can be explained by simply considering an electrical-conductor bar undergoing a thermal gradient (see Figure 1.1). The conduction electrons at the hot end have a thermal energy of about $k_B T$ which enable them to diffuse to the cold end : electrons and holes travel in opposite directions. This migration creates a voltage difference. An intrinsic Seebeck coefficient S [V.K^{-1}] characterizes the appearance of this potential difference in a material when it is subjected to a temperature gradient. The Seebeck coefficient is conventionally negative for a n-type semiconductor and positive for a p-type. It is expressed as follow:

$$S = \frac{\Delta V}{\Delta T} \tag{1.1}$$

The Seebeck effect is then defined as the induction of an electric field E [V] due to the polarization of the material under the influence of a thermal gradient ∇T [K]. It is defined by

$$\vec{E} = S \cdot \vec{\nabla} T \tag{1.2}$$

The Peltier effect is the reverse effect : a current passing through a material induces a heat flux in this one. The Peltier coefficient, denoted Π [V], quantifies the relationship between the

flux of extracted or generated heat Φ [J/s] by the electrical current I [A] through the material. It is expressed as

$$\Pi = \frac{\Phi}{I} \tag{1.3}$$

The Thomson effect appears in materials whose Peltier coefficient is temperature dependent. The Thompson coefficient, denoted τ [V.K^{-1}] characterizes a generation or absorption of heat in a material subjected to a temperature difference and traversed by an electric current. It is defined as

$$\tau = \frac{d\Pi}{dT} \tag{1.4}$$

At the time, Peltier and Seebeck did not have the tools to understand what they had observed experimentally. It is Lord Kelvin (Thomson) that linked the three coefficients S, Π and τ by the two following relationships:

$$\Pi = T \cdot S \tag{1.5}$$

$$\tau = T \cdot \frac{dS}{dT} \tag{1.6}$$

The coupling between electrical and thermal phenomena opens up two possible applications, namely electricity generation (Seebeck effect) and refrigeration (Peltier effect). The current generation occurs when an external heat source causes a temperature difference at the ends of the material. An electrical voltage is then established and can be exploited to generate a current in a load resistor. Refrigeration is made possible by the heat flow which is established after the imposition of an electric current across a material. This flow helps to remove the heat of a body to be cooled to an area where the heat is dissipated to the ambient environment.

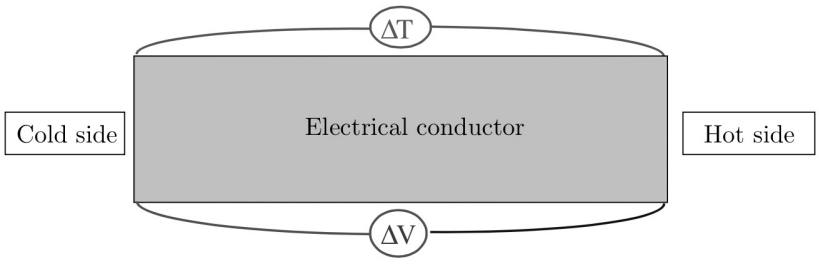

Figure 1.1: Representation of the Seebeck effect in a conductor bar: thermal gradient and induced electrical gradient. Adapted from Ref. [8].

1.2 Thermoelectric devices [8, 9]

For both the generation of electricity or the heating/cooling effect, a set of thermocouples is connected. Each thermocouple consists of two branches of semiconducting material: a p-type ($S > 0$) and a n-type semiconductor ($S < 0$). These two materials are joined by a conducting material whose Seebeck coefficient is assumed to be zero. The reason for the use of branches of different types will be explained here below. Many thermocouples compose the module and are connected electrically in series and thermally in parallel, as represented in Figure 1.2. This arrangement maximizes the heat flux through the module and its electrical resistance. Two types of thermocouple can then be considered : the electricity generation and the refrigeration thermocouple.

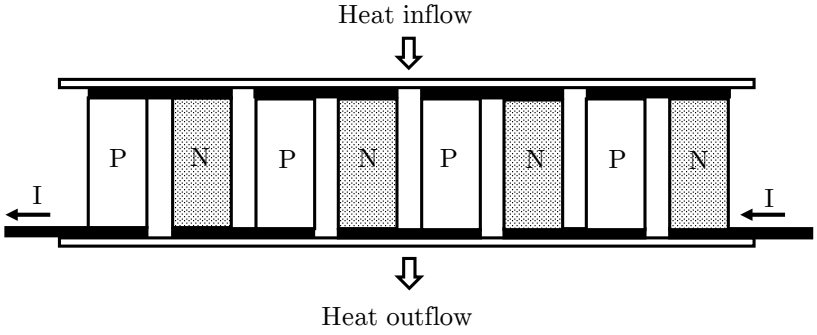

Figure 1.2: Thermoelectric module connected electrically in series and thermally in parallel.

Electricity generation thermocouple

The thermocouple configured for electricity generation, represented in Figure 1.3, is characterized by its performance η, defined as follows:

$$\eta = \frac{\text{electrical work that can be generated in the circuit}}{\text{amount of heat to provide to the hot side}} \tag{1.7}$$

$$\eta = \frac{T_h - T_c}{T_h} \frac{\sqrt{1 + Z_{np} T_{av}} - 1}{\sqrt{1 + Z_{np} T_{av}} + \frac{T_h}{T_c}} \tag{1.8}$$

where T_c is the temperature on the cold side, T_h is the hot side temperature, T_{av} is the average temperature [$T_{av} = (T_h + T_c)/2$] and Z_{np} the figure of merit of the couple np [K^{-1}]. This factor depends on the intrinsic transport properties of both p and n-type branches:

$$Z_{np} = \frac{(S_p - S_n)^2}{\left(\sqrt{\kappa_n/\sigma_n} + \sqrt{\kappa_p/\sigma_p}\right)^2} \tag{1.9}$$

where $S_{n/p}$ is the Seebeck coefficient of the n/p-type semiconductor, $\sigma_{n/p}$ the electrical conductivity [$1/\Omega$.m] and $\kappa_{n/p}$ the thermal conductivity [W/m.K]. One can understand through this

equation why different types of branches are used in couples: this will maximize the numerator and therefore the figure of merit.

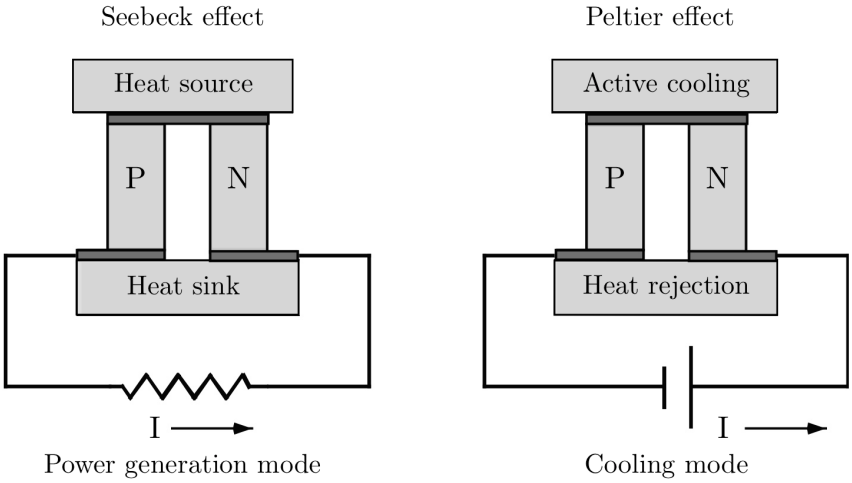

Figure 1.3: Descriptive diagrams of a *pn* couple used for thermoelectric generation (Seebeck effect) and the cooling (Peltier effect). Adapted from Ref. [8].

Refrigeration thermocouple

The thermocouple configured for cooling is characterized by the coefficient of performance COP defined as follows:

$$\text{COP} = \frac{\text{amount of heat absorbed at the cold side}}{\text{amount of work produced by the external power generator}} \tag{1.10}$$

$$\text{COP} = \frac{T_h}{T_h - T_c} \frac{\sqrt{1 + Z_{np} T_{av}} - T_h/T_c}{\sqrt{1 + Z_{np} T_{av}} + 1} \tag{1.11}$$

1.3 Figure of merit [8]

Performances of both devices are limited by the performance of a Carnot machine and depend on the thermal gradient and materials through the figure of merit Z_{np}. Indeed, the efficiency of a thermoelectric material can be summarized in the dimensionless figure of merit

$$Z \cdot T = \frac{S^2 \sigma}{\kappa_e + \kappa_l} \cdot T \tag{1.12}$$

where Z depends only on the material, S is the Seebeck coefficient of the thermocouple ($S = S_p - S_n$), σ is the electrical conductivity, κ_e is the electronic thermal conductivity and κ_l is the

lattice contribution to the thermal conductivity. T is the temperature, it is added in order to make the figure of merit Z dimensionless. As said previously this factor must be maximized to ensure an optimum conversion of the temperature gradient into a potential difference within the material concerned. It should be calculated for each type of material forming couples. But one can note that at the classical temperatures encountered for power generation, thermoelectric properties of best p-type and n-type semiconductors are similar. The figure of merit is then close to the mean of the individual factors of merit and it is reasonable to optimize two materials independently of one another. The electrical and thermal transport properties of the materials used in energy conversion by thermoelectric effect must therefore be correctly optimized in order to reach high figure of merit:

To manufacture thermoelectric generators with the best performance requires a **high Seebeck coefficient** S, a **high electrical conductivity** σ to minimized the Joule losses and a **low thermal conductivity** κ to retain heat near the junction.

Improving a material is therefore a puzzle. Indeed, in order to maximize σ, materials must have a high density of electrons. From the free-electron model, the conductivity can be expressed as

$$\sigma = \frac{ne^2\tau_e}{m_e^*} \tag{1.13}$$

where n is the number of electrons per volume at the Fermi energy [cm^{-3}], m_e^* is their effective mass [m_0^*] and τ_e their average collision time [s]. But these electrons also contribute to heat conduction so that it will increase κ_e. Using the same model, the electronic thermal contribution is indeed defined as

$$\kappa_e = \frac{1}{3}C_e v_F l_e = \frac{\pi^2 n k_B^2 T \tau_e}{3m_e^*} \tag{1.14}$$

where C_e is the specific heat capacity of the electrons [J/kg.K], v_F is the Fermi velocity [m/s] and l_e the mean free path of electrons [m]. The law of Wiedemann-Franz links these charge-carriers conductivities to the constant Lorenz number L_0 [$\mathrm{W.\Omega/K^2}$]. This law is mainly valid for metals and heavily doped semiconductors (where the charge carriers operate the transport of current and heat) and assume that the elastic scattering dominates (low or high temperature but not medium). It is expressed by the ratio of (1.13) and (1.14):

$$L_0 = \frac{\kappa_e}{\sigma T} = \frac{\pi^2}{3}\left(\frac{k_B}{e}\right)^2 = 2.44 \times 10^{-8} \tag{1.15}$$

where k_B is the Boltzmann constant [J/K] and e the electron charge [C]. The thermal conductivity must thus be reduced through its lattice contribution only since the reduction of its electronic contribution lead to an increase of the electric resistivity, i.e. a decrease of the figure of merit.

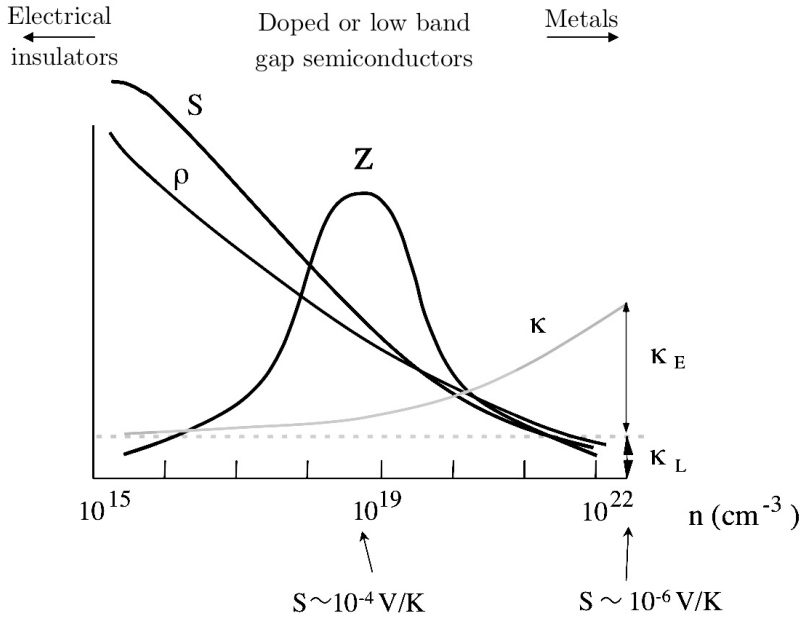

Figure 1.4: Electrical resistivity ρ [Ω.m], lattice and electronic contributions to thermal conductivity κ_l and κ_e [W/m.K], Seebeck coefficient S [V/K] and figure of merit Z [–] in function of the carrier concentration [cm^{-3}], at ambient temperature. Adapted from Ref. [8].

The sum of these various contributions are illustrated in Figure 1.4, in function of the carrier concentration. The electrical conductivity dependence is represented by the electrical resistivity $\rho = 1/\sigma$. By analysing the variation of the figure of merit, one can understand why heavily doped semiconductor are the most commonly used materials.

1.4 Thermoelectric materials [10–13]

Historically, as explained previously, the basics of thermoelectricity have been properly established in 1950 but the applications remained confined to niche applications. But since 1990, scientists have seriously searched for the best thermoelectric materials and for techniques to enhance the figure of merit. Three strategies, corresponding to three types of materials, are mainly explored today.

Alloys

A first strategy is to reduce lattice thermal conductivity by increasing the phonon scattering within the unit cell. Adding interstitials, vacancies or nano-precipitates, creating rattling structures as well as alloying are means to achieve this goal. Heavy-ion species (mostly rare earth elements) have large vibrational amplitudes so that they can also be introduced in the structure to scatter phonon. The thermal conductivity is then reduced without impacting the charge carrier transport.

Low-dimensional materials

A second strategy is to use low-dimensional materials. As explained previously, the Wiedmann-Franz law (1.15) links the electrical conductivity σ thermal and κ in 3D materials. But when the dimensionality of the material is reduced, discontinuities in the density of electronic states appear (see Figure 1.5) and lead to confinement effects of the charge carriers. It allows a beneficial decoupling of electronic and thermal transport which helps to increase the figure of merit.

The second major benefit of low-dimensional materials is the possibility to introduce many interfaces. These must be distributed at shorter distances than the mean free path of the phonons, but higher than the mean free path of electrons in order to scatter phonons more efficiently than electrons. The thermal conductivity will therefore fall sharply while the electrical conductivity will decrease only slightly. The improvement of the figure of merit is actually more important when phonons are diffused that when carriers are confined.

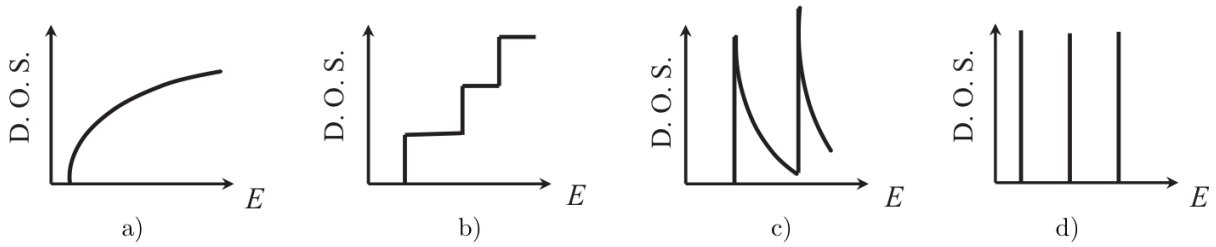

Figure 1.5: Electronic density of states for a) a 3 D crystalline semiconductor, b) a 2 D quantum well, c) a 1 D nanowire or nanotube, and d) a 0 D quantum dot. Adapted from Ref. [16].

Complex crystals

The ideal thermoelectric material should possess the low thermal properties of a glass (no periodic arrangement of atoms) and the electrical properties of a perfect single-crystal material : a phonon-glass electron-crystal (PGEC). Electrons would be weakly scattered while phonons would be strongly scattered. Large and complex unit cells can result in glass-like lattice thermal conductivity at high temperature because of the confinement of heat into low velocity optical phonon modes and the possibilities to scatter phonon. The thermal conductivity is therefore reduced without disrupting the crystallinity of the electron-transport region. Zintl phases like $Ca_5Al_2Sb_6$ and Ca_3AlSb_3 are typical complex crystals and are thus interesting options for thermoelectric materials.

1.5 Zintl phases [14, 15]

It is important to review the basic chemistry behind Zintl phases in order to understand the reason of their complexity, since it is what makes them interesting thermoelectric candidates. The explanations given below are directly inspired from Refs. [14, 15].

Zintl phases were named after Edward Zintl who studied their structures in the 1930s. They have similarities with metallic and ionic compounds. They are composed of an alkali or alkaline-earth metal and *p*-element(s) (metal, semimetal, or small-gap semiconductor). Most of Zintl compounds are semiconductors with their band gap decreasing with increasing atomic number of the electronegative part of the compound. These structures are brittle and are sometimes diamagnetic or show very weak, temperature-independent paramagnetism.

The structural and bonding characteristics of Zintl phases comply with Zintl-Klemm concept. Valence electrons from highly electronegative cations are fully transferred to anions. Anions then form covalently-bonded polyanions, called substructures, to satisfy their valence. This valence-precise nature distinguishes the Zintl phases from other intermetallic compounds and leads to many unique, complex crystal structures. It is the covalently-bonded substructures that provides the desired "electron–crystal" electronic structure. The constituent elements in Zintl compounds lead to different structures and semiconducting electronic behaviors. Such complexity in the unit cell leads to the containment of heat in low velocity optical modes in the phonon dispersion. Most of the Zintl phases reach exceptionally low lattice thermal conductivity (0.4 - 0.6 W/mK at 1000 K) which is the reason of their use as thermoelectrics. Due to their large chemistry, many possibilities of chemical substitutions and structural modifications exist. The transport parameters can therefore be tuned to enhance the figure of merit.

In the light of these explanations of thermoelectricity and the characteristics of Zintl phases, the electronic transport properties of $Ca_5Al_2Sb_6$ and Ca_3AlSb_3 can now be theoretically studied. The computational theories used for this purpose are firstly explained in the next chapter.

Chapter 2

Computational methods

Contents

Investigating the field of condensed matter physics from a theoretical or computational point of view is very challenging. Most of the time, (semi-) empirical models are built from the study of macroscopic phenomena to describe experimental results. These models can help to understand the physics behind a system and can even be interpolated or extrapolated in order to predict the behaviour of systems under different conditions. However, this empiric approach remains limited because of the complexity of condensed matter systems.

The first-principle approach – also called *ab initio* approach – relies on basic physical laws and does not take into account additional assumptions or special models. The matter is considered from the basic elements that constitute it: atoms, i.e. their positively charged nuclei and their negatively charged electrons. As interactions between nuclei and electrons govern interatomic interactions, the purpose of the first-principle approach is to model these in order to understand complex physical phenomena.

This chapter, mainly based on Refs. [17–21], is a global review at the first-principle theories that were used to compute physical properties in this thesis. The density functional theory is briefly explained as well as its implementation in the ABINIT software [22]. In this thesis,

calculations using this method allowed to investigate the density of states and electronic structures of both $Ca_5Al_2Sb_6$ and Ca_3AlSb_3 compounds. Their elastic constants were also computed from density functional perturbation theory. The semi-classical Boltzmann transport theory is then explained in the relaxation time approximation. The BoltzTraP software [23] allowed to compute the transport coefficients derived from this theory for the two Zintl phases, which was necessary to investigate their thermoelectric efficiency.

2.1 Density functional theory [17, 18]

2.1.1 Global overview

Many physical properties can be derived from the electronic structure of a material. It is therefore necessary to correctly compute the latter. This can be achieved through first-principle calculations. Traditional approaches like the Hartree-Fock theory or its derived methods are based on multielectronic-wave functions to perform this computation. The density functional theory (DFT) uses the fact that, as Hohenberg-Kohn's first theorem stipulates [24], the spatially dependent electron density is sufficient to determine the ground state properties of a many-electron system. Using functionals of the electron density therefore allows one to reduce the many-body of N electrons with 3 N spatial coordinates to only three spatial coordinates, which is much easier to treat computationally. On top of that, the DFT can be extended to the time-dependent domain (TD-DFT) in order to describe excited states or can study response functions (perturbations) in a system (DFPT).

The DFT formalism requires to introduce an approximation for the exchange and correlation interactions that go beyond the Hartree term for describing the electron-electron interactions. The most common ones are the local density approximation (LDA) and the generalized gradient approximation (GGA). The LDA, used in this thesis, involves an analytic expression of the exchange energy which is exact for a homogeneous electron gas as well as a parametrization of the correlation energy for this gas.

A more complete introduction to the main principles of the DFT and the LDA can be found in Appendix A.

2.1.2 Abinit : a DFT-based computational software

The open-source Abinit software [22] implements the DFT by solving the Kohn-Sham equations to describe the behavior of electrons in a material, using plane wave as basic functions. Since the potential of the system is periodic, the Bloch theorem applies. The wave functions $\Psi_{n,\mathbf{k}}$ take thus a periodic shape, following the Bloch functions $u_{n,\mathbf{k}}(\mathbf{r})$ which have themselves the lattice periodicity. They are expressed as

$$\Psi_{n,\mathbf{k}} = (N\Omega_0)^{-1/2} e^{i\mathbf{k}.\mathbf{r}} u_{n,\mathbf{k}}(\mathbf{r}) \tag{2.1}$$

where $(N\Omega_0)$ is the normalization factor and the $\mathbf{k}$ index differentiates the various specific states corresponding to the energy $\varepsilon_{\mathbf{k}}$. A plane-wave basis set is thus the natural way to describe $u_{n,\mathbf{k}}(\mathbf{r})$. In principle, one should use an infinite number of planewaves to describe the wave functions, but in the computational reality only a limited number of planewaves functions are used. This number is defined by the cut-off energy, represented by the variable `ecut` in ABINIT : all the planewaves whose vectors have a kinetic energy below this limit are used to describe the system.

For both $Ca_5Al_2Sb_6$ and Ca_3AlSb_3 compounds, the *ab initio* ABINIT software was firstly used in this thesis to study the convergence of the lattice parameters as a function of the cut-off energy and the number of k-points that were used to sample the Brillouin zone (the primitive cell in the reciprocal space). This k-grid points is defined using the variable `ngkpt`, with a specific number of k-points (`kpt`). The Brillouin zone was integrated along a specific path (including its high symmetry points) to draw the band structure of those compounds. The densities of states were calculated in order to identify the dominant states at the edge of the band gap. Electron density difference maps were computed to identify the type of bonding between atoms in unit cells. The results of those calculations for $Ca_5Al_2Sb_6$ and Ca_3AlSb_3 are respectively given in Chapters 3 and 4.

After a first analysis of the transport properties based on those band structures, ABINIT was employed again for two other calculations. First the density functional perturbation theory was used to calculate the elastic constants of the materials. Secondly deformation potentials were calculated by comparing electronic structures of a unit cell under different stresses. More explanations about those calculations are given in the relative Chapter 5.

To perform all those calculations, it is convenient to substitute the potential of Coulomb interaction of the nucleus and the effects of strongly-linked core-electrons by an effective potential interacting only with valence electrons, i.e. to use pseudopotentials. This substitution allows one to treat only the low-energy electrons, which are constituent of bonding, and therefore reduces significantly the calculation time. Norm conserving pseudopotentials FHI (Fritz-Haber-Institute [25]) within the local density approximation were used for Ca, Al and Sb atoms in this thesis[1].

[1]Those pseudopotentials are available on the ABINIT website at `http://www.abinit.org/downloads/psp-links/lda_fhi`.

2.2 Boltzmann transport theory [19–21]

The Boltzmann equation describes the statistical behavior of a fluid of electrons which is not in thermodynamic equilibrium. Considering the relaxation time approximation it is possible to derive analytical expressions for transport properties of interest : the electronic conductivity, the thermal conductivity and the Seebeck coefficient. The following explanations are directly inspired from Refs. [19–21].

2.2.1 Boltzmann equation

First of all, it is important to remember that the distribution function of an electron gas at equilibrium, i.e. the average occupation number by electrons of the state $\mathbf{k}$ with energy $\varepsilon_{\mathbf{k}}$, is given by the following Fermi-Dirac distribution function:

$$f^0_{\mathbf{k}} = \frac{1}{e^{(\varepsilon_{\mathbf{k}}-\mu)/k_B T}+1} \tag{2.2}$$

where k_B is the Boltzmann constant and μ is the chemical potential.

In a more general way, the distribution function $f(\mathbf{r},\mathbf{k},t)$ of electrons with a wave vector $\mathbf{k}$ at the position $\mathbf{r}$ at time t can vary due to three processes : the diffusion of electrons by temperature or concentration gradients, their acceleration by an external field and finally their scattering by phonons, lattice defects or impurities. The variation in time of the total distribution can be expressed as the sum of these three contributions:

$$\left(\frac{\partial f}{\partial t}\right) = \left(\frac{\partial f}{\partial t}\right)_{\text{diffusion}} + \left(\frac{\partial f}{\partial t}\right)_{\text{field}} + \left(\frac{\partial f}{\partial t}\right)_{\text{scattering}} \tag{2.3}$$

First of all, one can consider an electron is not subject to scattering but experiences an external field $\mathbf{F}$. It induces a variation of its wave vector $\mathbf{k}$ since the external field is expressed as

$$\mathbf{F} = \hbar\frac{d\mathbf{k}}{dt} \tag{2.4}$$

During a time interval dt, the electron will move from one state $(\mathbf{r}-\dot{\mathbf{r}}dt, \mathbf{k}-\dot{\mathbf{k}}dt, t-dt)$ to another $(\mathbf{r},\mathbf{k},\mathbf{t})$. Since the scattering is left aside, the change rate of the distribution function represents the continuous flow of a particle taking into account the diffusion and the acceleration of the electrons. It is then called the drift term and can be expressed by

$$\left(\frac{df}{dt}\right)_{\text{drift}} = \frac{f(\mathbf{r}-\dot{\mathbf{r}}dt, \mathbf{k}-\dot{\mathbf{k}}dt, t-dt) - f(\mathbf{r},\ \mathbf{k}, t)}{dt} \tag{2.5}$$

The Taylor expansion of the first term allows one to express it as

$$f(\mathbf{r}-\dot{\mathbf{r}}dt,\mathbf{k}-\dot{\mathbf{k}}dt,t-dt)=f(\mathbf{r},\mathbf{k},\mathbf{t})-\left[\dot{\mathbf{k}}\cdot\frac{\partial\mathbf{f}}{\partial\mathbf{k}}+\dot{\mathbf{r}}\cdot\frac{\partial\mathbf{f}}{\partial\mathbf{r}}+\frac{\partial\mathbf{f}}{\partial\mathbf{t}}\right]\mathbf{dt}+\cdots \tag{2.6}$$

Considering this Taylor expansion, the change of the wave vector under a force (2.4) and the velocity of the electron $\mathbf{v}=\dot{\mathbf{r}}$, the drift term can then be rewritten as

$$\left(\frac{df}{dt}\right)_{\text{drift}}=-\left[\frac{1}{\hbar}(\mathbf{F}\cdot\nabla_{\mathbf{k}}f)+\mathbf{v}\cdot\nabla_{\mathbf{r}}f+\frac{\partial f}{\partial t}\right] \tag{2.7}$$

Even if left aside at first, one has to remember that the electron scattering also plays an important part in their distribution. To be correct, the distribution function has to satisfy the equilibrium condition which means that the sum of the contributions (2.3) has to be null at the steady state. Since the drift term takes diffusion and acceleration into account, this steady state condition leads to

$$\left(\frac{df}{dt}\right)_{\text{drift}}=\left(\frac{df}{dt}\right)_{\text{scattering}} \tag{2.8}$$

This condition of balance results in the Boltzmann transport equation:

$$\frac{\partial f}{\partial t}=-\mathbf{v}\cdot\nabla_{\mathbf{r}}f-\frac{1}{\hbar}(\mathbf{F}\cdot\nabla_{\mathbf{k}}f)+\left(\frac{df}{dt}\right)_{\text{scattering}} \tag{2.9}$$

The three main contributions to the rate of the transport distribution function change with time are correctly found in this equation. In the right part of the equation, the first term on the left is related to the electron diffusion moving in and out a specific volume with a velocity $\mathbf{v}$. If the distribution function is spatially homogeneous this term becomes zero. On the contrary, when this function varies in space, the electron ratio flowing in and out the volume is not zero anymore and this diffusion becomes a contribution to the change of the distribution function. Now if the distribution function varies with the momentum state $\mathbf{k}$, the number of particles accelerated by an external force $\mathbf{F}$ into a specific region of momentum will differ from the particles that are leaving this same region. The second term is related to this effect. The last term is related to the probability of electron scattering and brings up the difficulty to solve the Boltzmann transport equation. Nevertheless no physical solution can be found without it. It is then necessary to simplify the collision term through the relaxation time approximation to express the related variation of the distribution function.

2.2.2 Relaxation time approximation

In order to solve the Boltzmann transport equation, one has to give an analytical expression to the scattering term. This can be done considering the transitions leading to a change of **k**-state. The distribution function can be seen as independent of the position **r** in this case. If a transition occurs from the state **k** to another state $\mathbf{k}'$, $f(\mathbf{k})$ will decrease and conversely. The scattering term can then be expressed by

$$\left(\frac{df}{dt}\right)_{\text{scat.}} = \sum_{\mathbf{k}'} \left(W(\mathbf{k}', \mathbf{k}) \cdot f(\mathbf{k}')[1 - f(\mathbf{k})] - W(\mathbf{k}, \mathbf{k}') \cdot f(\mathbf{k})[1 - f(\mathbf{k}')]\right) \tag{2.10}$$

where $W(\mathbf{k}', \mathbf{k})$ is the transition rate from a state $\mathbf{k}'$ to a state **k**, $f(\mathbf{k}')$ is the probability of electron occupation in the initial state $\mathbf{k}'$ and $(1 - f(\mathbf{k}))$ is the probability of the presence of a vacancy in the state **k**. The usual case where the Fermi level lies below the bottom of the conduction band ($f(\mathbf{k})$ and $f(\mathbf{k}') \ll 1$) is studied. Considering the equilibrium state (2.2), one can express the following equation

$$W(\mathbf{k}', \mathbf{k}) \cdot f_0(\mathbf{k}') = W(\mathbf{k}, \mathbf{k}') \cdot f_0(\mathbf{k}) \tag{2.11}$$

One can observe here the logical impact of this equality on the transition probabilities. When $\varepsilon_{\mathbf{k}} < \varepsilon_{\mathbf{k}'}$, $W(\mathbf{k}, \mathbf{k}') < W(\mathbf{k}', \mathbf{k})$. In other words, the probability for an electron to be scattered from a low energy state to a higher one is smaller than the inverse probability. The scattering can be rewritten as

$$\left(\frac{df}{dt}\right)_{\text{scat.}} = -\sum_{\mathbf{k}'} W(\mathbf{k}, \mathbf{k}') \left[f(\mathbf{k}) - f(\mathbf{k}')\frac{f_0(\mathbf{k})}{f_0(\mathbf{k}')}\right] \tag{2.12}$$

In almost every real case, the deviation from the equilibrium is small, i.e. the scattering results from an elastic collision. The initial energy state $\varepsilon_{\mathbf{k}}$ is then close from the energy of the final state $\varepsilon_{\mathbf{k}'}$. This can be stated as

$$f(\mathbf{k}) = f_0(\mathbf{k}) + f_1(\mathbf{k}), \quad \text{with} \quad f_1(\mathbf{k}) \ll f_0(\mathbf{k}) \tag{2.13}$$

It results in the approximation $f_0(\mathbf{k}) \approx f_0(\mathbf{k}')$ and allows one to rewrite the scattering term as

$$\left(\frac{df}{dt}\right)_{\text{scat.}} = -f_1(\mathbf{k}) \sum_{\mathbf{k}'} W(\mathbf{k}, \mathbf{k}') \left[1 - \frac{f_1(\mathbf{k})}{f_1(\mathbf{k}')}\right] \tag{2.14}$$

Those assumptions constitute the relaxation time approximation, only valid for homogeneous scattering. The relaxation time $\tau(\mathbf{k})$ is defined as the time between two collisions leading to

scattering and allows one to rewrite the scattering term as

$$\left(\frac{df}{dt}\right)_{\text{scat.}} = -\frac{f_1(\mathbf{k})}{\tau(\mathbf{k})} = -\frac{f(\mathbf{k}) - f_0(\mathbf{k})}{\tau(\mathbf{k})} \tag{2.15}$$

where

$$\frac{1}{\tau(\mathbf{k})} = \sum_{\mathbf{k}'} W(\mathbf{k}, \mathbf{k}') \left[1 - \frac{f_1(\mathbf{k})}{f_1(\mathbf{k}')}\right] \tag{2.16}$$

In this relaxation time approximation, the Boltzmann transport equation is reformulated as

$$\frac{\partial f}{\partial t} + \frac{1}{\hbar}(\mathbf{F} \cdot \nabla_{\mathbf{k}} f) + \mathbf{v} \cdot \nabla_{\mathbf{r}} f = \frac{f(\mathbf{k}) - f_0(\mathbf{k})}{\tau(\mathbf{k})} \tag{2.17}$$

This relaxation time characterizes the speed of recovery of the equilibrium state: for a short relaxation time, many collisions help the system to return to its initial state and conversely for a long relaxation time. Indeed a system recovering from a steady but non equilibrium state ($t = 0$) to its equilibrium without any external force will satisfy the following equation:

$$\frac{\partial f}{\partial t} = -\frac{f(\mathbf{k}) - f_0(\mathbf{k})}{\tau(\mathbf{k})} \tag{2.18}$$

The non equilibrium system then decays exponentially with the relaxation time to its equilibrium:

$$f - f_0 = (f - f_0)_0 \; e^{-t/\tau} \tag{2.19}$$

In Chapters 3 and 4, the relaxation time is approximated by a constant value. But in fact, the transition probabilities will differ depending on the type of scattering mechanisms electrons are facing and this relaxation time will take different temperature and energy dependent expressions. The expressions of ionized impurity and acoustic phonon scattering mechanisms, relevant for the transport properties of the two Zintl compounds $Ca_5Al_2Sb_6$ and Ca_3AlSb_3, are derived in Chapter 5.

2.2.3 Transport coefficients derivation

It is crucial, in order to study thermoelectricity, to be able to calculate the transport properties of a system. At the macroscopic level, the relations between the electrical or the heat current $\mathbf{J}$ and $\mathbf{J}_Q$, the electric field $\mathbf{E}$ and a temperature gradient ΔT in an isotropic solid are

$$\mathbf{J} = \sigma \cdot \mathbf{E} + S\sigma \cdot \Delta T \tag{2.20}$$

$$\mathbf{J}_Q = S\sigma T \cdot \mathbf{E} + \kappa \cdot \Delta T \tag{2.21}$$

where σ is the electrical conductivity, S the Seebeck coefficient and κ the thermal conductivity. At the microscopic level of the transport, the electrical current of carriers is defined by

$$\mathbf{J} = e \sum_{\mathbf{k}} f(\mathbf{k}) \mathbf{v}(\mathbf{k}) \tag{2.22}$$

where e is the charge of the carriers. The group velocity $\mathbf{v}(\mathbf{k})$ is formulated as

$$\mathbf{v}(\mathbf{k}) = \frac{1}{\hbar} \frac{\partial \varepsilon_{\mathbf{k}}}{\partial \mathbf{k}} \tag{2.23}$$

There is here a need for an analytical expression of the distribution function, the one which is expressed by the Boltzmann transport theory. In the absence of magnetic field and temperature gradients, the population on the state $\mathbf{k}$ – i.e. the distribution function $f(\mathbf{k})$ – is given by the linearized Boltzmann transport equation (2.17). This expression can be rewritten in a convenient way when considering an electric field $\mathbf{E}$ ($\mathbf{F} = e\mathbf{E}$) and a stationary state ($\partial f / \partial t = 0$) as

$$f(\mathbf{k}) = f_0(\varepsilon_{\mathbf{k}}) + e \left(-\frac{\partial f_0}{\partial \varepsilon} \right) \tau(\mathbf{k}) \mathbf{v}(\mathbf{k}) \cdot \mathbf{E} \tag{2.24}$$

The electrical current can then be reformulated as

$$\mathbf{J} = e f_0(\varepsilon_{\mathbf{k}}) \sum_{\mathbf{k}} \mathbf{v}(\mathbf{k}) + e^2 \sum_{\mathbf{k}} \left(-\frac{\partial f_0}{\partial \varepsilon} \right) \tau(\mathbf{k}) \mathbf{v}(\mathbf{k}) \mathbf{v}(\mathbf{k}) \cdot \mathbf{E} \tag{2.25}$$

When there is no gradient of temperature, the macroscopic expression of the electrical current (2.22) is reduced to its electric field contribution. The electrical conductivity can then be expressed as

$$\sigma(\mathbf{k}) = e^2 \sum_{\mathbf{k}} \left(-\frac{\partial f_0}{\partial \varepsilon} \right) \tau(\mathbf{k}) \mathbf{v}(\mathbf{k}) \mathbf{v}(\mathbf{k}) \cdot \mathbf{E} \tag{2.26}$$

$$\sigma(\mathbf{k}) = \sum_{\mathbf{k}} \left(-\frac{\partial f_0}{\partial \varepsilon} \right) \sigma(\mathbf{k}) \tag{2.27}$$

The transport properties are expressed as tensors since they can be anisotropic. As for the density of states, the tensor of conductivity shows a distribution in energy. It represents the contribution to the conduction of electrons having an specific energy ε:

$$\Xi = \sum_{\mathbf{k}} \sigma(\mathbf{k}) \frac{\delta(\varepsilon - \varepsilon_{\mathbf{k}})}{d\varepsilon} \tag{2.28}$$

The transport coefficients in a unit cell crystal of volume Ω can then be calculated for a specific chemical potential μ and temperature by integrating this conductivity distribution:

$$\sigma(T,\mu) = \frac{1}{\Omega}\int \Xi(\varepsilon)\left[-\frac{\partial f_\mu(T,\varepsilon)}{\partial \varepsilon}\right] d\varepsilon \tag{2.29}$$

$$S(T,\mu) = \frac{1}{\Omega e T \sigma(T,\mu)}\int \Xi(\varepsilon)(\varepsilon-\mu)\left[-\frac{\partial f_\mu(T,\varepsilon)}{\partial \varepsilon}\right] d\varepsilon \tag{2.30}$$

$$\kappa(T,\mu) = \frac{1}{\Omega T}\int \Xi(\varepsilon)(\varepsilon-\mu)\left[-\frac{\partial f_\mu(T,\varepsilon)}{\partial \varepsilon}\right] d\varepsilon \tag{2.31}$$

2.2.4 BoltzTraP : a BTE-based computational software

The BoltzTrap code [23] allows one to compute these transport coefficients with little computational effort. This code uses Fourier expansions to solve Boltzmann equation in the relaxation time approximation. The interpolated band structure is used to calculate the required derivatives to evaluate transport properties, e.g. the group velocities. It is therefore essential that the band energies are correctly computed through Abinit before using BoltzTraP. In this code, the rigid band approximation is made. It means that the bands are independent in doping, the chemical potential is simply shifted.

To facilitate the computation of the transport coefficients, the relaxation time can be considered as constant in BoltzTraP, i.e. temperature and energy independent. However, it is also possible to implement energy and temperature dependent relaxation times corresponding to specific electron scattering processes and then to compute their relative transport properties.

The implementation in Abinit and BoltzTraP softwares of the two theories presented in this chapter allows one to begin the theoretical study of $Ca_5Al_2Sb_6$ and Ca_3AlSb_3. The two following chapters are basic *ab initio* studies of these two compounds. Their electronic band structures are computed and used for computing the transport properties in the constant relaxation time approximation.

Chapter 3

Basic *ab initio* study of $Ca_5Al_2Sb_6$

Contents

This chapter aims to study the transport properties of the Zintl compound $Ca_5Al_2Sb_6$ using the constant approximation relaxation time. The unit cell is firstly presented and a complete structural relaxation is performed. An electron density difference map is computed in order to verify the covalent character of the anionic substructure. The electronic structure and the projected density of states are calculated using the density functional theory through the ABINIT code. This structure is then the starting point for computing the electronic transport properties (Seebeck coefficient and electrical resistivity) of $Ca_5Al_2Sb_6$ using the semiclassical Boltzmann transport theory. The approximation of a constant relaxation time is used in this chapter and its validity is discussed through a comparison with experimental results.

3.1 $Ca_5Al_2Sb_6$ crystal [26, 27]

3.1.1 Unit cell

The Zintl compound $Ca_5Al_2Sb_6$ has an orthorhombic unit cell (space group *Pbam*, no. 55 in the Hermann Mauguin notation). This cell is composed of 4 atoms of aluminium, 10 of calcium and 12 of antimony, i.e. two formula units. Representations of its structure were made using the Vesta software[1] and are shown in Figures 3.1 and 3.2. This Zintl phase can be seen as a set of Ca cations crossed by many anionic substructures, composed of antimony tetrahedra linked by Sb–Sb bonds. Each of these tetrahedra encloses an aluminium atom ($AlSb_4$). The five cations Ca^{2-} around a $(Al_2Sb_6)^{10-}$ block (two neighbouring tetrahedra) provide the valence balance. The substructures form one dimensional chains through the crystal along the [100] direction, represented in Figure 3.1 (b).

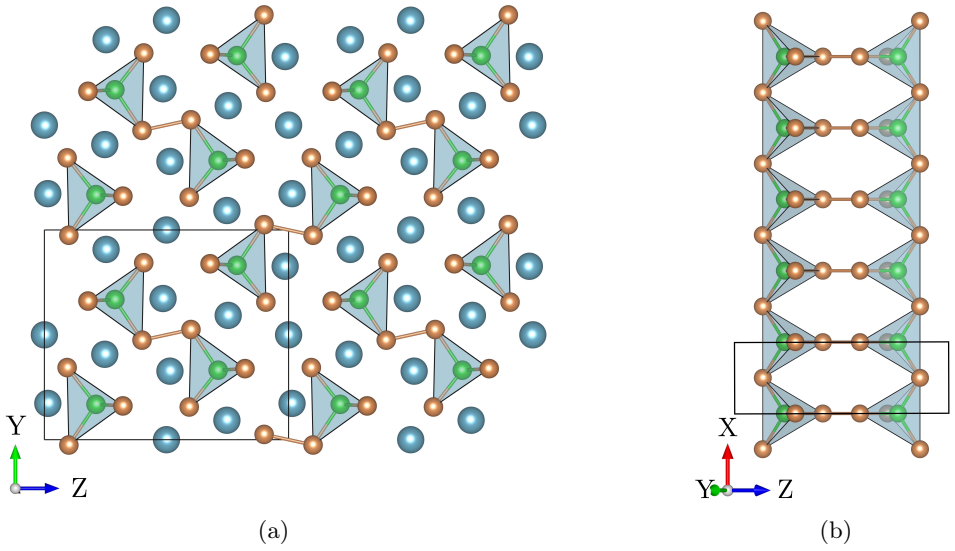

(a) (b)

Figure 3.1: Structural representation of (a) the orthorombic unit cell of $Ca_5Al_2Sb_6$ shown in the [100] direction and of (b) the ladder-like tetrahedral chains connected by Sb–Sb bonds extending along the [100] direction. Ca atoms are represented in blue, Sb atoms in orange and Al atoms in green.

As explained in Section 1.5, it is the covalent character of the anionic substructures that leads to the complexity in the unit cell, i.e. low thermal properties, and also provides the electron crystal electronic structure, i.e. good electrical properties. It is thus interesting to make sure these are correctly covalently bonded. Since a covalent bond should lead to an increased electron density, electron density difference (EDD) isosurfaces were calculated in order to identify those bonds. A first electronic density was calculated for the total $Ca_5Al_2Sb_6$ cell. The electronic density of each atom was then computed considering the atom alone in the $Ca_5Al_2Sb_6$ unit cell volume. Those 26 electronic densities of every atom were finally subtracted to the total one to produced an electron density difference map, shown in Figure 3.3. One can notice a large degree of charge

[1] Vesta is a three-dimensional visualization software for electronic and structural analysis [28]. It is available at `http://jp-minerals.org/vesta/en/download.html`

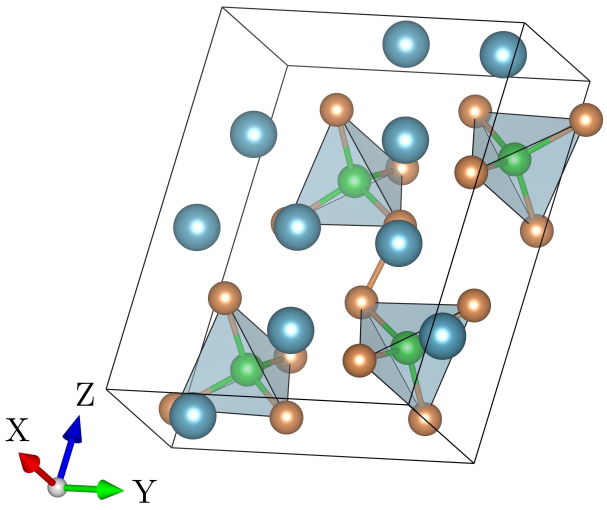

Figure 3.2: Unit cell of $Ca_5Al_2Sb_6$.

accumulation between aluminium and antimony atoms, which suggest a bonding with a strong covalent character. A charge accumulation between the antimony atoms can also be seen when considering much lower isosurfaces. This result is in good agreement with literature [26]. This bonding identification will help to correctly understand the states repartition in the density of states.

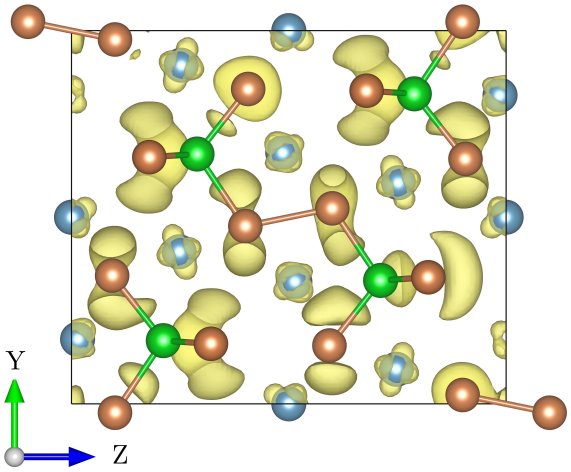

Figure 3.3: Electron density difference map of $Ca_5Al_2Sb_6$.

3.1.2 Structural relaxation

A complete structural relaxation $Ca_5Al_2Sb_6$ crystal was performed using the Broyden-Fletcher-Goldfarb-Shanno (BGFS) algorithm implemented in ABINIT. The cut-off energy and the number

of k-points were converged in order to guarantee the quality of the results while maintaining the computation time at a reasonable level. As explained in Subsection 2.1.2, the cut-off energy limits the number of wave functions that are used to describe the system while the number of k-points are used to sample the Brillouin zone. Lattice parameters are converged with a 0.2 % relative error to an asymptotic value for a cut-off energy of 15 Ha and a 6×6×6 k-points grid, as illustrated in Figure B.1 in the Appendix B. The converged lattice constants are in good agreement with those from the literature as shown in Table 3.1. The relaxed reduced coordinates can be found in Table B.1 in the Appendix B.

Table 3.1: Comparison of the computed lattice constants of for $Ca_5Al_2Sb_6$ with literature.

References	x [Å]	y [Å]	z [Å]
Present work (LDA)	4.50	12.16	14.17
Yan and Wang (LDA) [29]	4.51	12.12	14.09
Yang, He *et al.* (GGA) [27]	4.50	12.13	14.14
The Materials Project [30]	4.49	12.13	14.14

3.2 Electronic structure calculations

It is then necessary to calculate the eigenvalues of the Kohn-Sham equation for a larger number of k-points in order to generate the electronic band structure. A new path of integration including high symmetry points is set through the Brillouin zone. As represented in Figure 3.4, this path is Γ–X–S–Y–Γ–Z–U–R–T–Z|Y–T|U–X|S–R with Γ as the origin of the Brillouin zone. The number of k-points along the smallest segment between two high symmetry points is determined in Abinit by the `ndivsm` variable. Based on that, it is then proportionally adapted for the other segments.

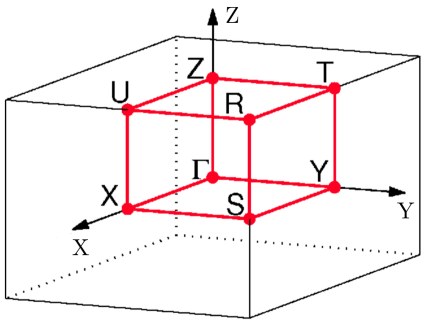

Figure 3.4: Integration path in the Brillouin zone including high symmetry points. Extracted from Ref. [31].

3.2.1 Electronic band structure

First of all, it is important to remember that the band gap is largely underestimated in DFT compared to experimental measures. A more correct band gap can be achieved using more advanced methods like hybrid functionals or GW. However, an erroneous band gap is not critical in this study since a correction shift can easily be added in order to match the experimental gap for further calculations in BoltzTraP. For those reasons no other studies that LDA were performed.

The computed electronic band structure (LDA) is represented in Figure 3.5 and is very similar to the band structure extracted from The Materials Project (computed using GGA), represented in Figure 3.6. Both structures show a direct band gap in Z. This satisfying comparison suggests that the computed band structure is a correct basis for further study. A comparison of several band gaps from experimental and theoretical studies is given in Table 4.2. Experimental band gaps were measured from the slope of the electrical resistivity at high temperature. Their difference are not commented in the literature. As expected, most of theoretical band gaps are underestimated compared to the experimental one. The theoretical band gap of 0.5 eV obtained in Ref. [26] is closer to experimental results since hybrid functionals under the HSE06 scheme were used.

Table 3.2: Comparison of the computed band gap value of $Ca_5Al_2Sb_6$ with the literature.

References	Theoretical band gap [eV]	Experimental band gap (resistivity) [eV]
Present work	0.29 (LDA)	–
The Materials Project [30]	0.15 (GGA)	–
Snyder *et al.* [26]	0.50 (GGA)	0.71
Yan and Wang [29]	0.20 (GGA)	–
Snyder *et al.* [4]	–	0.5

3.2.2 Effective masses

Effective masses play an important role in the electronic transport. It is therefore relevant to compute them and study their eventual anisotropy as it inevitably leads to anisotropic transport properties. Effective masses depend on the dispersion of the energy with the wave vector k, i.e. the band curvature, through the equation

$$\frac{1}{m^*} = \frac{1}{\hbar^2}\frac{\partial^2 \varepsilon}{\partial k^2} \tag{3.1}$$

The effective masses of interest correspond to the bands around the valence band edge as the transport is provided by holes in p-type semiconductor. Since this band gap is situated at the

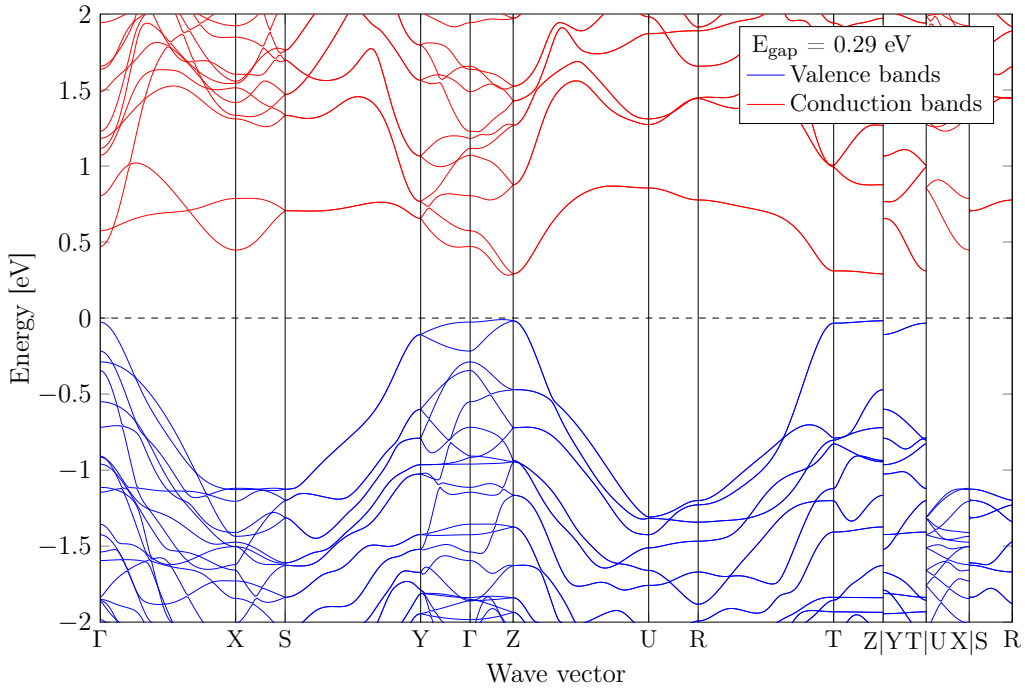

Figure 3.5: Electronic band structure of $Ca_5Al_2Sb_6$ (LDA).

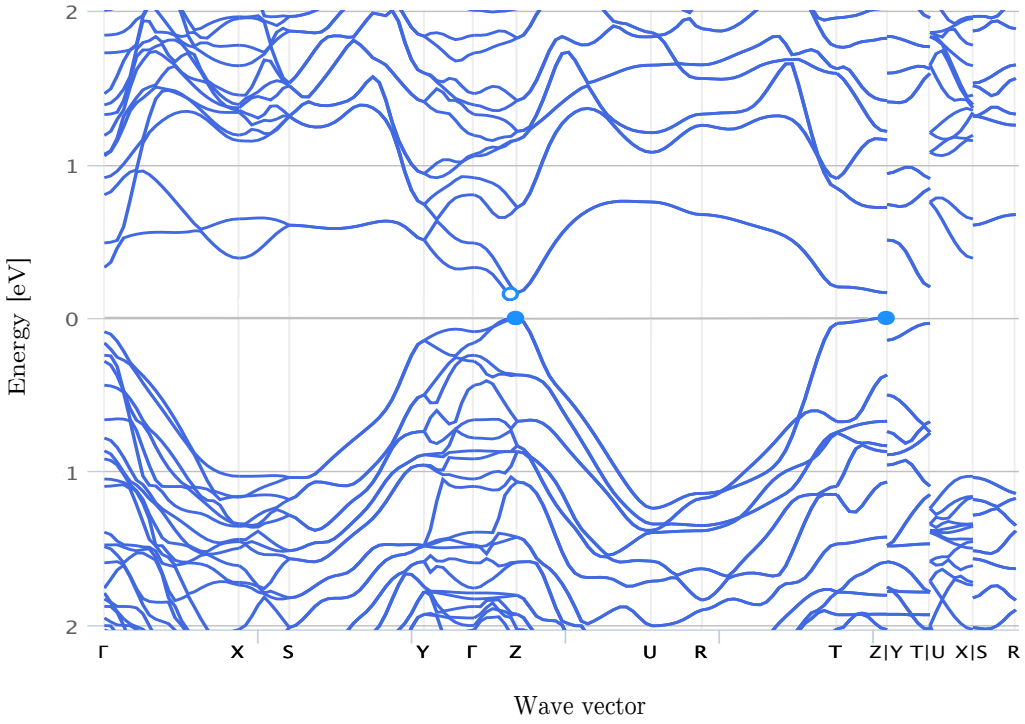

Figure 3.6: Electronic band structure of $Ca_5Al_2Sb_6$ from The Materials Project [30] (GGA).

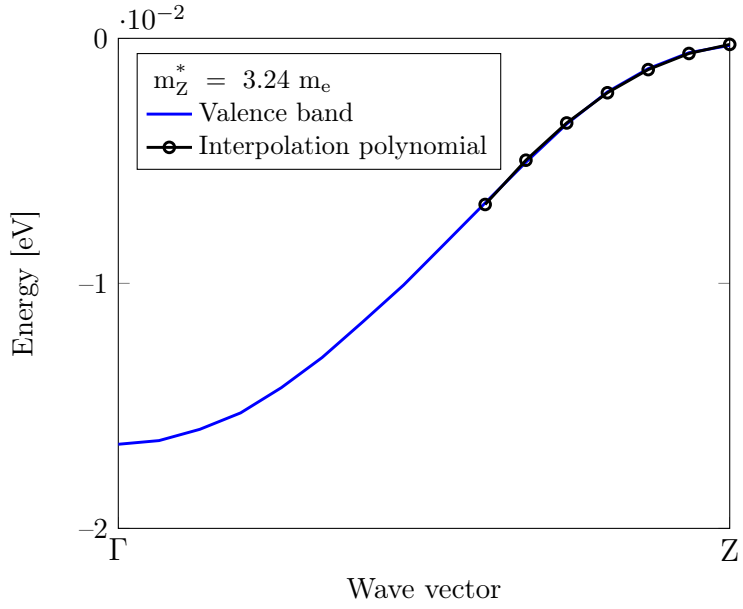

Figure 3.7: Valence band of $Ca_5Al_2Sb_6$ in the Z direction and the second order interpolation polynomial used to compute the effective mass m^*_Z.

high symmetry point Z, the effective masses under study are in the Z-U, Z-T and Z-Γ directions. With reference to the arrangement of high symmetry points represented in Figure 3.4, these are respectively noted m^*_X, m^*_Y and m^*_Z. For their computation, the valence band is interpolated with a second order polynomial. The second derivative of this polynomial is then simply the coefficient of the second order term and corresponds to $\partial^2\varepsilon/\partial k^2$. In this operation, the wave vectors have to be normalized with respect to the reciprocal lattice vectors. The interpolation polynomial of the valence band in the Z direction is illustrated in Figure 3.7.

The obtained values show the same trend as the literature (see Table 3.3). Effective masses in perpendicular directions to the covalent ladders (m^*_Y, m^*_Z) are clearly heavier than in the parallel direction of the chains (m^*_X). This pattern of lightest direction being parallel to the covalent substructure has been observed in other Zintl compounds, leading to the conclusion that this covalent network indeed takes the role of an electron crystal [32].

As explained in Section 1.3, a high electrical conductivity is searched in order to reach the highest figure of merit. A light effective mass, leading to a high mobility, is therefore interesting. However, a higher Seebeck is reached when the density of states is large near the band gap as stipulated by the Mott relation:

$$S = \frac{\pi^2}{3}\left(\frac{k_B^2 T}{e}\right)\left[\frac{d\ln(\sigma(\varepsilon))}{d\varepsilon}\right] \tag{3.2}$$

$$S = \frac{\pi^2}{3}\left(\frac{k_B^2 T}{e}\right)\left[\frac{1}{n}\frac{dn(\varepsilon)}{d\varepsilon} + \frac{1}{\mu}\frac{d\mu(\varepsilon)}{d\varepsilon}\right] \tag{3.3}$$

where n and μ are the carrier density and mobility. Since a large density of states is reflected by flat bands, the Seebeck coefficient will actually increase with heavier effective masses but also in case of degeneracy. The density of states effective mass, also called the band effective mass, characterizes these latter two parameters at a k point and is expressed by

$$m^*_{\text{band}} = (m^*_{d1} \cdot m^*_{d2} \cdot m^*_{d3})^{1/3} N_v^{2/3} \tag{3.4}$$

where d_i are the three perpendicular directions along a k point and N_v is the band degeneracy at this same point [27]. The Mott relation can then be reexpressed as

$$S = \frac{2k_B^2}{3e\hbar^2} m^*_{\text{band}} T \left(\frac{\pi}{3n}\right)^{2/3} \tag{3.5}$$

For $Ca_5Al_2Sb_6$, the band degeneracy is 2 at the Z point as it can be seen on the band structure in Figure 3.5 and the three inertial effective masses are the ones previously calculated. The band effective mass m^*_{band} at Z is then equal to 2.63 m_e. This value is much higher than for other thermoelectric (e.g. the band mass of PbTe is 0.3 m_e [33]). The combination of this heavy band effective mass and the very light effective mass m^*_{X} should lead to promising transport properties in the covalent ladders direction. Once the transport properties are computed, it will thus be relevant to analyse the anisotropy of the power factor, which summarizes both electrical conductivity and Seebeck coefficient.

Table 3.3: Comparison of the computed effective masses of $Ca_5Al_2Sb_6$ with the literature.

References	m^*_{X} $[m_e]$	m^*_{Y} $[m_e]$	m^*_{Z} $[m_e]$
Present work (LDA)	0.20	7.06	3.24
Snyder *et al.* [26] (GGA)	0.20	6.49	1.36

3.2.3 Density of states

The projected density of states was calculated and is represented in Figure 3.8. One can observe that Ca cations states are mainly localized in conduction band and that Sb states are dominant near the valence band edge. This density of states could also confirm the suppositions made from the EDD map on the covalent character of Sb–Al and Sb–Sb bonds. A covalent bond indeed results in the formation of bonding and antibonding states due to the overlap of atomic orbitals. In previous studies, these antibonding and bonding states were identified in the density of states [26, 29]. From – 6 to – 4.5 eV, the strong hybridization of Al and Sb electronic states is recognized as Al–Sb bonding states. The large density of Sb states near the band gap (–2 to 0 eV) is identified as Sb–Sb bonding states. Al–Sb anti-bonding states could correspond to the Al–Sb peak (1.5 eV) while the first peak (0.5 eV) likely corresponds to Sb–Sb antibonding states.

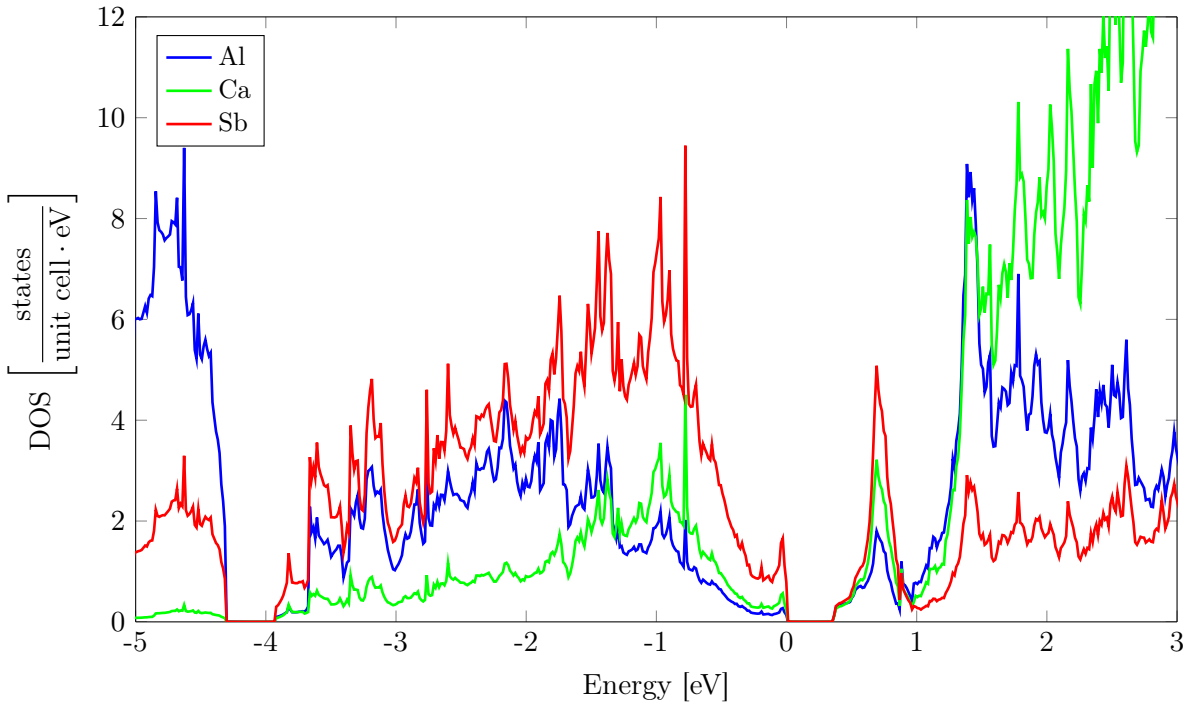

Figure 3.8: Density of states of $Ca_5Al_2Sb_6$.

While these identifications are not rigorously explained in the literature, the two identifications in the conduction band can actually be verified in regards of the density of states of Ca_3AlSb_3 (see Figure 4.6 on page 40). As it will be explained later, this other Zintl compound lacks Sb–Sb bonds between each $AlSb_4$ tetrahedra and therefore their relative states. Since the peak identified here above as resulting from Sb–Sb anti-bonding states is not present in the density of states of Ca_3AlSb_3, it confirms its identification.

3.3 Transport properties in constant relaxation time approximation

Now that the band structure has been computed, the transport properties can be calculated. In this section, a constant relaxation time of 10^{-14}s is considered as it was initially implemented in BoltzTrap. The experimental study « Improved carrier concentration control in Zn-doped $Ca_5Al_2Sb_6$ » published by Snyder's group [34] was taken as a reference to compare with these computed results. In this experimental study, the carrier concentrations of different samples of doped $Ca_5Al_2Sb_6$ are measured using the Hall effect. The evolution with the temperature of these Hall carrier concentrations is shown in Figure 3.9.

3.3.1 Seebeck coefficient

The Seebeck coefficient of $Ca_5Al_2Sb_6$ was firstly computed in this analysis. It is indeed a good indicator of the accuracy of the input band structure when working with a constant relaxation time. Indeed, since it is constant, the latter does not need to be taken into account in the energy

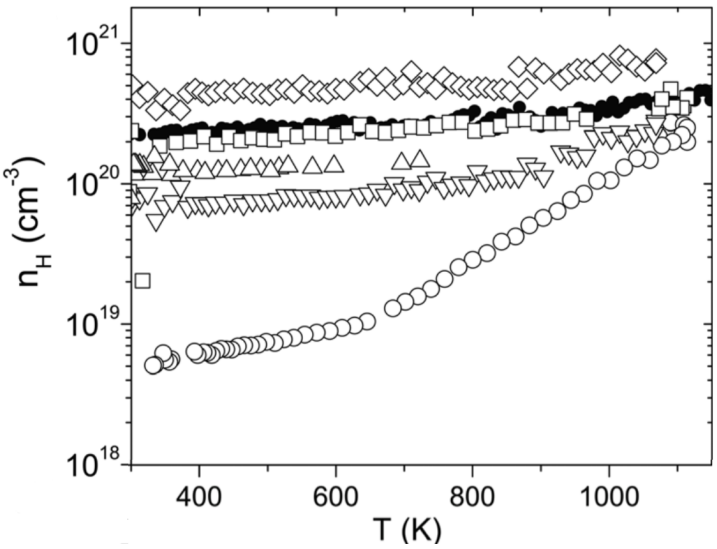

Figure 3.9: Hall carrier concentrations of several Zn-doped $Ca_5Al_2Sb_6$ samples. Extracted from Ref. [34].

integral in equation (2.30) and will be simplified by the electrical conductivity in the denominator. Therefore, the Seebeck coefficient does not depend on its value but only its energy variation, which is not taken into account here. Then, as said previously, the band gap of the electronic structure is largely underestimated from the density functional theory. Since the shape of the Seebeck coefficient varies with this band gap (in particular with $S_{\max} = E_{\text{gap}}/(2eT_{\max})$), it is thus appropriate to manually shift the computed eigenvalues for the conduction bands so that the gap matches the experimental value (0.50 eV, see Table 4.2).

The evolution of the Seebeck coefficient with the temperature is shown in Figure 3.10 for different doping levels corresponding to the experimental Hall carrier concentrations presented in the article. Both experimental results (marked line) and calculated values (simple line) are shown. It is important to note that although the legend only indicates the global doping level for calculated results, the evolution of the concentration shown in Figure 3.9 was actually taken into account. Even if not stated in the legend of every graph in this thesis for the sake of clarity, all concentrations are given in cm^{-3}.

One can firstly observe that the Seebeck coefficient decreases with the doping level, as expected from the Mott relation (3.5). The red curve, related to an extrinsically undoped sample of $Ca_5Al_2Sb_6$ ($p = 5{\cdot}10^{18}$ cm^{-3}), decreases much more than the others with the temperature. The intrinsic carrier generation is indeed more significant since the overall carrier concentration is lower than for other samples. At higher doping level, this intrinsic generation becomes insignificant compared to the extrinsic doping level, which is why other curves do not decrease in this range of temperature. Theoretical values are in good agreement with experimental data for low carrier concentrations but begin to space for doping levels higher than $p = 2{\cdot}10^{20}$ cm^{-3}. Three possible reasons for this erroneous shift were identified and tested. First of all, the Seebeck

coefficients were recalculated while considering Hall carrier concentrations instead of doping levels, since experimental results are actually given in function of the Hall carrier concentrations. However, it did not correct this error. This shift was also suspected to be due to the constant relaxation time approximation which neglects its possible energy dependence. This hypothesis is tested later in this report when the energy and temperature dependence of the relaxation time are found but do not solve this shift. Finally, as explained previously in Subsection 2.2.4, the approximation of rigid bands is made in BoltzTraP, which means that the shape of the bands is considered to be independent of the doping level. Since the Seebeck coefficient indeed varies with the band gap, neglecting its variation with the doping level could be the reason for this shift. The fact that this shift only appears for high doping levels seems to confirm this hypothesis, since the rigid band approximation is indeed less valid for higher doping levels.

3.3.2 Electrical conductivity

The next step is to study the electrical conductivity, which in turn depends on the value of the relaxation time, as seen in equation (2.29). It is done through the study of the electrical resistivity since this form will lead to an easier lecture while studying scattering mechanisms later in Chapter 5. Calculated and experimental resistivities of each sample are illustrated in Figure 3.11. The electrical resistivity of the undoped sample (red curve) is once again decreasing more than other samples with the temperature. The explanation remains the same as for the Seebeck coefficient: the intrinsic carrier generation is significant compared to the overall carrier concentration. One can then observe that the use of a constant relaxation time of $\tau = 10^{-14}$s leads a correct average value of the resistivity for each doping level. Since the temperature dependence of the relaxation time is neglected when this one is considered as constant, an electrical resistivity largely varying with the temperature, like the one of $Ca_5Al_2Sb_6$ at low temperature, cannot be reproduced. But since the resistivity at higher temperature is almost constant, the constant relaxation time approximation gives very reasonable results.

This constant behaviour is in fact interesting for thermoelectric properties since a constant electrical resistivity and electronic thermal conductivity above 650 K should lead to a flatter figure of merit above this temperature. Of course, since the Seebeck coefficient still varies with the temperature, this figure of merit will not be exactly flat, but it could be closer to its best for a range of temperature instead of just a specific one. This could facilitate the use of $Ca_5Al_2Sb_6$ in thermoelectric applications. While this constant behaviour remains uncommented in the literature, an investigation of electron scattering mechanisms in Chapter 5 will help to understand it. It should also allow one to understand the variation with the doping level of this resistivity.

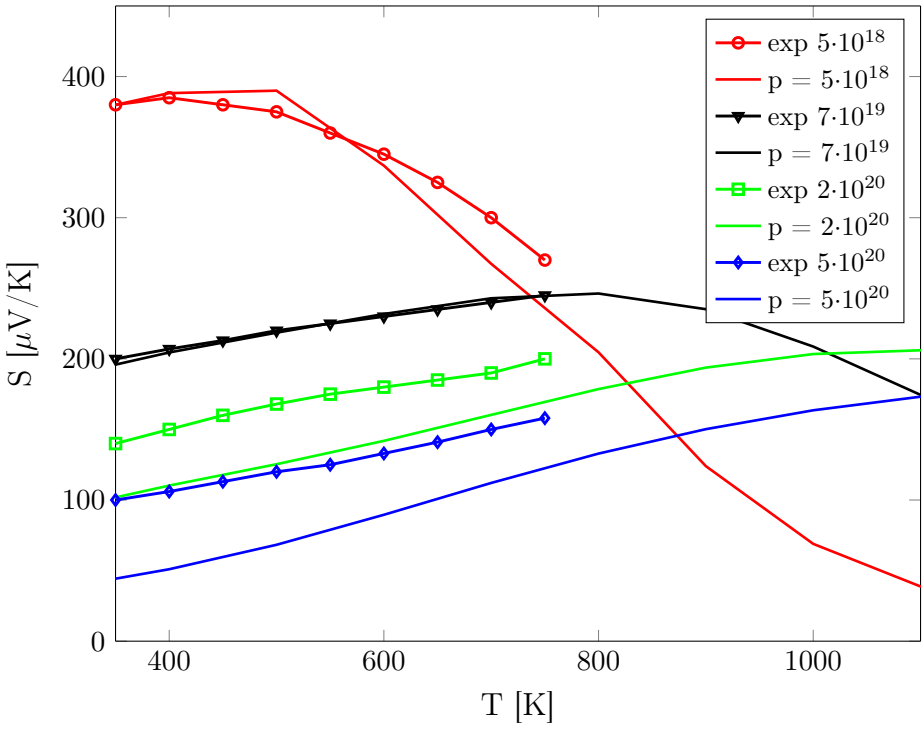

Figure 3.10: Seebeck coefficient of $Ca_5Al_2Sb_6$ at different doping levels.

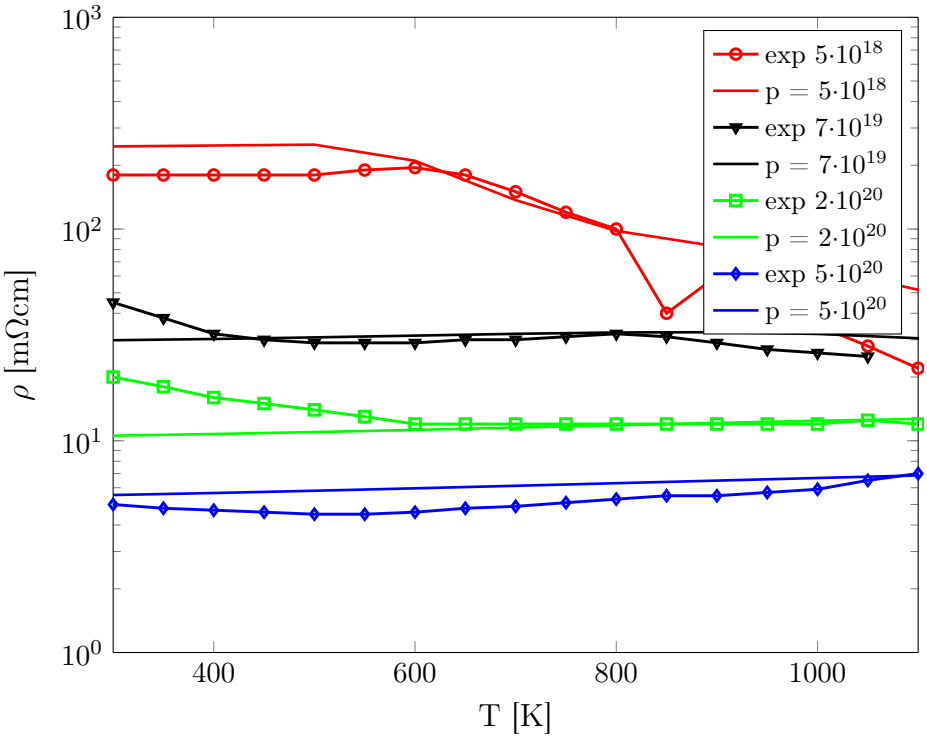

Figure 3.11: Electrical resistivity of $Ca_5Al_2Sb_6$ at different doping levels.

Chapter 4

Basic *ab initio* study of Ca_3AlSb_3

Contents

This chapter aims to study the transport properties of the Zintl compound Ca_3AlSb_3. As for the previous chapter, the unit cell is firstly presented and a complete structural relaxation is performed. An electron density difference is computed once again to confirm the covalent character of the substructure. The electronic structure and the density of states are computed and used to calculate the electronic transport properties of Ca_3AlSb_3. The validity of a constant relaxation time is discussed through a comparison with experimental results.

4.1 Ca_3AlSb_3 crystal [3, 26]

4.1.1 Unit cell

The Zintl compound Ca_3AlSb_3 has an orthorhombic unit cell (space group *Pnma*, no. 62 in the Hermann Mauguin notation). Representations of these structure are shown in Figures 4.1 and 4.2. As for the $Ca_5Al_2Sb_6$ compound, $AlSb_4$ tetrahedra are also forming chains, i.e. anionic substructures. Concerning the overall charge balance, this phase can be written as $Ca_3{}^{+2}Al^{-1}Sb_2{}^{-2}Sb^{-1}$. Each aluminium atom in a tetrahedron bonds with the four surrounding antimony atoms and has therefore a valence state of -1. The antimony atoms linking two tetrahedra have a valence state of -1. The rest of antimony will have only one bond, meaning their valence state is -2. Compared to the $Ca_5Al_2Sb_6$ compound, this Zintl phase has an extra Ca^{2+} cation whose electrons correctly balance the overall charge. There is therefore no Sb–Sb bond between the $AlSb_4$ chains. An electron density difference map of Ca_3AlSb_3 was computed to confirm the covalent character of Al–Sb bonds of the substructure. This map is shown in Figure 4.3.

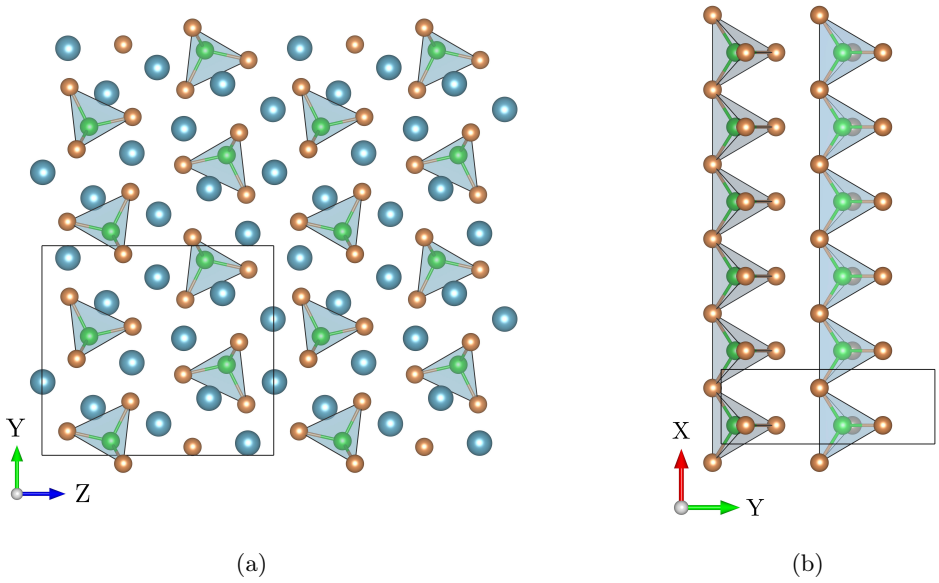

Figure 4.1: Structural representation of (a) the orthorombic unit cell of Ca_3AlSb_3 shown in the [100] direction and of (b) the ladder-like tetrahedral chains extending along the [100] direction. Ca atoms are represented in blue, Sb atoms in orange and Al atoms in green.

4.1.2 Structural relaxation

The same structural relaxation as for $Ca_5Al_2Sb_6$ was performed on Ca_3AlSb_3 with an identical criterion of accuracy. The lattice constants are correctly converged for a cut-off energy of 15 Ha and a $6\times6\times6$ k-points grid, i.e. the same parameters as for $Ca_5Al_2Sb_6$. A comparison between the converged lattice constants and those from the literature show good agreement (see Table 4.1). The relaxed reduced coordinates can be found in Table B.2 in the Appendix B.

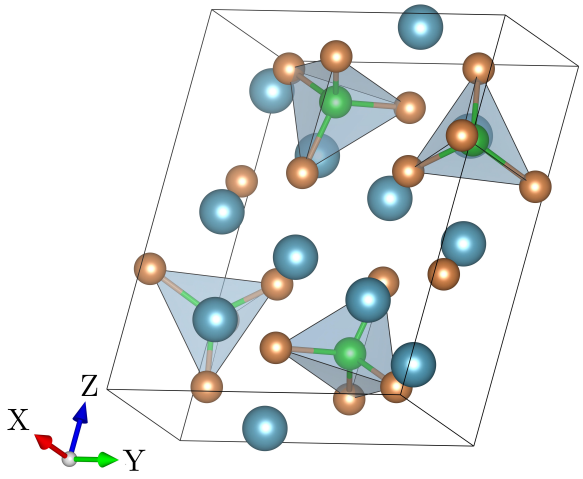

Figure 4.2: Unit cell of Ca_3AlSb_3.

Table 4.1: Comparison of the computed lattice parameters of Ca_3AlSb_3 with the literature.

References	x [Å]	y [Å]	z [Å]
Present work (LDA)	4.53	13.01	14.39
Yan, Wang *et al.* (GGA) [35]	4.51	12.96	14.34

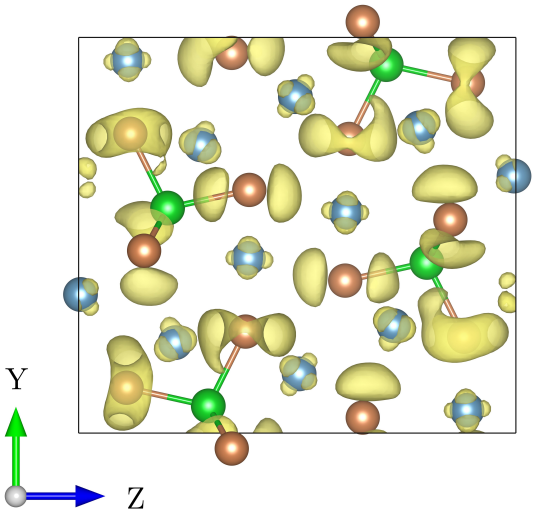

Figure 4.3: Electron density difference map of Ca_3AlSb_3.

4.2 Electronic structure calculations

The integration path in the Brillouin zone used for $Ca_5Al_2Sb_6$ remains appropriate for Ca_3AlSb_3 as it is also an orthorhombic unit cell.

4.2.1 Electronic band structure

The computed electronic band structure (LDA) is represented in Figure 4.4 while the corresponding band structure extracted from The Materials Project (GGA) is shown in Figure 4.5. These two are very similar and present a direct band gap in Γ. The band gap size differs since the exchange-correlation approximations are different. A comparison with several band gaps from experimental and theoretical studies show good agreement (see Table 4.2).

Table 4.2: Comparison of the computed band gap value of Ca_3AlSb_3 with the literature.

References	Theoretical band gap [eV]	Experimental band gap [eV]
Present work	0.67 (LDA)	–
The Materials Project [30]	0.29 (GGA)	–
Yan, Wang *et al.* [35]	0.71 (GGA)	0.65
Snyder *et al.* [3]	–	0.60

4.2.2 Effective masses

As done previously, the calculation of effective masses through the derivation of an interpolation polynomial allows one to study the anisotropy of this Zintl structure. The calculated values are given in Table 4.3 and exhibit the same trend as in the literature. The effective masses are indeed nearly isotropic, which is due to the parabolic dispersion of the valence band at the edge. The transport properties should follow this isotropy. These effective masses are smaller than the ones of $Ca_5Al_2Sb_6$ and lead to a smaller band effective mass m^*_{band} equal to 1.31 m_e. One can therefore expect to find a higher Seebeck coefficient for $Ca_5Al_2Sb_6$ while Ca_3AlSb_3 will reach a higher average electrical conductivity as its inertial effective masses are lighter.

Table 4.3: Comparison of the computed effective masses of Ca_3AlSb_3 with the literature.

References	m^*_X $[m_e]$	m^*_Y $[m_e]$	m^*_Z $[m_e]$
Present work (LDA)	0.86	0.79	0.84
Yan, Wang *et al.* [35]	0.67	0.57	0.62

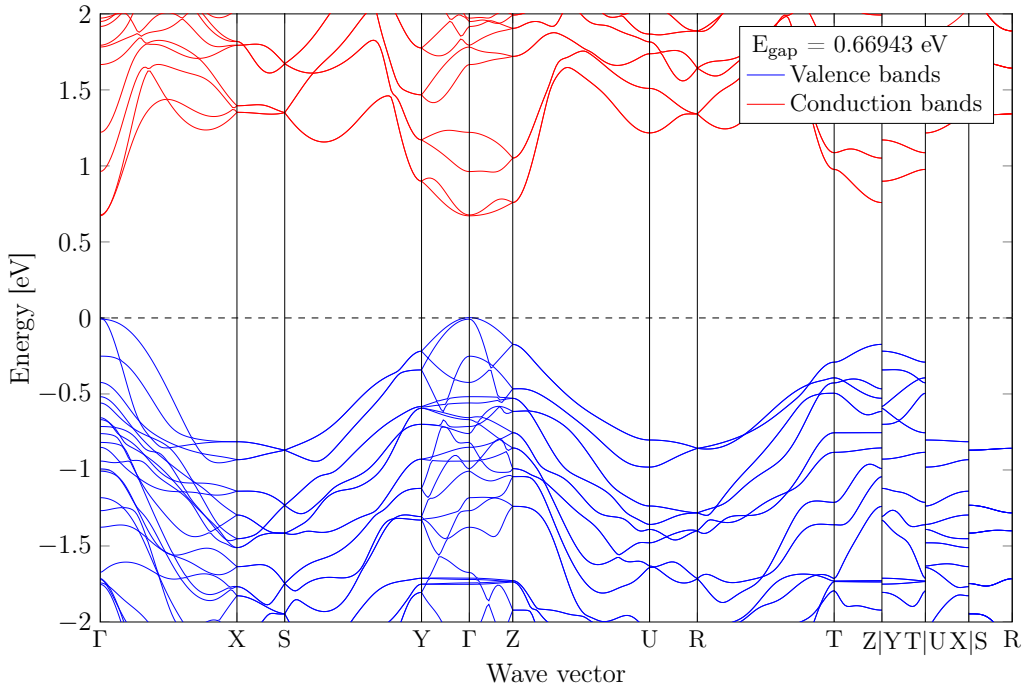

Figure 4.4: Electronic band structure of Ca_3AlSb_3 (LDA).

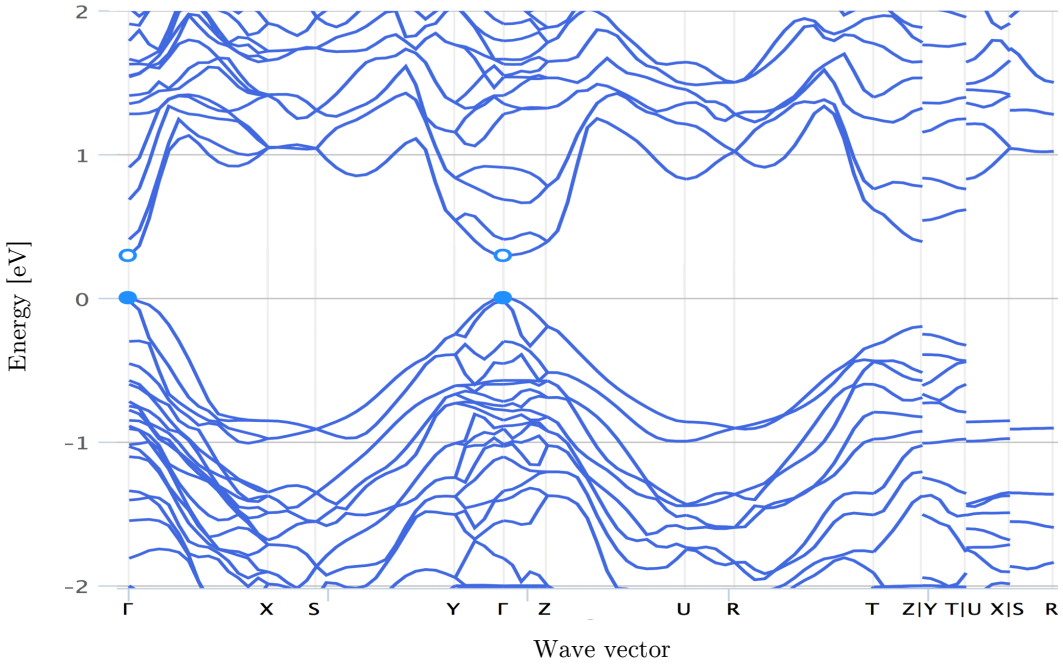

Figure 4.5: Electronic band structure of Ca_3AlSb_3 from The Materials Project [30] (GGA).

4.2.3 Density of states

The projected density of states was calculated for Ca_3AlSb_3 (see Figure 4.6). The same analysis as for $Ca_5Al_2Sb_6$ is done to identify the bonding and antibonding Al–Sb states. As announced previously, there is no important antimony peak at 0.5 eV in the conduction band since this Zintl compound lacks the Sb–Sb bonds between each tetrahedron. Here again Sb states are dominant near the valence band edge and Ca states are localized in the conduction band.

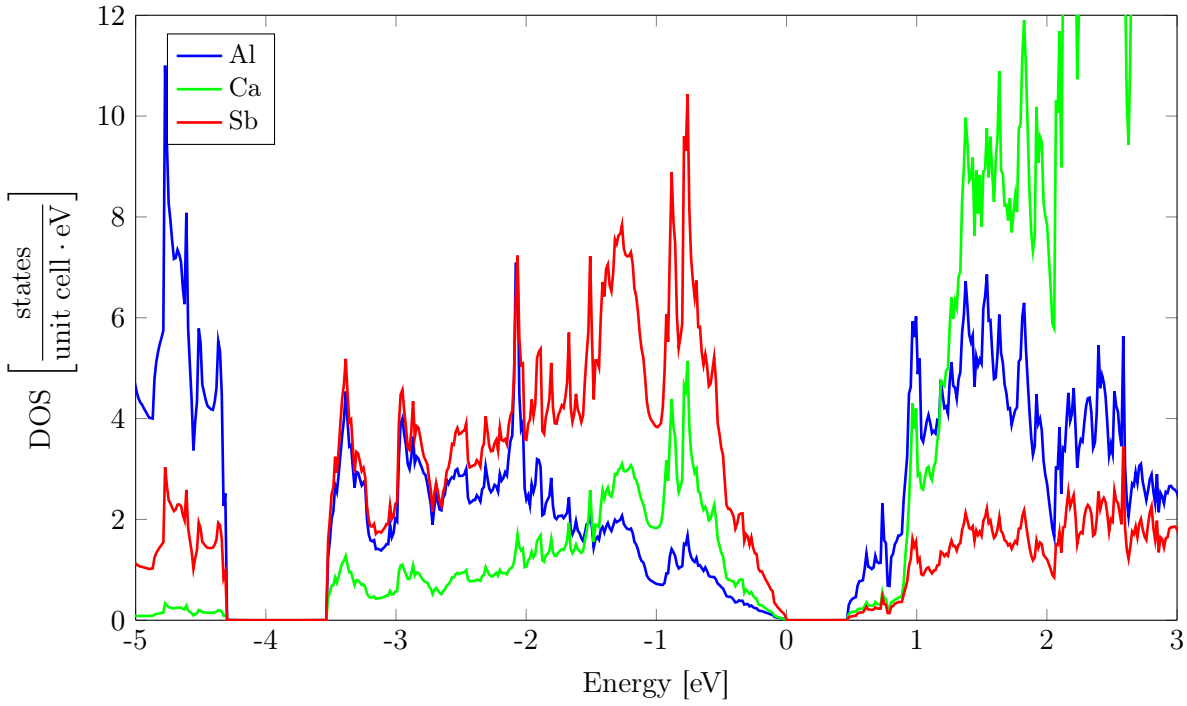

Figure 4.6: Density of states of $CaAlSb_3$.

4.3 Transport properties in constant relaxation time approximation

As in the previous chapter, the transport properties of Ca_3AlSb_3 were firstly studied using a constant relaxation time. The article « Ca_3AlSb_3: an inexpensive, non-toxic thermoelectric material for waste heat recovery » published by Snyder's group [3] was used for experimental comparison. The evolution of the Hall carriers concentrations with temperature for the four doped samples considered in the article is illustrated in Figure 4.7.

4.3.1 Seebeck coefficient

The band gap of Ca_3AlSb_3 was shifted to 0.6 eV to match the experimental value. The Seebeck coefficient was calculated for specific doping levels corresponding to the experimental samples. One can observe in Figure 4.8 that these coefficients are not exactly correctly reproduced, especially at low temperature. It will thus be interesting to recalculate this coefficient once the dominant electron scattering mechanisms are identified in the following chapter, i.e. once a

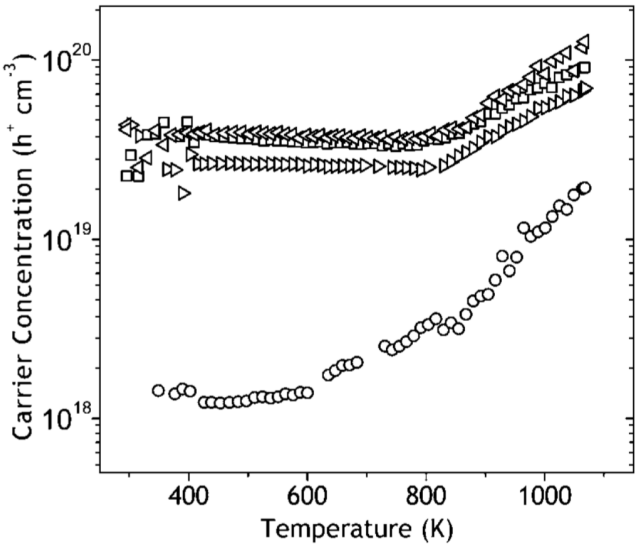

Figure 4.7: Hall carrier concentrations of several Na-doped Ca_3AlSb_3 samples. Extracted from Ref. [3].

temperature and energy dependent relaxation time is obtained, to check if this fit improves. By comparing Seebeck coefficients of both Zintl phases at nearly identical doping levels ($7{\cdot}10^{19}$ and $5{\cdot}10^{19}$ cm^{-3}), one can clearly see that the Seebeck coefficient of $Ca_5Al_2Sb_6$ is much higher than the one of Ca_3AlSb_3. This difference was indeed expected from the higher band mass of $Ca_5Al_2Sb_6$.

4.3.2 Electrical conductivity

The electrical resistivities of the different samples are shown in Figure 4.9. Unlike for $Ca_5Al_2Sb_6$, a constant relaxation time of 10^{-14}s gave incorrect results for this phase. Its value must in fact be increased to $4 \cdot 10^{-14}$s to best fit the experimental electrical resistivities. This higher relaxation time means that the time between two consecutive scattering events of an electron is longer, which is beneficial since it leads to lower resistivities. For a same doping level, the resistivity of Ca_3AlSb_3 is therefore smaller than the one of $Ca_5Al_2Sb_6$. The resistivity of Ca_3AlSb_3 is also constant at high temperature, which must be due to both the intrinsic carrier generation and a specific combination of electron scattering mechanisms. It allows a constant relaxation time to give correct results in this range of temperature. The large decrease at low temperature is logically not caught by the computed resistivity, but since the temperatures of interest for thermoelectricity are the high ones (corresponding to low resistivities), it does not really matter. Finally, one can notice that the variation of the resistivity with the doping level is smaller than for $Ca_5Al_2Sb_6$. As said previously, a deeper investigation of the electron scattering mechanisms in the following chapter should allows one to correctly reproduce experimental results. It should also help to understand the reasons for both the constant behaviour of the resistivity at high temperature and its smaller variation with the doping level than for $Ca_5Al_2Sb_6$.

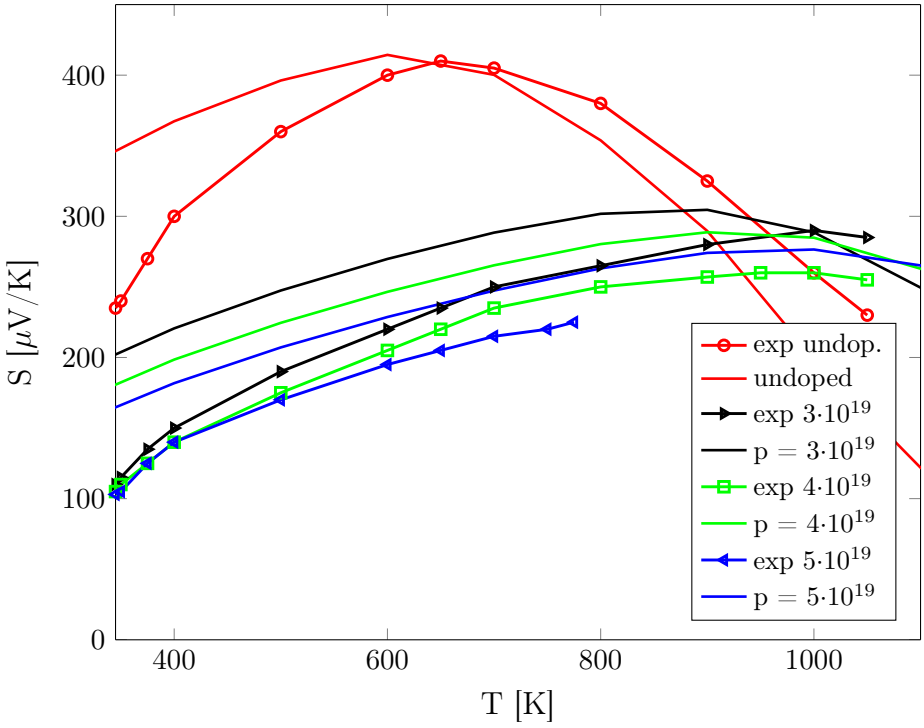

Figure 4.8: Seebeck coefficient of Ca_3AlSb_3 at different doping levels.

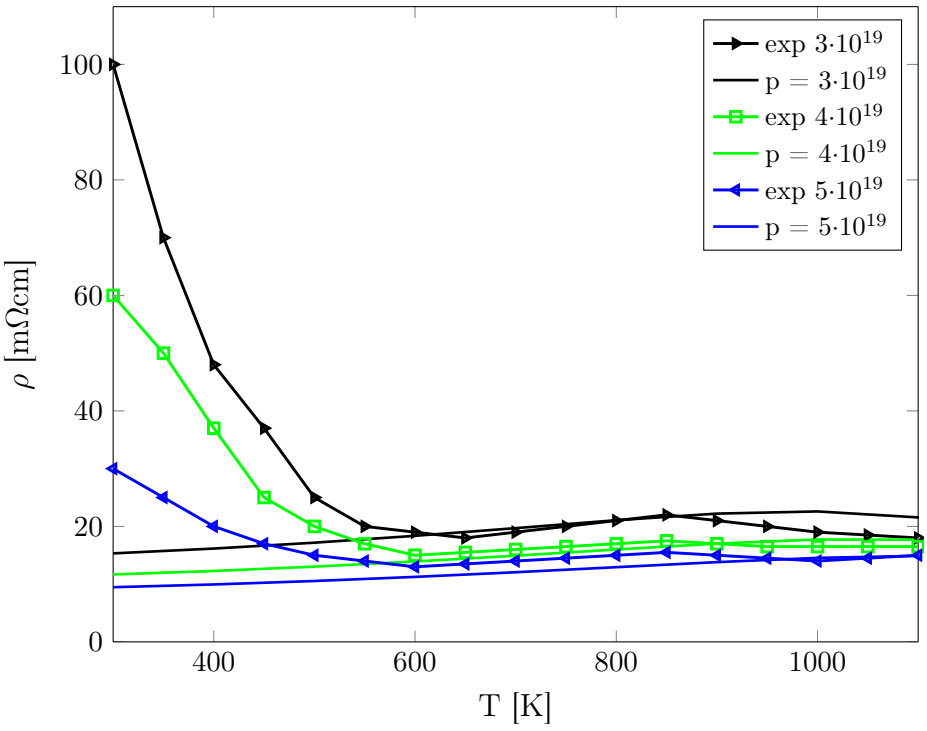

Figure 4.9: Electrical resistivity of Ca_3AlSb_3 at different doping levels.

Chapter 5

Electron scattering mechanisms

Contents

In the previous chapters, the relaxation time was considered as constant. This approach gave satisfying results for both Zintl compounds at high temperature, which is quite unusual (e.g. the electrical resistivity of PbTe with a constant relaxation time is not even close to experimental results [36], the energy and temperature dependency must be taken into account). This validity is due to the unusual constant behaviour of the electrical resistivity with the temperature. This chapter is therefore devoted to the study of the different electron scattering mechanisms influencing the energy and the temperature dependences of the total relaxation time, i.e. the electrical resistivity, in the Zintl phases $Ca_5Al_2Sb_6$ and Ca_3AlSb_3. This analysis should in particular reveal the origin of the constant behaviour of the resistivity. It should also explain the different behaviours of the electrical resistivities with the doping level for both Zintl compounds. The working procedure was firstly to implement relaxation times corresponding to specific scattering mechanisms in BoltzTraP and fit them on experimental results. This fitting allowed one to identify ionized impurity and acoustic phonon scattering as the dominant mechanisms. They are

described in the first part of this chapter and analytical expressions of their relative relaxation time are derived. Their combination explains the constant resistivity and therefore the validity of the constant relaxation time approximation. As shown by the experimental fitting, the acoustic phonon scattering differs the most between $Ca_5Al_2Sb_6$ and Ca_3AlSb_3. This mechanism is therefore theoretically investigated and its diverse contributions – the deformation potential constants, the sound velocities and the band effective masses – were computed with ABINIT. This investigation explains the origins of the different behaviours of the electrical resistivities with the doping level of these two materials at high temperature.

5.1 Relaxation times

An analytical expression for the variation in time of the electronic distribution function due to scattering was found under the relaxation time approximation in Subsection 2.2.2:

$$\left(\frac{df}{dt}\right)_{\text{scat.}} = -\frac{f_1(\mathbf{k})}{\tau(\mathbf{k})} = -\frac{f(\mathbf{k}) - f_0(\mathbf{k})}{\tau(\mathbf{k})} \tag{5.1}$$

where

$$\frac{1}{\tau(\mathbf{k})} = \sum_{\mathbf{k}'} W(\mathbf{k}, \mathbf{k}') \left[1 - \frac{f_1(\mathbf{k})}{f_1(\mathbf{k}')}\right] \tag{5.2}$$

While the relaxation time in previous chapters was considered as constant, one can deduct from equation (5.2) that it actually depends on the state transition probability $W(\mathbf{k}, \mathbf{k}')$. Considering simple parabolic bands[1], expressions of this probability can be derived using the non-stationary perturbation theory for both ionized impurity and acoustic phonon scattering. These two mechanisms were firstly chosen for analysis since they are known to be dominant in Zintl phases [3,34]. The experimental fitting will tell if these contributions are sufficient to reproduce experimental results. The general electronic Hamiltonian in a real lattice is expressed as

$$\hat{H}_T = \hat{H} + \hat{H}' \tag{5.3}$$

where $\hat{H}'$ is the disturbed Hamiltonian, which describes electron-impurity or electron-phonon interactions, and $\hat{H}$ is the undisturbed Hamiltonian. In the case of ionized impurity scattering, the latter is the electronic Hamiltonian in an ideal lattice, but when acoustic phonon scattering is considered, it is the Hamiltonian of an ideal phonon gas non interacting with electrons. Solving these Hamiltonians with the assumption of a small disturbance ($\hat{H}' \ll \hat{H}$) leads to a specific transition probability for each scattering mechanism. The final transition probabilities given here below can then be used to express the corresponding relaxation time. Full developments of their derivation can be found in Refs. [19, 20].

[1] This consideration of parabolic bands correctly stands for the valence band of Ca_3AlSb_3 while the one of $Ca_5Al_2Sb_6$ is much more anisotropic. However, this assumption was still used for the sake of simplicity.

5.1.1 Ionized impurity scattering

When electrons are scattered by impurities, the transition probability is

$$W(\mathbf{k},\mathbf{k}') = \frac{2\pi}{\hbar}\frac{N_i}{V}\left|\int U(\mathbf{r})e^{i(\mathbf{k}\text{ - }\mathbf{k}',\mathbf{r})}d\mathbf{r}\right|^2 \delta(\varepsilon_{\mathbf{k}} - \varepsilon_{\mathbf{k}'}) \tag{5.4}$$

where N_i is the impurity atom concentration, V is the crystal volume, $U(\mathbf{r})$ is the disturbance potential and the δ function expresses the energy conservation, i.e. the condition for this scattering to be elastic. When considering ionized impurity scattering, relevant in the case of a doped semiconductor, this expression needs to be modified. Indeed, since impurities from the doping are located on energy levels close to the valence band for p-type semiconductor, they are easily ionized even at low temperature. A long-range Coulomb field is then generated by every ionized impurity, whose potential is written as

$$\phi = \frac{\pm e}{\chi r} \tag{5.5}$$

where r is the position of the ionized impurity in the semiconductor, $\pm e$ is the ion charge and χ is the dielectric constant of the crystal. For the relaxation time to converge ($r \to \infty, \tau(k) \to 0$), one has to consider the Coulomb potential screening by charge carriers. The potential of a single ionized impurity atom at a distance r from the ion location can then be presented as

$$\phi(r) = \left(\frac{\pm e}{\chi r}\right) e^{-r/r_0} \tag{5.6}$$

where r_0 is referred to the radius of ion field screening and is generally defined by the formula

$$r_0^{-2} = \left(\frac{4\pi e^2}{\chi}\right)\int -\left(\frac{\partial f_0(\varepsilon)}{\partial \varepsilon}\right) g(\varepsilon)d\varepsilon \tag{5.7}$$

where $f_0(\varepsilon)$ is the equilibrium electron distribution function and $g(\varepsilon)$ is the density of states. The scattering potential is finally expressed as

$$U(r) = e\phi(r) = \left(\frac{\pm e^2}{\chi r}\right) e^{-r/r_0} \tag{5.8}$$

Once its expression is considered in the formulation of the transition probability, it leads to

$$W(\mathbf{k},\mathbf{k}') = \frac{2\pi}{\hbar}\frac{N_i}{V}\left(\frac{4\pi e^2}{\chi}\right)^2 \frac{\delta(\varepsilon_{\mathbf{k}} - \varepsilon_{\mathbf{k}'})}{[(\mathbf{k}-\mathbf{k}')^{\mathbf{2}} + \mathbf{r_0^{-2}}]^{\mathbf{2}}} \tag{5.9}$$

Since this scattering mechanism is elastic, it is characterized by its relative relaxation time. Considering that the root of $\varepsilon(\mathbf{k}') = \varepsilon(\mathbf{k})$ is $k' = k$ and using equation (5.9) in equation (5.2) allows one to formulate it as

$$\tau(k) = \frac{\hbar\chi^2}{2\pi e^4 N_i F_{imp}(k)} k^2 \left(\frac{\partial\varepsilon}{\partial k}\right) \tag{5.10}$$

In the assumption of a simple parabolic band, this relaxation time can be reformulated as

$$\tau(\varepsilon) = \frac{\chi^2 (2m^*_{\text{band}})^{1/2} (k_B T)^{3/2}}{\pi e^4 N_i F_{imp}(\varepsilon)} \left(\frac{\varepsilon}{k_B T}\right)^{3/2} \tag{5.11}$$

where

$$F_{imp}(k) = ln(1+\zeta) - \zeta/(1+\zeta) \quad \text{with} \quad \zeta = \frac{8m^*_{\text{band}}\varepsilon r_0^2}{\hbar^2} \tag{5.12}$$

$$r_0 = \left(\frac{\chi k_B T}{4\pi e^2 n}\right)^2 \tag{5.13}$$

It can be seen from equation (5.11) that the relaxation time τ does not directly depends on the temperature but varies with $\varepsilon^{3/2}$.

5.1.2 Acoustic phonon scattering

Bose-Einstein distribution function for phonons of frequency $\omega_j(\mathbf{q})$ is

$$N_q = N(\hbar\omega_j(\mathbf{q})) = N_{\mathbf{q}j} = \frac{1}{e^{\hbar\omega_j(\mathbf{q})/k_B T} - 1} \tag{5.14}$$

where N_q is the number of phonons and j is a reference to the number of branches of the frequency spectrum ($j = 1, 2, ..., 3s$) with s the number of atoms. The phonon number thus increases with the temperature so that this mechanism should probably be more important at high temperature. The Hamiltonian of the undisturbed case $\hat{H}$ and the disturbed case $\hat{H}'$ must be found. The first one is a combination of both electronic Hamiltonian $\hat{H}_e$ and lattice Hamiltonian $\hat{H}_{lat}$ and leads to a first expression of transition probability:

$$W(\mathbf{k}, \mathbf{k}') = \sum_{\widetilde{N}'_{\mathbf{q}j}} W(\mathbf{k}\widetilde{N}_{\mathbf{q}j}, \mathbf{k}'\widetilde{N}'_{\mathbf{q}j}) \tag{5.15}$$

where $\widetilde{N}'_{\mathbf{q}j}$ are the oscillation quantum numbers. This is actually a sum over all the finite states of the phonon system of the following transition probability:

$$W(\mathbf{k}\widetilde{N}_{\mathbf{q}j}, \mathbf{k}'\widetilde{N}'_{\mathbf{q}j}) = 2\pi\hbar^{-1}|\langle \mathbf{k}'\widetilde{N}'_{\mathbf{q}j}|\hat{H}'|\mathbf{k}\widetilde{N}_{\mathbf{q}j}\rangle|^2\delta \times [\varepsilon_{\mathbf{k}'} - \varepsilon_{\mathbf{k}} + \sum_{qj}(N'_{\mathbf{q}j} - N_{\mathbf{q}j})\hbar\omega_j(\mathbf{q})] \tag{5.16}$$

The first left term on the right side corresponds to the electronic Hamiltonian while the second term is the lattice Hamiltonian. The electronic Hamiltonian requires the explicit form of the disturbed Hamiltonian corresponding to electron-lattice interaction. A method was developed by Bardeen and Shockley to characterize this interaction for acoustic phonon [37]. A phonon being an elastic wave propagating in a crystal, the latter deforms, i.e. each atom in the unit cell moves along a shift vector. Since the electronic structure depends on the lattice constants, this deformation therefore leads in particular to a shift of the valence energy band. This interaction is called the deformation potential and is defined as

$$\hat{H}'_{ac} = E_1 \nabla \cdot \mathbf{u}_{ac}(\mathbf{r}) \tag{5.17}$$

where E_1 is the deformation potential constant and $\mathbf{u}_{ac}(\mathbf{r})$ is the shift vector. Substituting this interaction Hamiltonian in the electronic Hamiltonian leads, after several operations, to a new expression of the transition probability:

$$W_{ac}(\mathbf{k}, \mathbf{k}') = \sum_{\mathbf{q}} w_1(q)[A^+_{\mathbf{k}\mathbf{k}'}(\mathbf{q}) + A^-_{\mathbf{k}\mathbf{k}'}(\mathbf{q})] \tag{5.18}$$

where

$$A^{\pm}_{\mathbf{k}\mathbf{k}'}(\mathbf{q}) = (N_q + \frac{1}{2} \mp \frac{1}{2})\delta(\varepsilon_{\mathbf{k}'} - \varepsilon_{\mathbf{k}} \mp \hbar\omega(\mathbf{q}))\delta_{\mathbf{k}',\mathbf{k}+\mathbf{q}} \tag{5.19}$$

$$w_1(q) = \frac{\pi E_1^2 q^2}{NM\omega(q)} \tag{5.20}$$

where $w(q)$ is the longitudinal acoustic phonon frequency (with $\omega(\mathbf{q} = 0) = 0$ for acoustic phonons), N_q the number of phonons given by the Bose Einstein distribution function (5.14), N the number of unit cells and M the unit cell mass. The term $A^+_{\mathbf{k}\mathbf{k}'}$ refers to the transitions due to phonon absorption while $A^-_{\mathbf{k}\mathbf{k}'}$ is related to phonon emission. The δ function and symbol are respectively linked to the energy and impulse conservation. This scattering mechanism must be elastic in order to be characterized by a relaxation time. The energy of emitted or absorbed phonon must thus be negligible in comparison of charge carrier energy ($\hbar\omega(q) \ll k_B T$). These conditions allow to neglect the phonon energy in the δ function in equation (5.19) and to expand the Bose-Einstein distribution to

$$N_q + 1 \approx N_q \approx k_B T/\hbar\omega(q) \tag{5.21}$$

Considering these approximations and the fact that $\omega(q) = v_0 q$ stands for acoustic branches (where v_0 is the sound velocity), one can rewrite the general expression of the transition probability as

$$W_{ac}(\mathbf{k}, \mathbf{k}') = \frac{2\pi}{MN} \frac{E_1^2}{\hbar v_0^2} k_B T \delta(\varepsilon_{\mathbf{k}'} - \varepsilon_{\mathbf{k}}) \tag{5.22}$$

Using equation (5.2) and by turning the summation over $\mathbf{k}$ into an integral, the relaxation time can be expressed as

$$\tau(k) = \frac{\pi \hbar d}{E_1^2} \frac{v_0^2}{k_B T} \frac{1}{k^2} \left(\frac{\partial \varepsilon}{\partial k} \right) \tag{5.23}$$

where $d = MN/V$ is the crytal density. When the band is considered as parabolic, the latter expression can be rewritten as

$$\tau(\varepsilon) = \frac{2\pi \hbar^4 d v_0^2}{E_1^2 (2 m^*_{\text{band}} k_B T)^{3/2}} \left(\frac{\varepsilon}{k_B T} \right)^{-1/2} \tag{5.24}$$

For the acoustic phonon scattering, the related relaxation time thus varies with $\tau \sim T^{-1} \varepsilon^{-1/2}$.

5.1.3 Implementation in BoltzTraP

The global relaxation time is computed by summing the contributions of scattering due to ionized impurities (II) and to acoustic phonons (AP) using Matthiessen's law:

$$\frac{1}{\tau_{\text{TOT}}} = \frac{1}{\tau_{\text{II}}} + \frac{1}{\tau_{\text{AP}}} \tag{5.25}$$

The BoltzTraP code actually allows one to implement an energy and temperature dependent relaxation time through the expression

$$\tau(\varepsilon, T) = \tau_0 \left(\frac{T}{T_0} \right)^s \left(\frac{\varepsilon}{\varepsilon_0} \right)^{r-1/2} \tag{5.26}$$

where τ_0 is a reference relaxation time given at a specific temperature T_0 and energy ε_0 and where r and s are respectively the energy and the temperature dependence parameters. By correctly choosing the values of r and s, specific scattering mechanisms can be considered. The purpose is then to recalculate the transport properties considering one scattering mechanism at the time and finally to sum the two contributions. In the case of ionized impurity scattering, $\tau_{\text{II}} \sim \varepsilon^{3/2}$ corresponds to the values $s = 0$ and $r = 2$ in the BoltzTraP code. For acoustic phonon scattering, $\tau_{\text{AP}} \sim T^{-1} \varepsilon^{-1/2}$ sets the parameters to $s = -1$ and $r = 0$.

5.2 Experimental fitting

At this point, two types of procedure are possible to identify the dominant scattering mechanisms in $Ca_5Al_2Sb_6$ and Ca_3AlSb_3. Firstly, the relaxation time of each scattering mechanism could be theoretically computed (from equations (5.11) and (5.24) in the case of ionized impurity and acoustic phonon scattering) and then compared with others. Mechanisms with the smaller relaxation times would then be identified as dominant. This technique requires to consider every mechanism since it is their relative differences that allows the identification. A second possibility is to calculate the transport properties while considering relevant mechanisms (ionized impurity and acoustic phonon scattering in this case) and fit them as best as possible on experimental results by varying the value of their reference relaxation time τ_0. If these scattering mechanisms are sufficient to reproduce experimental results, they can thus be considered as dominant. If no match is possible between the results, other scattering mechanisms should be considered. This technique, less demanding in terms of theoretical calculations, was used in this work and is explained here below.

In the BoltzTraP implementation, parameters r and s are fixed according to the scattering mechanism and influence the energy and temperature dependence of τ. As said previously, the reference relaxation time τ_0 is kept variable in order to fit experimental results but ε_0 and T_0 must be fixed so that the results only have one degree of liberty and can therefore be compared. The energy ε_0 is fixed to 0.01 eV and the temperature T_0 is set to 600 K. Fitted results for electrical resistivities of doped $Ca_5Al_2Sb_6$ and Ca_3AlSb_3 are respectively shown in Figures 5.1 and 5.2. On those graphs, red curves correspond to the results obtained with the constant relaxation time considered in previous chapters. Green and blue curves are respectively related to the ionized impurity and acoustic phonon contributions to the electrical resistivity. The marked black curves correspond to the experimental results (taken from the same articles used in previous chapters) and the dashed black lines are the sum of the scattering contributions, i.e. the total resistivity of the analysed compound. The two correct scattering contributions are found by trial and error by varying the value of the reference relaxation time until the global resistivity can fit the experimental one. Ionized impurity and acoustic phonon scattering are therefore identified as dominant since they are sufficient to reproduce experimental results.

Although the relaxation time of ionized impurity scattering does not directly depend on the temperature, one can observe it is strongly decreasing with the temperature. It must therefore be due to its energy dependence, which comes from the variation of the Fermi level with the temperature and the doping level. This decrease is thus band structure dependent, i.e. unit cell dependent. The increase of the acoustic phonon contribution is due both to the temperature and energy dependences of its related relaxation time, i.e. it is also partially material dependent. These two mechanisms compensate above 650 K and lead to a constant electrical resistivity. This behaviour is quite unusual since the acoustic phonon contribution is strongly dominant over the ionized impurity contribution in most materials. For example, the relaxation time of

acoustic phonon scattering in PbTe is 60 times larger than the ionized impurity contribution at 300 K ($\tau_{AP} = 68{\cdot}10^{-14}$s and $\tau_{II} = 4{\cdot}10^{-11}$s) and increases to be 1400 times larger at 900 K (at $\varepsilon = 0.02$ eV) [36]. This dominant acoustic phonon contribution in PbTe and in many other materials leads to an important increase of the resistivity with the temperature. A constant relaxation time can therefore not be used to reproduce the electrical resistivity. The constant behaviour of the electrical resistivity in $Ca_5Al_2Sb_6$ and Ca_3AlSb_3, which enables the use of a constant relaxation time, is thus specific to these two phases, i.e. their electronic band structures, and due to the compensation of their scattering mechanisms. This validity of the constant relaxation time is therefore material dependent. Results for other doping levels can be found in Appendix C.

Now that the validity of the constant relaxation time approximation has been explained, the variation of the fitted relaxation times with the doping level can be analysed. These are presented in Table 5.1. Relaxation times of ionized impurity scattering decrease when the doping level increases, which is indeed in logical agreement with equation (5.11) stipulating that $\tau_{II} \sim N_i^{-1}$. As for acoustic phonon scattering, the relaxation time remains constant regardless the doping level for Ca_3AlSb_3, but a large doping difference in $Ca_5Al_2Sb_6$ between $2{\cdot}10^{20}$ and $7{\cdot}10^{19}$ cm^{-3} actually results in its decrease. Since the only term related to the doping level in equation (5.24) is the band effective mass, its variation with the doping level must be the reason of the variation of the relaxation time.

Finally, the relaxation time of each scattering mechanism in the two phases can be compared since they were computed for the same T_0 and ε_0. This comparison allows one to determine which scattering mechanism differs more between the two phases, i.e. which one is mainly responsible for their difference in electrical resistivities. For ionized impurity scattering, values should ideally be compared at the same doping level, which is not possible here due to lack of experimental data. However, relaxation times of this mechanism are in similar range. Since the main difference seems to reside in acoustic phonon scattering, it is relevant to perform a full theoretical computation of its related relaxation time. This analysis should allow to understand the origin of the difference between the electrical resistivities of two phases as well as the observed variation with the doping level in the case of $Ca_5Al_2Sb_6$.

Table 5.1: Fitted relaxation times of ionized impurity and acoustic phonon scattering mechanisms in $Ca_5Al_2Sb_6$ and Ca_3AlSb_3 at different doping levels.

Unit cell	Doping [cm^{-3}]	$\tau_{0,II}$ [fs]	$\tau_{0,AP}$ [fs]
$Ca_5Al_2Sb_6$	$5{\cdot}10^{20}$	0.50	80
	$2{\cdot}10^{20}$	0.60	80
	$7{\cdot}10^{19}$	1	40
Ca_3AlSb_3	$5{\cdot}10^{19}$	0.35	400
	$4{\cdot}10^{19}$	0.35	400
	$3{\cdot}10^{19}$	0.55	400

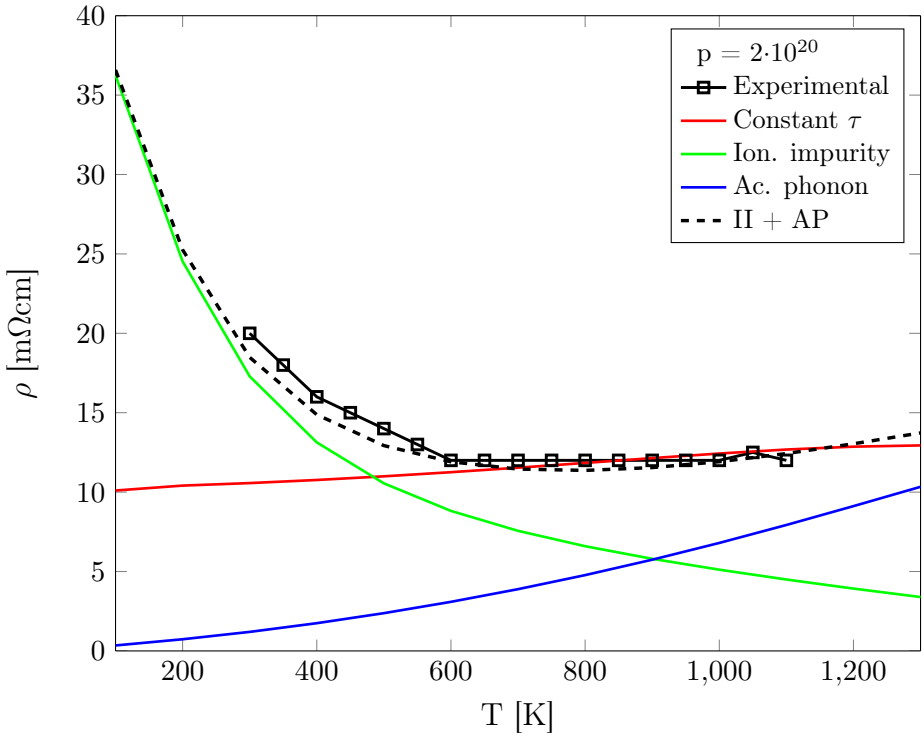

Figure 5.1: Experimental fitting of the electrical resistivity of $Ca_5Al_2Sb_6$ at a $2{\cdot}10^{20}$ cm^{-3} doping level based on ionized impurity and acoustic phonon scattering mechanisms.

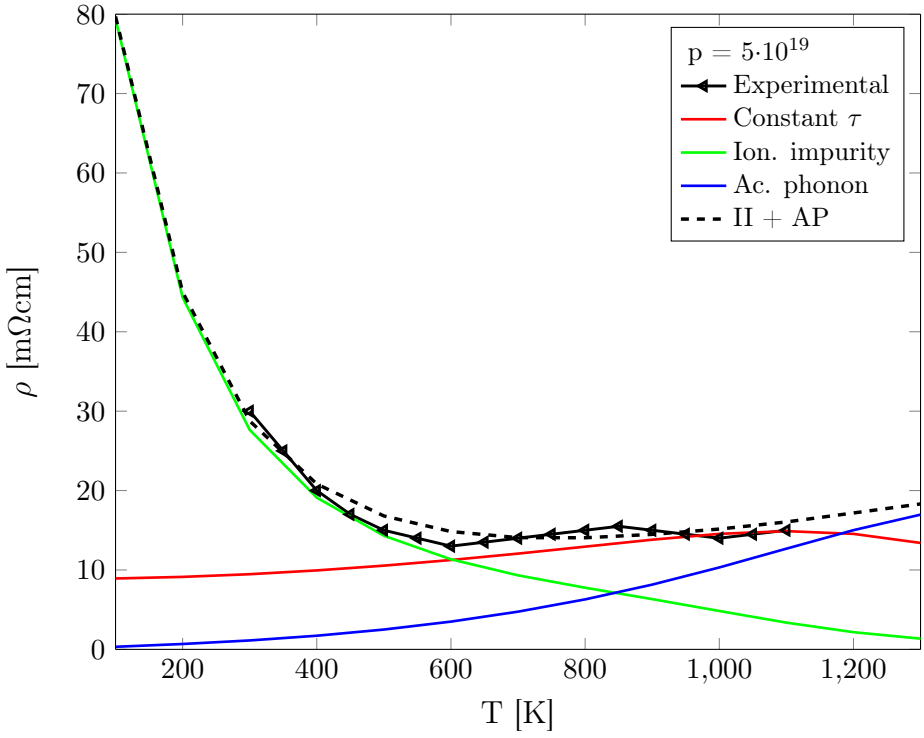

Figure 5.2: Experimental fitting of the electrical resistivity of Ca_3AlSb_3 at a $5{\cdot}10^{19}$ cm^{-3} doping level based on ionized impurity and acoustic phonon scattering mechanisms.

5.3 *Ab initio* study of acoustic phonon scattering

The experimental fitting revealed that the acoustic phonon scattering differs significantly from one compound to another. The purpose of this investigation is to understand the origin of this difference and to analyse the variation of the relaxation time with the doping level observed in $Ca_5Al_2Sb_6$. The previously found expression for the relaxation time of the acoustic phonon scattering is

$$\tau(\varepsilon) = \frac{2\pi\hbar^4 d v_0^2}{E_1^2 (2m^*_{\text{band}} k_B T)^{3/2}} \left(\frac{\varepsilon}{k_B T}\right)^{-1/2} \tag{5.27}$$

The reference relaxation τ_0 must computed at a specific temperature T_0 and energy ε_0 and then used in BoltzTraP. Its expression is

$$\tau_0 = \frac{2\pi\hbar^4 d v_0^2 \varepsilon_0^{-1/2}}{E_1^2 (2m^*_{\text{band}}(T_0))^{3/2} k_B T_0} \tag{5.28}$$

The deformation potential constant E_1 and the sound velocity v_0 must be computed through first-principle calculations. The evolution of the band effective mass with the temperature should also be analysed at different doping levels since it is most likely the term responsible for the variation with the doping level.

5.3.1 Deformation potential constant

The deformation potential method introduced by Bardeen and Shockley [37] is used to describe electron interactions with phonons, i.e. their scattering, using the following Hamiltonian:

$$\hat{H}'_{ac} = E_1 \nabla \cdot \mathbf{u}_{ac}(\mathbf{r}) \tag{5.29}$$

where E_1 is the deformation potential constant and $\mathbf{u}_{ac}(\mathbf{r})$ the shift vector. As explained previously, acoustic phonons are treated as atomic displacements in this method. These displacements lead to a deformation of the crystal, which gives rise to a shift of the electronic structure. The deformation potential constant E_1 used in this context characterizes this energy shift at the valence band edge. This first equation must be simplified in order to calculate the deformation potential constant from first-principle calculations. The following assumptions are based on explanations from Ref. [38].

The interaction Hamiltonian can been expressed as a small variation of energy δE due to acoustic phonons and the divergence of the shift vector can be reevaluated by considering the following tensor:

$$\frac{\partial u_i}{\partial x_j} = A_{ij} + S_{ij} \tag{5.30}$$

where A_{ij} and S_{ij} are respectively the antisymmetric and symmetric tensors. The first one corresponds to a rigid rotation of the crystal and does not lead to any energy shift. The symmetric tensor is more relevant in the present case as it describes the strain induced in the unit cell by the atomic displacement, i.e. by the acoustic phonons. By definition, the trace of this tensor is equal to the small volume change of the unit cell due to strain:

$$\mathrm{tr}(S_{ij}) = \frac{\delta V}{V_0} \tag{5.31}$$

where V_0 is the initial volume. It can be shown that this antisymmetric tensor is diagonal when longitudinal acoustic mode is considered. The divergence of the shift vector can therefore be expressed as

$$\nabla \cdot \mathbf{u}_{ac}(\mathbf{r}) = \frac{\delta V}{V_0} \tag{5.32}$$

The general expression for the interaction Hamiltonian can thus be reformulated as

$$\delta E = E_1 \frac{\delta V}{V_0} \tag{5.33}$$

The latter expression seems to be computable by first-principle calculations. However, although this technique works for a relative deformation potential (between two bands, e.g. the band gap), it can not be applied for the computation of an absolute deformation potential constant, i.e. when considering the shift of a single band. The main problem is that the absolute position of an energy level in an infinity periodic crystal is defined in terms of the average potential. Since this reference level will vary from an unstrained cell to a strained unit cell, band energies cannot be compared. Many researchers tried to overcome this problem with various assumptions but the results from all these techniques often contradict each other and the search for a rigorous method, i.e. for invariant reference, is still under debate. Nowadays, there are basically two main methods to compare energies while taking into account a reference level.

While computing the band structure of a unit cell using first-principle calculations, eigenvalues of energy are given in function of the average potential. A first logical possibility is to considered this average potential as a reference. As this potential varies for different unit cells, one must therefore find the potential shift between their average potentials in order to correctly compare their energy levels. As introduced by Van de Walle and Martin [39], this potential shift can be found by considering the interface of two different unit cells (A and B) in a superlattice. The superlattice must be large enough so that on one side there are enough unit cells A to reproduce the average potential of a bulk A and that on the other side there are enough unit cells B to reproduce the average potential of bulk B. The potential shift can then be calculated at the interface. Relevant energies can be calculated in isolate unit cells (to avoid confinement due to the superlattice) and then be correctly compared by taking into account the potential

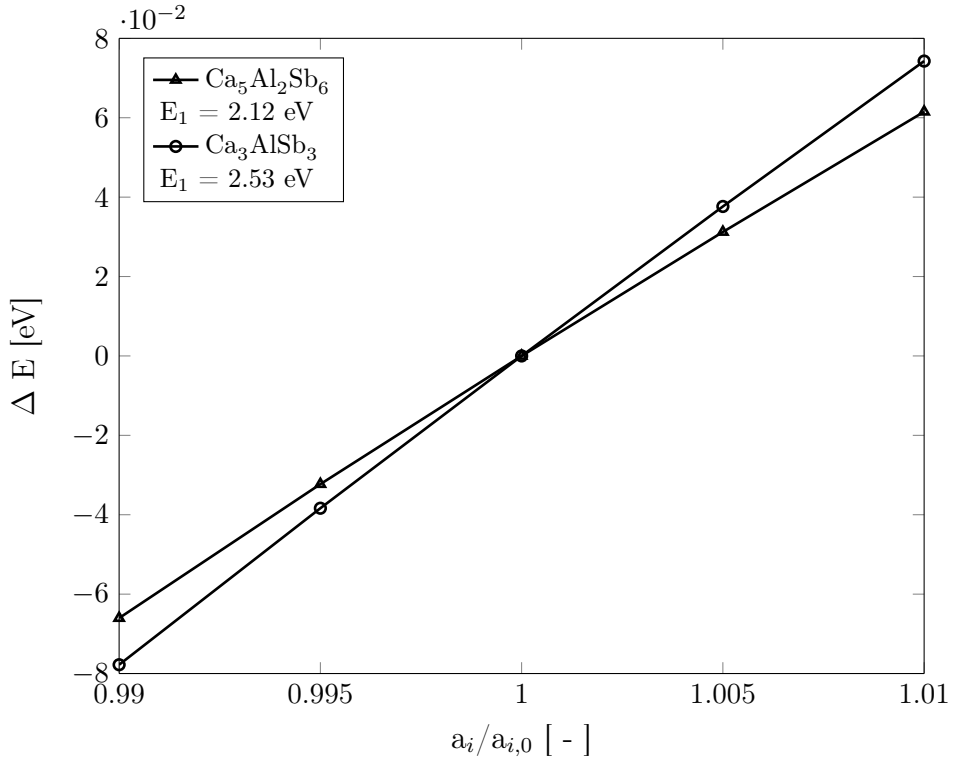

Figure 5.3: Energy variation of the valence band edge with the deformation of the lattice constants of both $Ca_5Al_2Sb_6$ and Ca_3AlSb_3 while considering a null potential shift.

shift. For the computation of a deformation potential, the two unit cells A and B are from the same material but deformed. Only one direction can be deformed at the time since two lattice constants must inevitably remain identical to correctly match at the interface. Van de Walle and Martin therefore divided the computation of the volume deformation potential constant into three uniaxial deformation potential constants by considering three different superlattices, one for each direction of deformation. This technique is very demanding in computational time, especially with such big cells as $Ca_5Al_2Sb_6$ and Ca_3AlSb_3, since all superlattices must be large enough for the average potentials to be converged. It was therefore not used in this thesis. Instead of that, a strong assumption was made that the potential shift is nearly equal to zero. The important similarity of the strained and unstrained unit cells (small deformations, no defect nor atomic substitution, etc.) motivated this assumption.

This first hypothesis leads to the results presented in Figure 5.3. The energy of the valence band edge (located at the Z point for $Ca_5Al_2Sb_6$ and at the Γ point for Ca_3AlSb_3) is computed for several deformed unit cells. The homogeneous deformations of the lattice constants a_i remain small and can be set to 0.99 $a_{i,0}$, 0.995 $a_{i,0}$, 1 $a_{i,0}$, 1.005 $a_{i,0}$ and 1.01 $a_{i,0}$. The deformation potential constant of the valence band edge can then be calculated considering the volume variation and the corresponding energy variation of the band. The linearity of this variation in the present results confirms that the chosen deformations were indeed small enough.

A second possibility to compute absolute deformation potential is to consider the energy of a core level as a reference energy, instead of the average potential. This option avoids the demanding computation of the potential shift. This assumption actually supposes that the core electron does not take part of any bonding, i.e. its energy is not influence by the environment. The difference between this energy level and the average potential should therefore remain constant. In practical terms, one must ideally have access to a pseudopotential including at least one core level. Only valence electrons are considered in FHI pseudopotentials used in this thesis but a visual analysis of the band structures revealed that some low valence bands actually disperse only a little, meaning that these electrons are strongly localized on an atom, i.e. do not take part to any bonding. Analysing the projected density of states also verified their localizations. Electronic band structures and densities of states of the relevant energy ranges are shown for $Ca_5Al_2Sb_6$ and Ca_3AlSb_3 in Figures 5.4 and 5.5. Firstly, the less dispersive state was considered as invariant and therefore taken as a reference. For both compounds, it corresponds to the state of highest energy in the represented states (around -8.5 eV). One can observe on density of states representations that it corresponds to some Sb–Al states. However, antimony atoms are strongly localized at this energy for both compounds. The antimony state ratios are indeed 0.96 for $Ca_5Al_2Sb_6$ and 0.9626 for Ca_3AlSb_3.

In addition to the use of less dispersive core states as references, one should also calculate deformation potential constants using the lowest energy states as references (around -10.5 eV), even if they disperse more, in order to get a range of value. Their relative state ratios are lower than for the previous consideration (0.9356 for $Ca_5Al_2Sb_6$ and 0.8451 for Ca_3AlSb_3) which means that they should be more influenced by their environment.

The results from these three assumptions are given in Table 5.2. The values for the less dispersive state reference are very similar to those obtained for a supposedly null potential shift. This similarity confirms that the potential shift is indeed very small. The larger values of the last approximation are due to the more important dispersion of the energy bands taken as reference and will therefore be used as an upper bound for the constants. They would therefore reflect the case where there is a small potential shift. One should finally note that deformation potential constants are all positive and are larger for Ca_3AlSb_3. For a same deformation, the shift of its valence band will then larger than for $Ca_5Al_2Sb_6$.

Table 5.2: Computed absolute deformation potential constants of the valence band edge of $Ca_5Al_2Sb_6$ and Ca_3AlSb_3 under different approximations: (A) the supposedly identical average potentials, (B) the less dispersive valence state and (C) the lowest valence state are taken as references.

Unit cell	$E_{1,A}$ [eV]	$E_{1,B}$ [eV]	$E_{1,C}$ [eV]
$Ca_5Al_2Sb_6$	2.12	2.02	3.82
Ca_3AlSb_3	2.53	2.75	4.99

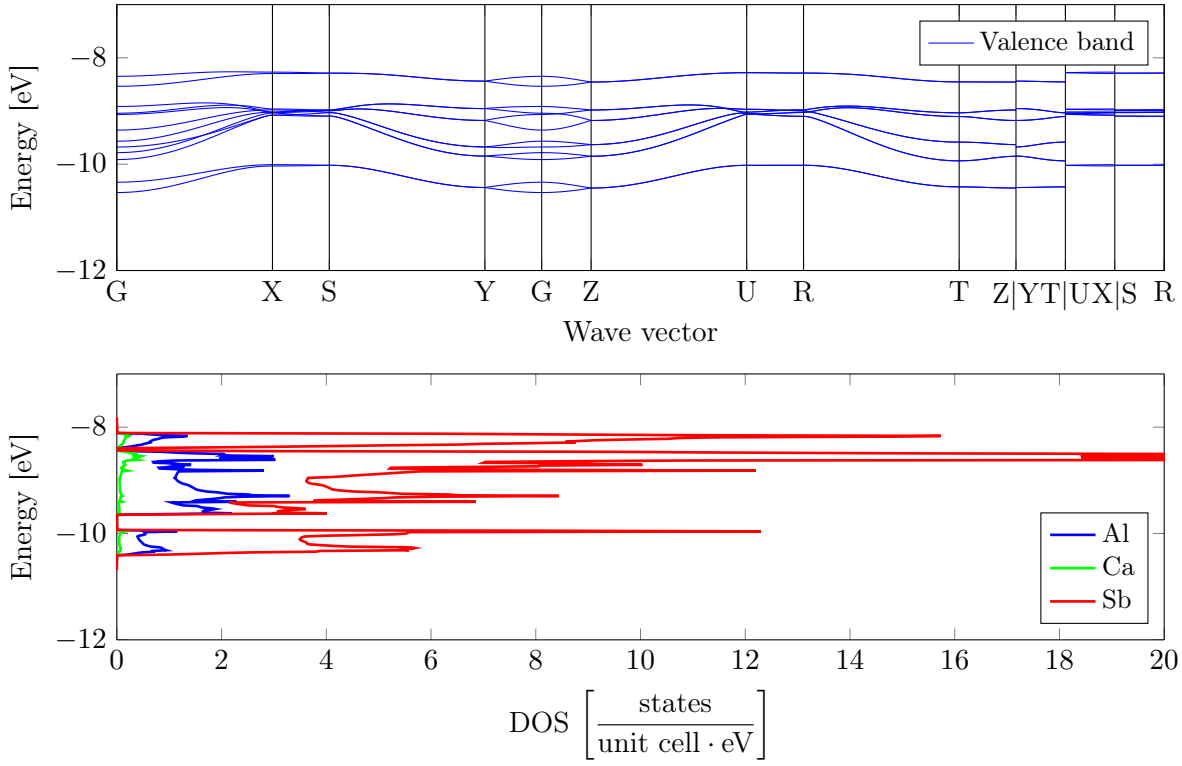

Figure 5.4: Electronic band structure and density of states of core electrons of $Ca_5Al_2Sb_6$.

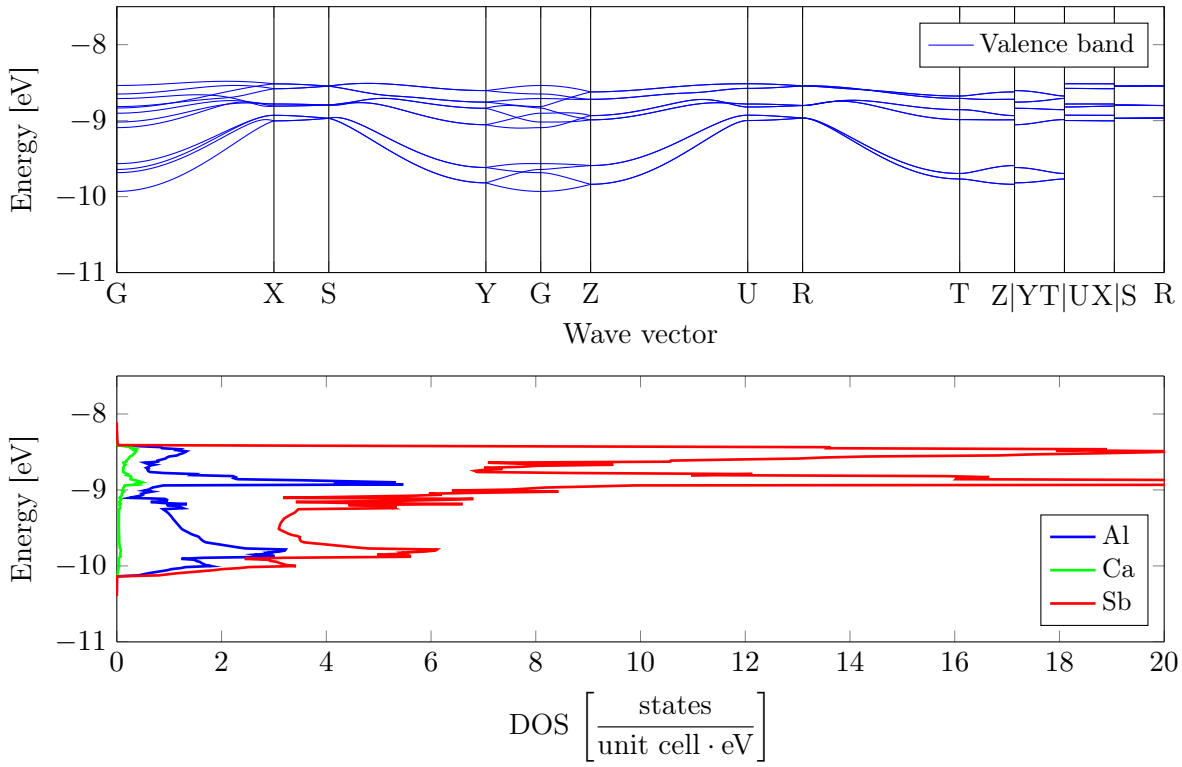

Figure 5.5: Electronic band structure and density of states of core electrons of Ca_3AlSb_3.

5.3.2 Sound velocity

As seen from equation (5.28), sound velocities must be computed in order to find the values of τ_0. Elastic constants of the two Zintl structures were calculated as they can express these velocities by using the Voigt-Reuss-Hill approximation [40, 41]. The orthorhombic symmetry reduces to 9 the number of independent constants. The variation of the total energy E of a system of volume V under a deformation ϵ and the elastic constants C can be expressed by

$$E(\epsilon) = E(0) + \left.\frac{\partial^2 E}{\partial \epsilon_i \epsilon_j}\right|_0 \epsilon_{ij}^2 \tag{5.34}$$

$$C_{ij} = \frac{1}{V}\left.\frac{\partial^2 E}{\partial \epsilon_i \epsilon_j}\right|_0 \tag{5.35}$$

These constants can be computed using the density functional perturbation theory in ABINIT to run strain response-function calculations. The first step is to make sure the structure is correctly relaxed. A ground-state density is then calculated from a self-consistent cycle and is the starting point for a non-self consistent run. The latter ensures that the wave functions are converged. The last step is to run a response-function calculation specific for a strain perturbation in order to get the elastic tensor. First-order wave functions for the strain perturbation are used to calculated the second derivatives of the total energy, required to calculate the elastic constant. The perturbation is characterized by its wavevector (`nqpt` and `qpt` in ABINIT) and its directions (`rfdir`). The variable `rfstrs` = 3 specifies that both uniaxial and shear strains must be computed.

The cut-off energy and the number of k-points were converged with a criteria of a 1 % difference with the asymptotic values of elastic constants (calculated for `ecut` = 60 Ha and `ngkpt` = 20×20×20). Results of these convergence studies for $Ca_5Al_2Sb_6$ are shown in Appendix D. The elastic constants are converged for `ecut` = 15 Ha and `ngkpt` = 10×10×10. The same convergent parameters were found for Ca_3AlSb_3.

The Voigt-Reuss-Hill approximation [40, 41] links the elastic constants to the bulk modulus B and the shear modulus G. Their lower (Reuss) and upper (Voigt) bounds are defined by

$$B_V = (1/9)[C_{11} + C_{22} + C_{33} + 2(C_{12} + C_{13} + C_{23})] \tag{5.36}$$

$$\begin{aligned} G_V = (1/15)[&C_{11} + C_{22} + C_{33} + 3(C_{44} + C_{55} + C_{66}) \\ &- (C_{12} + C_{13} + C_{23})] \end{aligned} \tag{5.37}$$

$$\begin{aligned} \Delta = C_{13}&(C_{12}C_{23} - C_{13}C_{22}) + C_{23}(C_{12} + C_{13} - C_{23}C_{11}) \\ &+ C_{33}(C_{11}C_{22} - C_{12}^2) \end{aligned} \tag{5.38}$$

$$\begin{aligned} B_R = \Delta[&C_{11}(C_{22}+C_{33}-2C_{23})+C_{22}(C_{33}-2C_{13})-2C_{33}C_{12} \\ &+C_{12}(2C_{23}-C_{12})+C_{13}(2C_{12}-C_{13})+C_{23}(2C_{13}-C_{23})]^{-1} \end{aligned} \tag{5.39}$$

$$\begin{aligned} G_R = 15\{4[&C_{11}(C_{22}+C_{33}+C_{23})+C_{22}(C_{33}+C_{13})+C_{33}C_{12} \\ &-C_{12}(C_{23}+C_{12})-C_{13}(C_{12}+C_{13})-C_{23}(C_{13}+C_{23})]/\Delta \\ &+3[(1/C_{44})+(1/C_{55})+(1/C_{66})]\}^{-1} \end{aligned} \tag{5.40}$$

The average bulk modulus B and shear modulus G can then be expressed from these bounds:

$$B = 1/2(B_V + B_R) \tag{5.41}$$

$$G = 1/2(G_V + G_R) \tag{5.42}$$

The transverse and longitudinal sound velocities can finally be computed and used to express the average sound velocity v_m using the following expressions:

$$v_t = \sqrt{\frac{B}{d}} \tag{5.43}$$

$$v_l = \sqrt{\left(B + \frac{3}{4}G\right)/d} \tag{5.44}$$

$$v_m^3 = \frac{3}{v_l^{-3} + 2v_t^{-3}} \tag{5.45}$$

The results from these equations are compared with the literature in Table 5.3. The values from Yang's article were computed using PAW in the GGA approximation and the experimental velocities of both Snyder's articles were obtained using room temperature ultrasonic measurements.

Table 5.3: Comparison of computed elastic properties of $Ca_5Al_2Sb_6$ and Ca_3AlSb_3 with the literature.

Unit cell	References	d [g/cm^3]	B [GPa]	G [GPa]	v_t [m/s]	v_l [m/s]
$Ca_5Al_2Sb_6$	Present work	–	43	29	2636	3919
	Yang *et al.* [27]	4.23	39	22.4	2300	4030
	Snyder *et al.* [3]	4.31	39	25	2400	4100
Ca_3AlSb_3	Present work	–	42	29	2678	3964
	Snyder *et al.* [42]	4.14	39	25	2440	4170

5.3.3 Band effective mass

Effective masses depend on the dispersion of the energy bands. The temperature and the doping level have thus an influence on these masses as they induce a variation of the Fermi level. Since the band effective mass m^*_{band} is used in the expression of the relaxation time (5.28), its variation with the temperature at different doping levels is studied using BoltzTraP. The results are illustrated in Figures 5.6 and 5.7 and should analysed with regard to the electronic band structures of $Ca_5Al_2Sb_6$ and Ca_3AlSb_3 (see Figures 3.1 and 4.1 on pages 24 and 36). The higher values of $Ca_5Al_2Sb_6$ are due to its flatter valence band edge and will inevitably lead to a difference in the final relaxation time. Then, when the doping level in a *p*-type semiconductor increases, the Fermi level is lowered in the valence band, so that the effective masses vary. The variation of the band mass with the doping level or the temperature is nevertheless not easy to analyse since it is a convolution of the three inertial effective masses. One can just note that the variation with the doping level is much more important in the case of $Ca_5Al_2Sb_6$ (the band mass decreases with it), which is the direct reason for the varying value of τ_0 with this doping level. In the case of Ca_3AlSb_3, the band mass is only slightly increasing with the doping level, which can explain the nearly constant relaxation time.

5.3.4 Relaxation time

Now that the deformation potential constants, the sound velocities and the band effective mass variations with the temperature and the doping level have been investigated, the relaxation time can be calculated using equation (5.28). The temperature T_0 and energy ε_0 used previously must be kept identical (600 K and 0.01 eV) in order to correctly compare experimental and computed values. The average sound velocities v_m are used here (2879 m/s for $Ca_5Al_2Sb_6$ and 2923 m/s for Ca_3AlSb_3). Relaxation times are computed using both the lower and upper deformation potential constants, respectively calculated using the less dispersive ($E_{1,B}$) and the lowest energy state ($E_{1,C}$) as references. These values are given in Table 5.4 and compared with the fitted values.

One can firstly note that computed values are within the same range as experimental values. Their values depend in particular on the deformation potential constant, which was here calculated with strong assumptions. Since experimental relaxation times lie in their corresponding computed relaxation times range, the correct deformation potential must itself lie between the lower and upper computed bounds. As this range is not that large ($\pm$ factor 3), this analysis could confirm that good approximated deformation potential constants can be obtained using the less dispersive or lowest energy state as a reference in the absolute calculation. However, the deformation potential constants are obviously not the only responsible for the value of the relaxation times, one should therefore still be careful when using these assumptions.

Secondly, one can observe that these computed values correctly follow the same trends with the doping level as the fitted ones. They are indeed increasing with the doping level for $Ca_5Al_2Sb_6$ and slightly decreasing – nearly constant for Ca_3AlSb_3. This behaviour was identified as the

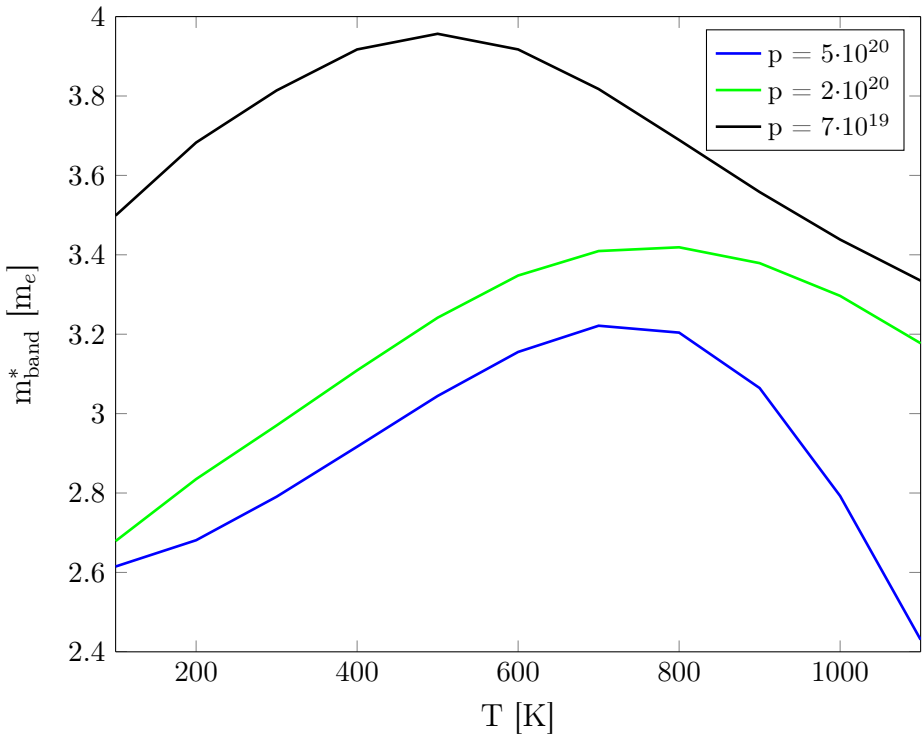

Figure 5.6: Evolution of the band effective mass of $Ca_5Al_2Sb_6$ at different doping levels.

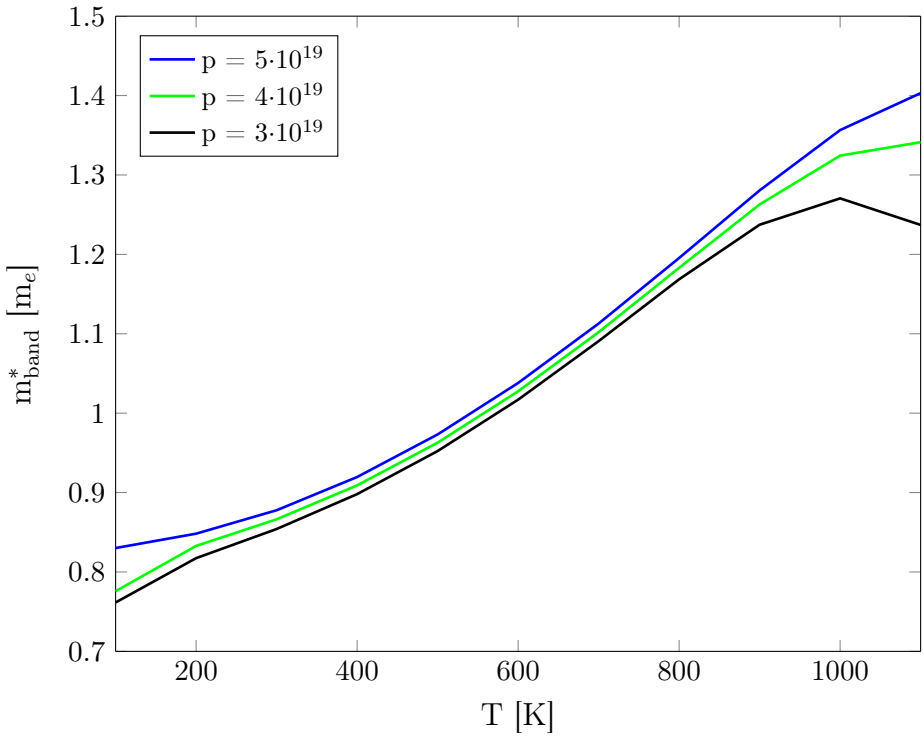

Figure 5.7: Evolution of the band effective mass of Ca_3AlSb_3 at different doping levels.

Table 5.4: Comparison of the fitted and the computed relaxation times of $Ca_5Al_2Sb_6$ and Ca_3AlSb_3 at different doping levels for acoustic phonon scattering mechanism in function of the different computed deformation potential constants.

Unit cell	Doping [cm^{-3}]	Fitted $\tau_{0,AP}$ [fs]	Computed $\tau_{0,AP}(E_{1,B})$ [fs]	Computed $\tau_{0,AP}(E_{1,C})$ [fs]
$Ca_5Al_2Sb_6$	$5{\cdot}10^{20}$	80	178	50
	$2{\cdot}10^{20}$	80	164	45
	$7{\cdot}10^{20}$	40	129	36
Ca_3AlSb_3	$5{\cdot}10^{19}$	400	527	160
	$4{\cdot}10^{19}$	400	535	162
	$3{\cdot}10^{19}$	400	544	165

direct consequence of the variation of the band effective mass with the doping level, as the relaxation is inversely proportional to this mass. For $Ca_5Al_2Sb_6$, it is experimentally observed that an increase of the doping level leads to a decrease of the resistivity (see Figure 3.11 on page 34), i.e. an increase of the relaxation time. Indeed when the doping level increases in $Ca_5Al_2Sb_6$, the band effective mass decreases and leads to an increase of the relaxation time, i.e. a decrease of the electrical resistivity. As for Ca_3AlSb_3, experimental results show an electrical resistivity nearly independent of the doping level at high temperature (see Figure 4.9 on page 42). It was indeed shown that the band effective mass is nearly constant with the doping level. A variation of the latter have thus nearly no influence on the electrical resistivity at high temperature.

5.4 Power factor

The power factor summarizes in one term both the Seebeck coefficient and the electrical resistivity ($PF = S^2\sigma = S^2/\rho$). This factor must simply be divided by the thermal conductivity in order to express the thermoelectric figure of merit. It varies with the doping level and the temperature as do its contributions. The electrical resistivity used here is considering both ionized impurity and acoustic phonon scattering mechanisms. Since the Seebeck coefficients still do not completely match with the experimental Seebeck values even after including the energy dependency of the relaxation, they were shifted while computing the power factor in order to avoid the propagation of their error.

One can observe that for $Ca_5Al_2Sb_6$ under 500 K, power factors are similar no matter the doping level. It means that in this range the decrease of the resistivity with the doping level is counterbalanced by the decrease of the squared Seebeck coefficient. At higher temperature, the power factor strongly increases with the doping level due to the important decrease of the electrical resistivity with it (factor 10 between $5{\cdot}10^{20}$ and $7{\cdot}10^{19}$ cm^{-3} doping levels). As for Ca_3AlSb_3, the power factor remains nearly constant with the doping level increases, in accordance with the fact that the relaxation time is nearly constant with it.

5.5 Conclusion

The first step in this chapter was to identify the main electron scattering mechanisms in $Ca_5Al_2Sb_6$ and Ca_3AlSb_3, in order to understand the observed constant resistivity. The relaxation time expression implemented in BoltzTraP allowed to compute separately the contribution of each scattering mechanisms. Since the calculated transport properties correctly fitted experimental results while considering both ionized impurity and acoustic phonon scattering, these two mechanisms were considered as dominant. Unlike many other materials, the acoustic phonon contribution is not dominant over the ionized impurity contribution. These mechanisms indeed compensate above 650 K and thus lead to the constant resistivity. For the two phases, this unusual constant resistivity can therefore be reproduced using a constant relaxation time since there is no temperature dependence.

In addition to this explanation of the validity of the constant approximation, this experimental fitting also revealed that the acoustic phonon scattering differs the most between the two compounds and that its related relaxation time varies differently with the doping level in the two phases. It was then decided to theoretically investigate this mechanism in order to understand the origin of these differences. The deformation potential constants, the sound velocities and the evolution of the band effective mass were computed and analysed. The good agreement of the computed values with the fitted ones suggests that the assumptions related to the computation of the deformation potential constants (the less dispersive state and the lowest in energy taken as references) were valid. The difference between the relaxation times of both compounds likely comes the convolution of these three parameters, since none of them show a significant difference. The different observed experimental trends in both compounds, i.e. the variation of the relaxation time with the doping level, are correctly recreated and justified by the different variations of the band effective mass of both compounds.

The final purpose of this study on electronic transport properties would be to fully reproduce or even anticipate experimental studies, without any experimental fitting. There is therefore a need to theoretically compute the relaxation time related to the ionized impurity scattering mechanism. It would then be possible to study the transport properties at any doping level or temperature. One must of course ensure first that these two mechanisms are indeed dominant electron scattering mechanisms in the material under study before computing the transport properties.

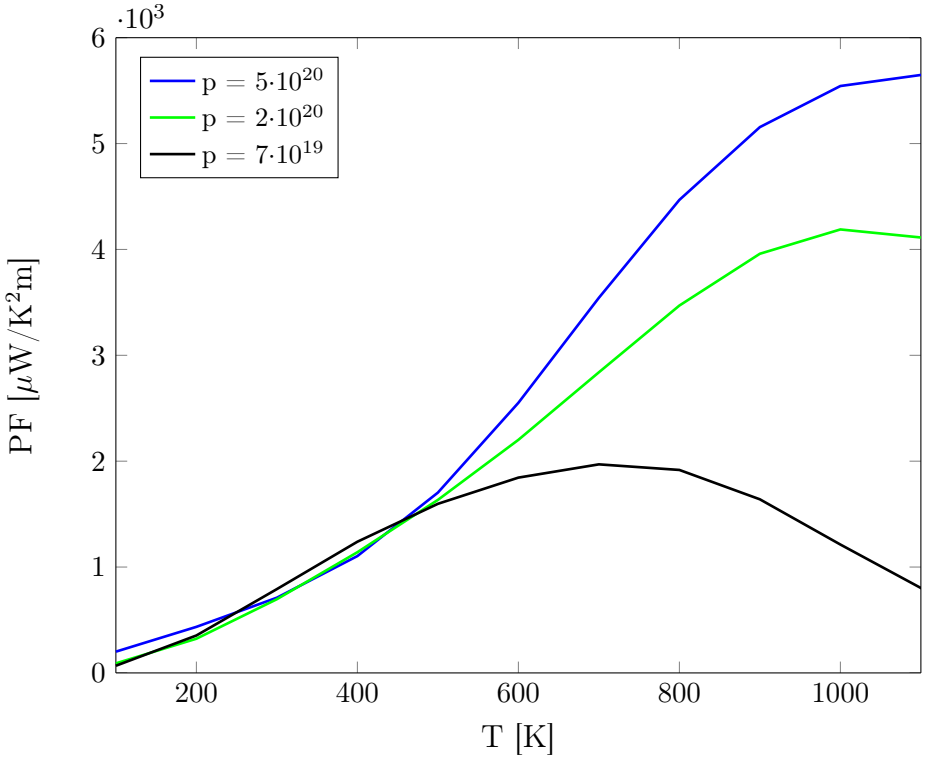

Figure 5.8: Evolution of the power factor of $Ca_5Al_2Sb_6$ with the temperature at different doping levels.

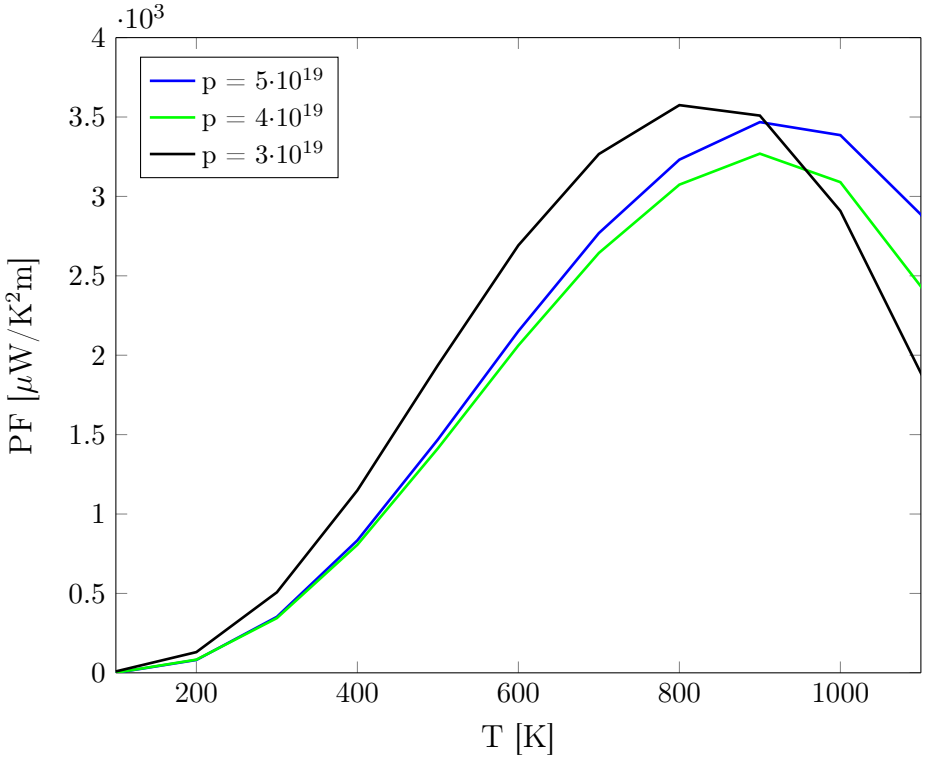

Figure 5.9: Evolution of the power factor of Ca_3AlSb_3 with the temperature at different doping levels.

Chapter 6

Anisotropic transport properties in $Ca_5Al_2Sb_6$

Contents

In addition to the previous study, it is also interesting to reach the final step of computing a figure of merit. This chapter is therefore devoted to the calculation of the different contributions to the latter factor for the $Ca_5Al_2Sb_6$ Zintl compound. The electronic contribution to the thermal conductivity is computed using the Wiedemann-Franz law with experimental Lorentz constants and the minimal lattice contribution is calculated from the elastic constants using Cahill's model.

The choice to study $Ca_5Al_2Sb_6$ over Ca_3AlSb_3 was actually motivated by the effective masses computed in Chapter 3 (see Table 3.3 on page 30). First of all, the effective mass in the X direction, i.e. along the covalent ladders, is especially light and should therefore lead to a very low resistivity. Secondly, despite this light effective mass, the band effective mass of $Ca_5Al_2Sb_6$ is heavier than the one of Ca_3AlSb_3 (respectively 2.63 m_e and 1.31 m_e) which is favorable to a high Seebeck coefficient. These two contributions made the X direction of $Ca_5Al_2Sb_6$ an interesting candidate to reach a high figure of merit.

Even if left aside in this chapter, the directional electrical resistivities, Seebeck coefficients and power factors of Ca_3AlSb_3 are shown in Appendix E. As expected from the isotropy of its effective masses (see Table 4.3 on page 38), transport properties show no anisotropy.

6.1 Power factor

The calculations of the electrical resistivity are considering the two electron scattering mechanisms studied previously. The anisotropy revealed in the effective masses computed at the ground state is clearly marked in the electrical resistivity, as it can be observed in Figure 6.1. At 600 K, the average resistivity is 30 mΩcm while in the X direction, it reaches 10 mΩcm.

The Seebeck coefficient is also anisotropic as shown in Figure 6.2 and is logically lower in the X direction since the effective mass is lighter. The average value is then 231 μV/K at 600 K while in the X direction, the Seebeck coefficient is 223 μV/K.

The anisotropy of the power factor is finally illustrated in Figure 6.3 and show an impressive and logical anisotropy with excellent values in the X direction (more than twice the average value). At 600 K, the average value is 1845 μW/K^{2}m while in the X direction, the power factor reaches 4695 μW/K^{2}m.

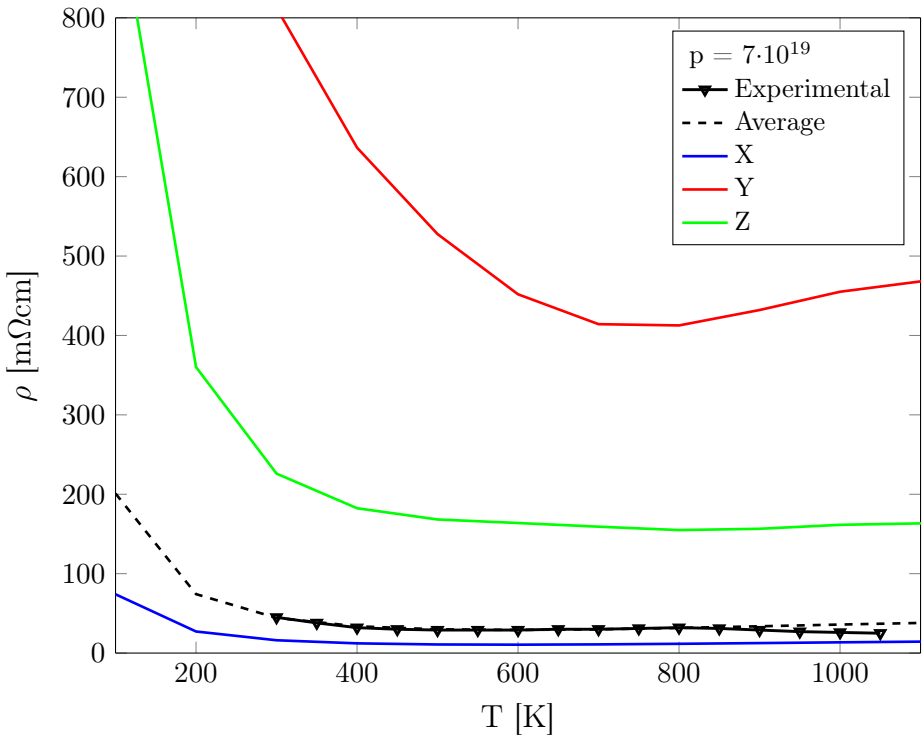

Figure 6.1: Anisotropy in the electrical resistivity of $Ca_5Al_2Sb_6$ based on ionized impurity and acoustic phonon scattering mechanisms.

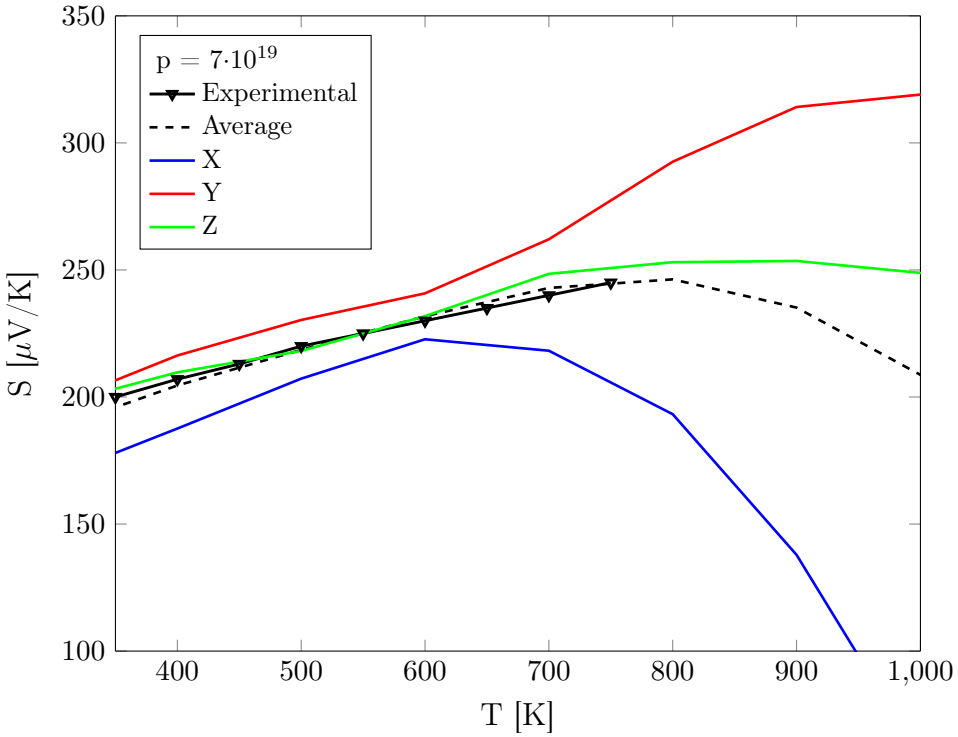

Figure 6.2: Anisotropy of the Seebeck coefficient of $Ca_5Al_2Sb_6$.

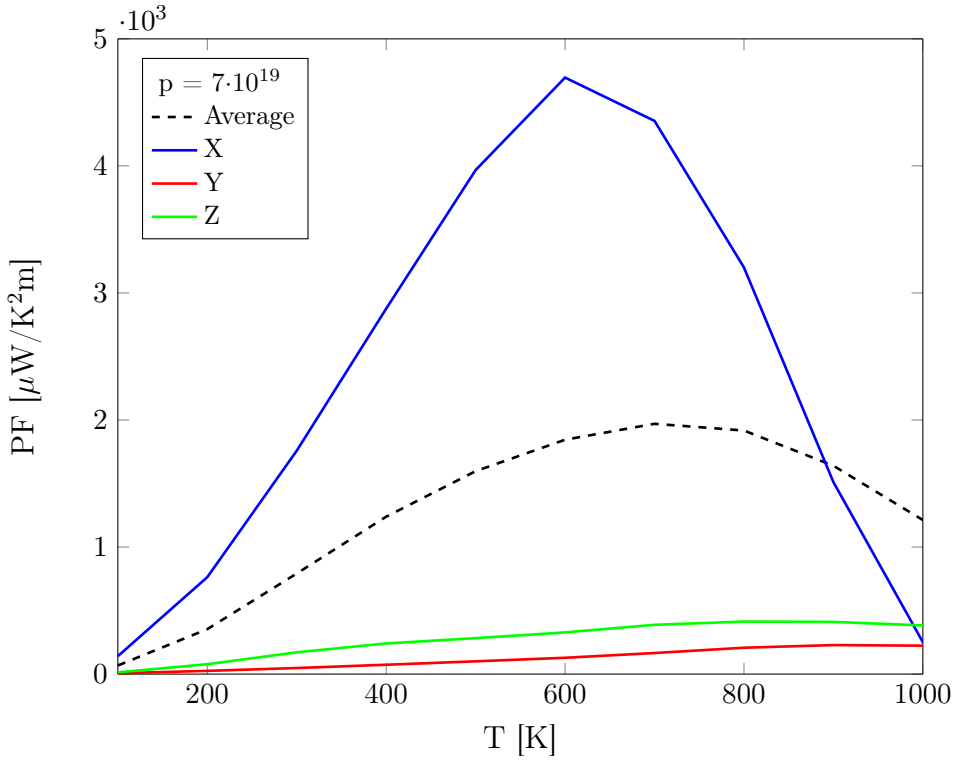

Figure 6.3: Anisotropy of the power factor of $Ca_5Al_2Sb_6$.

6.2 Thermal conductivity

6.2.1 Electronic contribution

The thermal conductivity, even if globally left aside in this thesis, is as important as the electrical conductivity for thermoelectric properties. It is divided in two contributions: the electronic and the lattice thermal conductivity. As explained in Subsection 1.3, it is actually possible to estimate the electronic contribution using the Wiedemann-Franz law:

$$\kappa_e = \frac{L_0 T}{\rho} \tag{6.1}$$

where L_0 is the Lorentz constant. Experimental Lorentz numbers were taken from Ref. [43]. Figure 6.4 shows both the Lorentz constants and the electronic thermal conductivity. A higher electrical conductivity logically leads to a higher electronic thermal conductivity, which will lower the figure of merit. However these values remain low: the average value at 600 K is 0.035 W/mK while it reaches 0.096 W/mK in the X direction.

6.2.2 Lattice contribution

The lattice thermal conductivity is much harder to compute since it requires to study the phonons in the unit cell. However, a simplified calculation is still possible. When the temperature is higher than the Debye temperature, the lattice thermal conductivity decrease with a $1/T$ dependence as the phonon transport is mainly limited by the Umklapp scattering. Using Anderson's formula [44], this Debye temperature can be expressed as

$$\Theta_D = \frac{v_m \hbar}{k_B} \left(\frac{6\pi^2 Q_n N_A d}{M} \right)^{1/3} \tag{6.2}$$

where Q_n is the number of atoms in the unit cell, N_A is the Avogadro's number and M is the molecular mass. A Debye temperature of 275 K is calculated, in quite correct agreement with the literature (286 K and 257 K in Refs. [4,42]). Above this temperature, the lattice contribution decreases and finally converges (above 850 K according to experimental results) to a minimal lattice contribution – the glassy minimum. This latter can be used to approximate to global lattice conductivity at high temperature. It can be calculated using the method of Cahill [45]:

$$\kappa_{l,min} = \frac{1}{2} \left(\frac{\pi}{6} \right)^{1/3} k_B \left(\frac{M}{Q_n N_A d} \right)^{-2/3} (2v_t + v_l) \tag{6.3}$$

The calulated minimal lattice thermal conductivity is 0.534 W/m.K, also in correct agreement with the literature (0.53 W/m.K and 0.52 W/m.K in Refs. [4, 27]). This glassy minimum is not reached in every material, but the structural complexity of $Ca_5Al_2Sb_6$ confines the heat

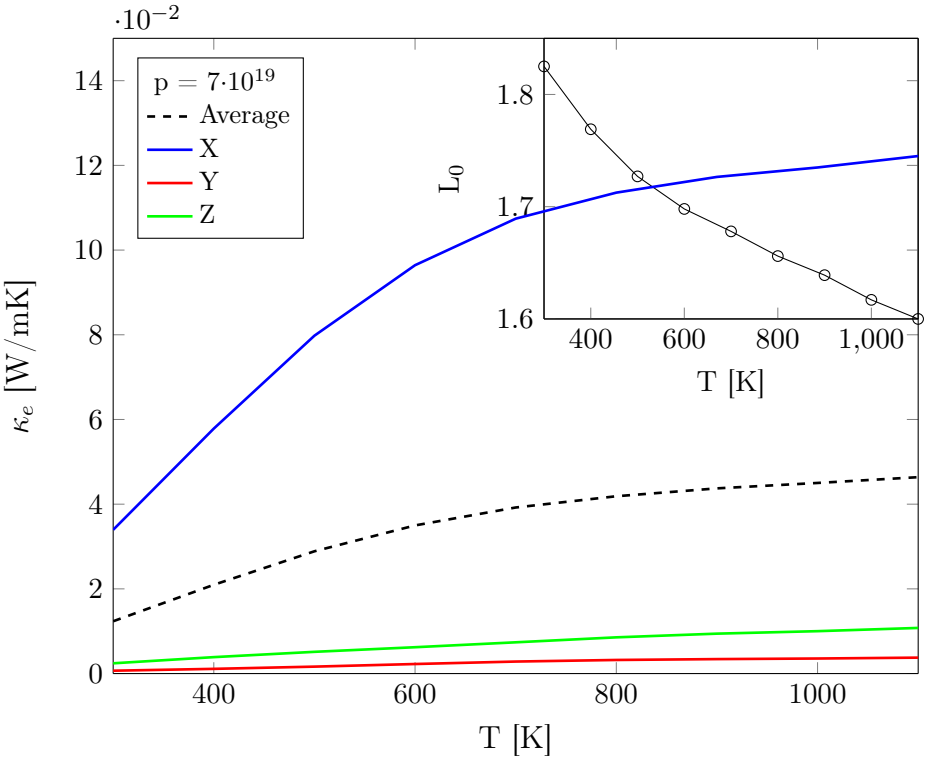

Figure 6.4: Anisotropy of the electronic thermal conductivity of $Ca_5Al_2Sb_6$.

in low velocity optical phonon modes and creates additional scattering channels for Umklapp processes [4]. This value is thus reached in experimental results at high temperature no matter the doping level. To reduce this minimal value, one must modify the unit cell, i.e. its elastic constants, in order to reach lower sound velocities. The anisotropy of this contribution can also be studied by considering anisotropic sound velocities through the following expressions [46]:

In the X direction:

$$[100] : v_l = \sqrt{C_{11}/d}, \quad [010] : v_{t1} = \sqrt{C_{66}/d}, \quad [001] : v_{t2} = \sqrt{C_{55}/d} \tag{6.4}$$

In the Y direction:

$$[010] : v_l = \sqrt{C_{22}/d}, \quad [100] : v_{t1} = \sqrt{C_{66}/d}, \quad [001] : v_{t2} = \sqrt{C_{44}/d} \tag{6.5}$$

In the Z direction:

$$[001] : v_l = \sqrt{C_{33}/d}, \quad [100] : v_{t1} = \sqrt{C_{55}/d}, \quad [010] : v_{t2} = \sqrt{C_{44}/d} \tag{6.6}$$

The values computed from these sound velocities show no anisotropy ($\kappa_{l,X} = 0.564$ W/mK, $\kappa_{l,Y} = 0.562$ W/mK, $\kappa_{l,Z} = 0.575$ W/mK) so that this contribution is considered isotropic. The sound velocities are calculated under different approximations than Voigt-Reuss-Hill so that the directional lattice contributions computed here above lead to a different average value than the one computed previously. However, the only interest was here to compare the directional values so that this difference is not important.

6.3 Figure of merit

The anisotropic electronic thermal conductivity is used in the calculation of the figure of merit while a constant value (0.7 W/mK) of is used for the lattice contribution. As observed in Figure 6.5, the average figure of merit is maximal at 800 K and reaches 0.23 for the $7{\cdot}10^{19}$ cm^{-3} doping level. The maximal figure of merit in the X direction is 0.41 and is reached at 700 K. This directional value (twice the average) is therefore very promising if the transport could be controlled along this direction. As it can be seen in Figure 6.6, since the electrical resistivity decreases with the doping level, the figure of merit increases with the doping level. However, at a certain doping level, the electronic contribution to the thermal conductivity is so high and the Seebeck coefficient so low that the final figure of merit will decrease (see Figure 1.4 on page 9).

In the line of this work, it would be interesting to find the optimal doping level for the figure of merit for both bulk $Ca_5Al_2Sb_6$ and in the X direction. This task is quite demanding if one has to consider both scattering mechanisms varying at each doping level. However several assumptions can simplify this process. One can indeed consider that relaxation times of ionized impurity scattering will only vary with $1/N_i$ and that the variation of the relaxation times of acoustic phonon scattering with the scattering can be expected from the variation of the band mass.

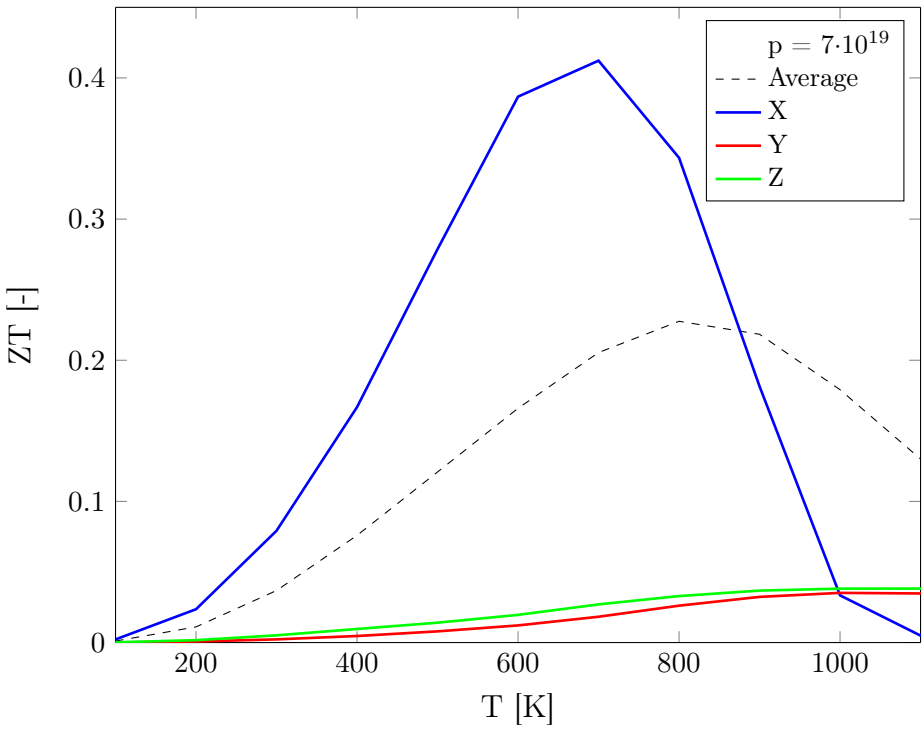

Figure 6.5: Anisotropy of the figure of merit of $Ca_5Al_2Sb_6$.

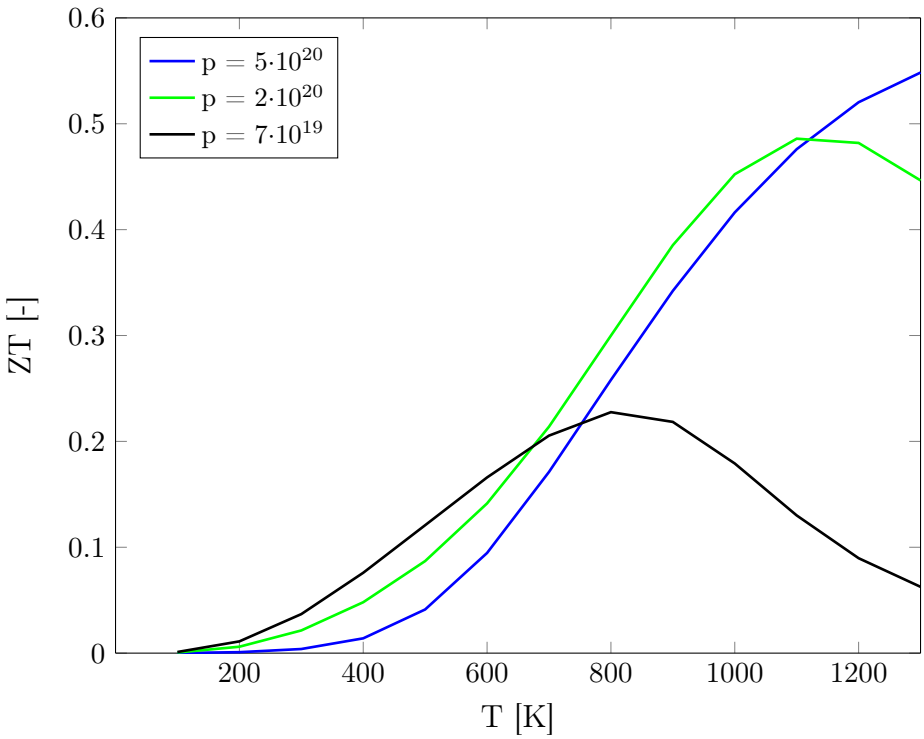

Figure 6.6: Figure of merit of $Ca_5Al_2Sb_6$ at different doping levels.

Conclusion and outlook

In recent experimental studies, both $Ca_5Al_2Sb_6$ and Ca_3AlSb_3 Zintl compounds exhibited interesting thermoelectric properties. The electrical resistivities of these *p*-type semiconductors are constant with the temperature and show different behaviours with the doping level. The purpose of this thesis was therefore to investigate these resistivities and understand the origin of their differences, since they have a direct impact on the figure of merit. This study was divided into three main parts.

First of all, general *ab initio* studies were performed for both compounds using ABINIT. Zintl structures are characterized by an inner anionic substructure, made of $AlSb_4$ tetrahedra in this present case. Unlike for Ca_3AlSb_3, neighbouring substructures in $Ca_5Al_2Sb_6$ are bonded through Sb atoms. The bonding character of these substructures were characterized using electron density difference maps and confirm their covalent character. This latter is responsible for the complexity of the crystal, i.e. its low lattice thermal conductivity. After a full structural relaxation, the electronic band structure and the projected density of states were computed for both compounds. Using the electronic structure as an input, the electronic transport properties (Seebeck coefficient and electrical resistivity) were computed using BOLTZTRAP in the constant relaxation time approximation. This approximation gave correct results at high temperature for both compounds since their electrical resistivities are constant with the temperature. The constant relaxation time used for $Ca_5Al_2Sb_6$ (10^{-14}s) is smaller than the one for Ca_3AlSb_3 ($4{\cdot}10^{-14}$s) so that the electrical resistivity of the latter is smaller for a same doping level. The resistivity of $Ca_5Al_2Sb_6$ decreases with the doping level while the one of Ca_3AlSb_3 remains constant.

In a second time, electron scattering mechanisms were studied in order to understand this constant behaviour of the resistivities with the temperature and their different variation with the doping level. Ionized impurity and acoustic phonon scattering were identified as dominant through an experimental fitting. The acoustic phonon contribution remains small compared to ionized impurity even at high temperature, unlike many other materials. These mechanisms therefore compensate above 650 K and lead to the constant resistivity. Since the acoustic phonon relaxation time differs the most between the two compounds and shows different behaviour with the doping level, an theoretical investigation of this mechanism was done. Deformation potential constants, characterizing the energy shift of the valence band with the deformation of the crystal due to acoustic phonon, were calculated under different approximation. It revealed that the

electronic structure of Ca_3AlSb_3 ($E_1 = \pm 2.53$ eV) is more sensitive to the deformations than the one of $Ca_5Al_2Sb_6$ ($E_1 = \pm 2.02$ eV). Strain response-function calculations allowed to compute the elastic constants used to express the sound velocities of both $Ca_5Al_2Sb_6$ and Ca_3AlSb_3 (respectively 2879 m/s and 2923 m/s). The band effective mass showed an important variation with the doping level for $Ca_5Al_2Sb_6$ while it remains constant for Ca_3AlSb_3. It explains the constant behaviour of the electrical resistivity of Ca_3AlSb_3 with the doping level. Since none of them showed a dominant difference, all these three parameters are responsible for the different acoustic phonon relaxation times of the two compounds. The computed relaxation times were in the same range as the fitted ones.

To continue this study on electron scattering mechanisms in Zintl compounds, it would be very interesting to compute the relaxation time related to the scattering by ionized impurity. It requires in particular the calculation of the dielectric constant of the unit cell. The combination of this mechanism with the acoustic phonon scattering would enable to compute the total electrical resistivity at any doping level and temperature. Experimental results could then be fully recreated or even anticipated, provided that these two mechanisms are indeed dominant in the material under study.

In the last part of this work, the anisotropy of $Ca_5Al_2Sb_6$ was studied. The effective mass in the direction of the covalent ladders is indeed much lighter than in the other directions while the band effective mass is still high enough to reach a high Seebeck coefficient. The electronic contribution to the thermal conductivity was calculated using experimental Lorentz constants and showed a logical anisotropy since it is inversely proportional to the electrical resistivity. A minimal lattice contribution of 0.53 W/m.K was calculated from Cahill's model and showed no isotropy. This contribution was then approximated by a constant value when computing the figure of merit. This latter also reflected this anisotropy. At a $7{\cdot}10^{19}$ cm^{-3} doping level, the figure of merit in the direction of the covalent ladders is 0.41 while the average is only 0.23. This isolation of the transport in this direction could therefore be an interesting possibility to reach a high figure of merit.

In the line of this anisotropic study, it would be interesting to find the optimal doping level for the figure of merit for both bulk $Ca_5Al_2Sb_6$ and in the direction along the covalent substructures. This task requires to take into account the two scattering and therefore to compute the relaxation time related to the scattering by ionized impurity, as suggest here above.

References

[1] I. Johnson, W. Choate, and A. Davidson. Waste heat recovery. Technology and opportunities in US industry. *BCS, Inc., Laurel, MD (United States)*, 2008.

[2] T. Tritt and M.A. Subramanian. Thermoelectric materials, phenomena, and applications: a bird's eye view. *MRS bulletin*, 31(03):188–198, 2006.

[3] A. Zevalkink, E. Toberer, W. Zeier, E. Flage-Larsen, and J. Snyder. Ca_3AlSb_3: an inexpensive, non-toxic thermoelectric material for waste heat recovery. *Energy & Environmental Science*, 4(2):510–518, 2011.

[4] A. Zevalkink, E. Toberer, N. Crisosto, and J. Snyder. The Zintl compound $Ca_5Al_2Sb_6$ for low-cost thermoelectric power generation. *Advanced Functional Materials*, 20(24):4375–4380, 2010.

[5] International Energy Agency. Key world energy statistics 2015. `https://www.iea.org/publications/freepublications/publication/key-world-energy-statistics-2015.html`, accessed June 19, 2016.

[6] BMW Group and A. Eder. Efficient and dynamic : The BMW group roadmap for the application of thermoelectric generators. `http://energy.gov/sites/prod/files/2014/03/f13/eder_0.pdf`, accessed April 15, 2015.

[7] J.-M. Fournier, C. Salvi, and J. Stochkolm. Thermoélectricité: Le renouveau grâce aux nanotechnologies. *Techniques Ingénieur*, 2006.

[8] L. Piraux and J.-C. Charlier. MAPR 2471 : Phénomènes de transport dans les solides et les microstructures (cours). *Université Catholique de Louvain*, 2015.

[9] Wikipedia, The Free Encyclopedia. Thermoelectric effect. `https://en.wikipedia.org/wiki/Thermoelectric_effect`, accessed May 1, 2015.

[10] M. Dresselhaus *et al.* New directions for low-dimensional thermoelectric materials. *Advanced Materials*, 19(8):1043–1053, 2007.

[11] C. Godart, E. Alleno, S. Volz *et al.* Nanomatériaux thermoélectriques. *Les nanomatériaux et leurs applications pour l'énergie électrique*, pages 262–385, 2014.

[12] Wikipedia, The Free Encyclopedia. Thermoelectric materials. `https://en.wikipedia.org/wiki/Thermoelectric_materials`, accessed May 21, 2016.

[13] J. Snyder and E. Toberer. Complex thermoelectric materials. *Nature materials*, 7(2):105–114, 2008.

[14] S. Kauzlarich, S. Brown, and J. Snyder. Zintl phases for thermoelectric devices. *Dalton Transactions*, (21):2099–2107, 2007.

[15] A. Zevalkink. PhD thesis : Chain-forming Zintl antimonides as novel thermoelectric materials. *California Institute of Technology*, 2014.

[16] Institut de Chimie Moléculaire et des Matériaux d'Orsay. Oxydes à propriétés remarquables - Thermoélectricité. `http://www.icmmo.u-psud.fr/Labos/SP2M/ThemeOxydes/ThemeOxydes_Thermoelectricite.php`, accessed April 19, 2015.

[17] J.-C. Charlier, X. Gonze, and G.-M. Rignanese. MAPR 2451 : Atomistic and nanoscopic simulations. *Université Catholique de Louvain*, 2015.

[18] Wikipedia, The Free Encyclopedia. Théorie de la fonctionnelle de la densité. `http://fr.wikipedia.org/wiki/Théorie_de_la_fonctionnelle_de_la_densité`, accessed April 2, 2015.

[19] B. Askerov. Electron transport phenomena in semiconductors. *World Scientific*, 1994.

[20] M. Kaviany. Heat transfer physics. *Cambridge University Press*, 2014.

[21] C. Hamaguchi. Basic semiconductor physics. *Springer Science & Business Media*, 2009.

[22] X. Gonze, G.-M. Rignanese *et al.* First-principles computation of material properties: The ABINIT software project. *Computational Materials Science*, 25(3):478–492, 2002.

[23] G. Madsen and D. Singh. BOLTZTRAP: A code for calculating band-structure dependent quantities. *Computer Physics Communications*, 175(1):67–71, 2006.

[24] P. Hohenberg and W. Kohn. Inhomogeneous electron gas. *Physical review*, 136(3B):B864, 1964.

[25] M. Fuchs and M. Scheffler. Ab initio pseudopotentials for electronic structure calculations of poly-atomic systems using density-functional theory. *Computer Physics Communications*, 119(1):67–98, 1999.

[26] A. Zevalkink, J. Snyder *et al.* Influence of the triel elements (M= Al, Ga, In) on the transport properties of $Ca_5M_2Sb_6$ Zintl compounds. *Chemistry of Materials*, 24(11):2091–2098, 2012.

[27] G. Yang, H. Cui, D. Ma, and C. He. The elastic and thermoelectric properties of the Zintl compound $Ca_5Al_2Sb_6$ under high pressure. *Journal of Applied Physics*, 116(22):223709, 2014.

[28] K. Momma and F. Izumi. Vesta: a three-dimensional visualization system for electronic and structural analysis. *Journal of Applied Crystallography*, 41(3):653–658, 2008.

[29] Y. L. Yan and Y. X. Wang. Crystal structure, electronic structure, and thermoelectric properties of $Ca_5Al_2Sb_6$. *Journal of Materials Chemistry*, 21(33):12497–12502, 2011.

[30] A. Jain, S. Ong, G. Hautier *et al.* The Materials Project: A materials genome approach to accelerating materials innovation. *APL Materials*, 1(1):011002, 2013.

[31] W. Setyawan and S. Curtarolo. High-throughput electronic band structure calculations: Challenges and tools. *Computational Materials Science*, 49(2):299–312, 2010.

[32] E. Toberer, A. May, B. Melot, E. Flage-Larsen, and J. Snyder. Electronic structure and transport in thermoelectric compounds AZn_2Sb_2 (A= Sr, Ca, Yb, Eu). *Dalton Transactions*, 39(4):1046–1054, 2010.

[33] Y. Pei, A. LaLonde, H. Wang, and J. Snyder. Low effective mass leading to high thermoelectric performance. *Energy & Environmental Science*, 5(7):7963–7969, 2012.

[34] A. Zevalkink, J. Snyder *et al.* Improved carrier concentration control in Zn-doped $Ca_5Al_2Sb_6$. *Journal of applied physics*, 110(1):013721, 2011.

[35] Q. Shi, Z. Feng, Y. Yan, and Y. X. Wang. Electronic structure and thermoelectric properties of Zintl compounds A_3AlSb_3 (A = Ca and Sr): first-principles study. *RSC Adv.*, 5:65133–65138, 2015.

[36] S. Ahmad and S. Mahanti. Energy and temperature dependence of relaxation time and Wiedemann-Franz law on PbTe. *Physical Review B*, 81(16):165203, 2010.

[37] J. Bardeen and W. Shockley. Deformation potentials and mobilities in non-polar crystals. *Physical Review*, 80(1):72, 1950.

[38] S. Bruzzone and G. Fiori. Ab initio simulations of deformation potentials and electron mobility in chemically modified graphene and two-dimensional hexagonal boron-nitride. *Applied Physics Letters*, 99(22):222108, 2011.

[39] C. Van de Walle and R. Martin. Absolute deformation potentials: Formulation and ab initio calculations for semiconductors. *Physical review letters*, 62(17):2028, 1989.

[40] R. Hill. The elastic behaviour of a crystalline aggregate. *Proceedings of the Physical Society. Section A*, 65(5):349, 1952.

[41] P. Watt. Hashin-shtrikman bounds on the effective elastic moduli of polycrystals with orthorhombic symmetry. *Journal of Applied Physics*, 50(10):6290–6295, 1979.

[42] A. Zevalkink, J. Snyder *et al.* Thermoelectric properties of Sr_3GaSb_3 – a chain-forming Zintl compound. *Energy & Environmental Science*, 5(10):9121–9128, 2012.

[43] A. Zevalkink, J. Swallow, and J. Snyder. Thermoelectric properties of Mn-doped $Ca_5Al_2Sb_6$. *Journal of electronic materials*, 41(5):813–818, 2012.

[44] O. Anderson. A simplified method for calculating the debye temperature from elastic constants. *Journal of Physics and Chemistry of Solids*, 24(7):909–917, 1963.

[45] D. Cahill and R. Pohl. Lattice vibrations and heat transport in crystals and glasses. *Annual review of physical chemistry*, 39(1):93–121, 1988.

[46] J. Feng, R. Zhou *et al.* Stability, thermal and mechanical properties of PtxAly compounds. *Materials & Design*, 32(6):3231–3239, 2011.

[47] A. Kachmar. PhD thesis : Etude par la théorie de la fonctionnelle de la densité et par la dynamique moléculaire Car-Parrinello des mécanismes de synthèse et d'isomérisation de nanomatériaux à base de polyoxométallates fonctionnalisés. *Strasbourg 1*, 2008.

[48] W. Kohn and L. J. Sham. Self-consistent equations including exchange and correlation effects. *Physical Review*, 140(4A):A1133, 1965.

[49] J. Perdew, K. Burke, and M. Ernzerhof. Generalized Gradient Approximation made simple. *Physical Review Letters*, 77(18):3865, 1996.

Appendix A

Density functional theory

Here below is a more comprehensive presentation about the density functional theory (DFT) to complete the short introduction given in Chapter 2. The theoretical foundations of this first-principle calculation technique method are presented. This appendix is directly inspired by Refs. [17, 18, 47].

Quantum description

Schrödinger equation

The fundamental equation describing the quantum state of a system with multiple nuclei and electrons is established by Schrödinger equation:

$$\hat{H}\Psi = \left[-\sum_{i}^{N} \frac{\hbar^2}{2m}\nabla_i^2 - \sum_{I}^{A} \frac{\hbar^2}{2M}\nabla_I^2 - \sum_{i,I} \frac{Z_I e^2}{|\vec{r}_i - \vec{R}_I|} + \sum_{i<j} \frac{e^2}{|\vec{r}_i - \vec{r}_j|} + \sum_{I<J} \frac{Z_I Z_J e^2}{|\vec{R}_I - \vec{R}_J|} \right] \Psi = E\Psi \tag{A.1}$$

where $\hat{H}$ is the molecular Hamiltonian and Ψ is the wave function. The first two terms of the Hamiltonian are respectively the kinetic energy operators of the N electrons (indexed i) and of the A atomic nuclei (indexed I). The other three terms represent the different interaction potentials - electron-nucleus, electron-electron and nucleus-nucleus interactions.

The Schrödinger equation must be simplified to be solved analytically. Born and Oppenheimer suggested the following approximation: the position of atomic nuclei is considered fixed. This approximation is justified by the weight ratio between the particles constituting the nucleus (protons and neutrons) and electrons. The kinetic energy of atomic nuclei can therefore be neglected and the interaction term between them considered as a constant (denoted by E_{II}). This approximation leads to following equation:

$$\hat{H}\Psi = \left[-\sum_{i}^{N} \frac{\hbar^2}{2m}\nabla_i^2 - \sum_{i,I} \frac{Z_I e^2}{|\vec{r}_i - \vec{R}_I|} + \sum_{i<j} \frac{e^2}{|\vec{r}_i - \vec{r}_j|} + E_{II} \right] \Psi = E\Psi \tag{A.2}$$

One can simplify the notation by introducing specific notations.
The kinetic energy operator:

$$\hat{T} = -\sum_{i}^{N} \frac{\hbar^2}{2m}\nabla_i^2 \tag{A.3}$$

The external potential felt by electrons:

$$\hat{V}_{Ne} = -\sum_{i,I} \frac{Z_I e^2}{|\vec{r}_i - \vec{R}_I|} \tag{A.4}$$

The potential of electron-electron interaction:

$$\hat{V}_{ee} = \sum_{i<j} \frac{e^2}{|\vec{r}_i - \vec{r}_j|} \tag{A.5}$$

The equation can then be reformulated in a clearer form:

$$\hat{H}\Psi = [\hat{T} + \hat{V}_{Ne} + \hat{V}_{ee} + E_{II}]\Psi = E\Psi \tag{A.6}$$

Many methods have been developed to solve the multielectronic Schrödinger equation, e.g. the description of the wave function as a determinant of Slater like in the Hartree-Fock method. The DFT provides an alternative method by considering as basic quantity for the description of the system its electronic density.

Electronic density

The probability to find an electron among N electrons of the system in a volume element $d\vec{r}$ centered on the position $\vec{r}$ is expressed as

$$n(r)d\vec{r} \tag{A.7}$$

where $n(r)$ is the density of electron probability, defined as

$$n(\vec{r}) = N \int |\Psi(\vec{r}_1 s_1, \vec{r}_2 s_2, \ldots, \vec{r}_N s_N)|^2 ds_1 d\vec{r_1} ds_2 d\vec{r_2} \ldots ds_N d\vec{r_N} \tag{A.8}$$

The density probability has mainly two important properties:

$$n(\vec{r} \to \infty) = 0 \tag{A.9}$$

$$\int n(\vec{r}) d\vec{r} = N \tag{A.10}$$

Hohenberg and Kohn theorems

Two theorems were proposed by Hohenberg and Kohn [24] :

1. Theorem 1: « For a particle system interacting with an external potential $V_{Ne}(r)$, this potential is determined, to a constant, by the density $n_0(r)$ of the particle in its ground state ». This means that all system properties can be completely determined if the electron density of the ground state is known.

2. Theorem 2: « There is a universal functional $E[n]$ expressing the energy in function of the electron density $n(r)$, valid for any external potential $V_{Ne}(r)$. For each $V_{Ne}(r)$ in particular, the energy of the ground state of the system is the value that minimizes this functional. The corresponding density $n(r)$ is the exact density $n_0(r)$ of the ground state ». The energy appears as a density functional, and as for any external potential, the density that minimizes this functional is the exact density of the ground state.

$$E = F[n] \tag{A.11}$$

It is then possible to rewrite the Schrödinger equation (A.6) as a density functional:

$$E = T[n] + V_{Ne}[n] + V_{ee}[n] \tag{A.12}$$

According to these theorems, the DFT method easily determines the energy of the ground state for a given external potential if the shape of the functional is known. The problem then is the formulation of functional $F[n]$, and in particular the expression of the kinetic energy $T[n]$.

Kohn and Sham ansatz

The kinetic energy of an electron gas in interaction is unknown. Kohn and Sham proposed an ansatz [48] to overcome this difficulty. The idea is to replace the system of interacting electrons, impossible to solve analytically, with a problem of independent electrons moving in an external potential.

The Hohenberg and Kohn total energy functional, described as

$$E_{HK}[n] = F[n] + \int V(r) n(r) dr \tag{A.13}$$

can be rewritten as follows:

$$E_S[n] = T_S[n] + V_S \tag{A.14}$$

where $T_S[n]$ is the kinetic energy of the electrons without interaction and $V_S[n]$ the potential where electrons move. The electron density $n_S(r)$ is strictly equal to the density shown in the functional defined by Hohenberg and Kohn if the external potential $V_S[n]$ is defined as

$$V_S = V_{Ne} + V_{ee} + (T - T_S) \tag{A.15}$$

One can now define a one-electron Hamiltonian and write the corresponding Kohn-Sham equations, in order to solve them analytically:

$$\left[-\frac{\hbar^2}{2m}\nabla^2 + V_S(\vec{r})\right]\phi_i(\vec{r}) = \epsilon_i\phi_i(\vec{r}) \tag{A.16}$$

The resolution of Kohn-Sham equations helps to determine the orbitals $\phi_i(\vec{r})$ that will reproduce the electron density of the original multielectronic system according the following definition:

$$n(\vec{r}) \overset{\text{def}}{=} n_S(\vec{r}) = \sum_i^N |\phi_i(\vec{r})|^2 \tag{A.17}$$

The effective one-electron potential that appears in the equation can be expressed more fully as

$$V_S = V_{Ne} + \int \frac{n_S(\vec{r})n_S(\vec{r}')}{|\vec{r} - \vec{r}'|}\mathrm{d}^3r' + V_{\mathrm{XC}}[n_S(\vec{r})] \tag{A.18}$$

The first term is the external potential created by the nuclei. The second, called Hartree potential, expresses the classical Coulomb interaction between electron pair. The last term is the exchange-correlation potential and contains, besides the exchange and electron correlation, corrections to the kinetic energy.

The Kohn and Sham ansatz finally allows one to achieve a set of one-electron Schrödinger equations known as Kohn-Sham equations:

$$\Big[-\frac{\nabla^2}{2m} + V_{Ne} + V_{Ha} + V_{XC}\Big]\phi_i = \epsilon_i\phi_i \tag{A.19}$$

Exchange-correlation potentials

At the stage of Kohn-Sham equations, the DFT is an exact theory (apart from the Born-Oppenheimer approximation) considering the electron density that minimizes the total energy is exactly the density of the system of N interacting electrons. However, two approximations are finally made. First of all, one has to choose the basic functions and the reduced number of electrons considered in the calculations. Different types of pseudopotentials can be used to this end. Secondly, the exchange-correlation potential V_{XC} is not exactly known: the choice of an approximated function is the main flaw of the DFT in the Kohn-Sham approach. Two main approximations of this potential are the local density approximation (LDA) [48] and generalized gradient approximation (GGA) [49]. Other derived methods, based on a non-local approach, also exist. The LDA was used in this thesis.

Local density approximation

The approach of the local density is based on the uniform electron gas model and is the simplest approach to express the exchange-correlation energy. The total energy of the system is a density functional and is expressed as

$$E_{XC}[n] = \int n(\vec{r})\varepsilon_{XC}[n]dr \tag{A.20}$$

where $\varepsilon_{XC}[n]$ refers to the exchange-correlation energy for a particle of a homogeneous electron gas. The function $\varepsilon_{XC}[n]$ can be decomposed into an exchange contribution $\varepsilon_X[n]$ and a correlation contribution $\varepsilon_C[n]$:

$$\varepsilon_{XC}[n] = \varepsilon_X[n] + \varepsilon_C[n] \tag{A.21}$$

The contribution from the electronic exchange in the approximation of local density is known and taken from the exchange energy functional formulated by Dirac:

$$\varepsilon_X[n] = -\frac{3}{4}(\frac{3}{\pi})^{1/3} \int n(\vec{r})^{4/3} d^3r \tag{A.22}$$

Although it is a fairly simple approach conceptually, the LDA functional still provides good results. An error compensation can explain the relative success of the LDA method. Indeed it tends to underestimate the exchange energy as it overestimates the correlation energy. In the end, the LDA allows one to reach pretty correct values for the exchange-correlation energy. The energy of the band gap will be underestimated which is a specific problem in the DFT.

Appendix B

Structural relaxation results

Convergence studies

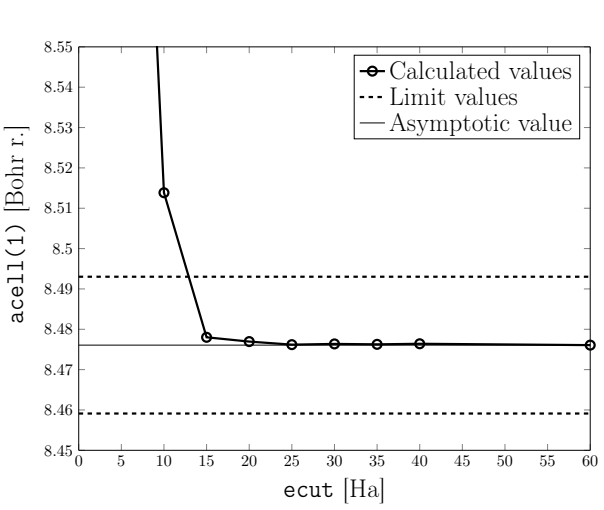

(a)

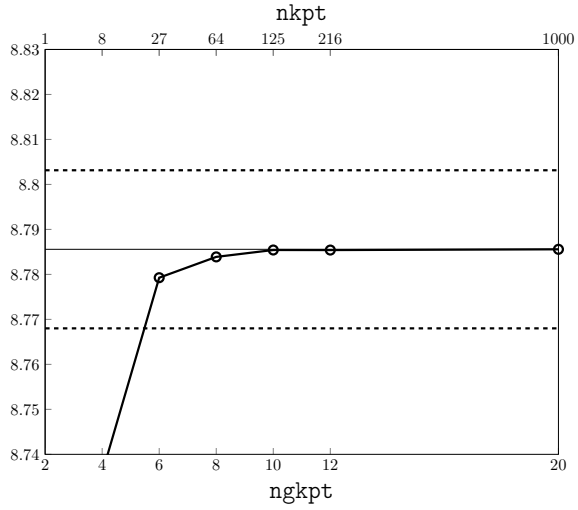

(b)

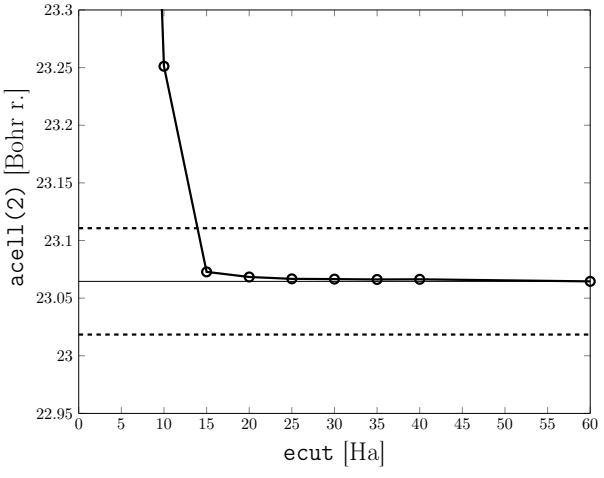

(c)

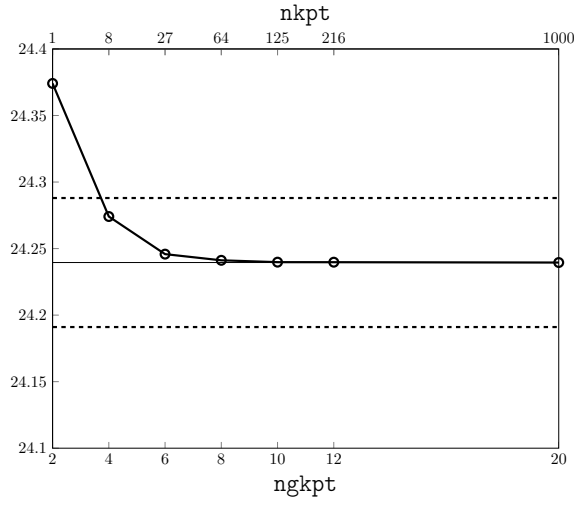

(d)

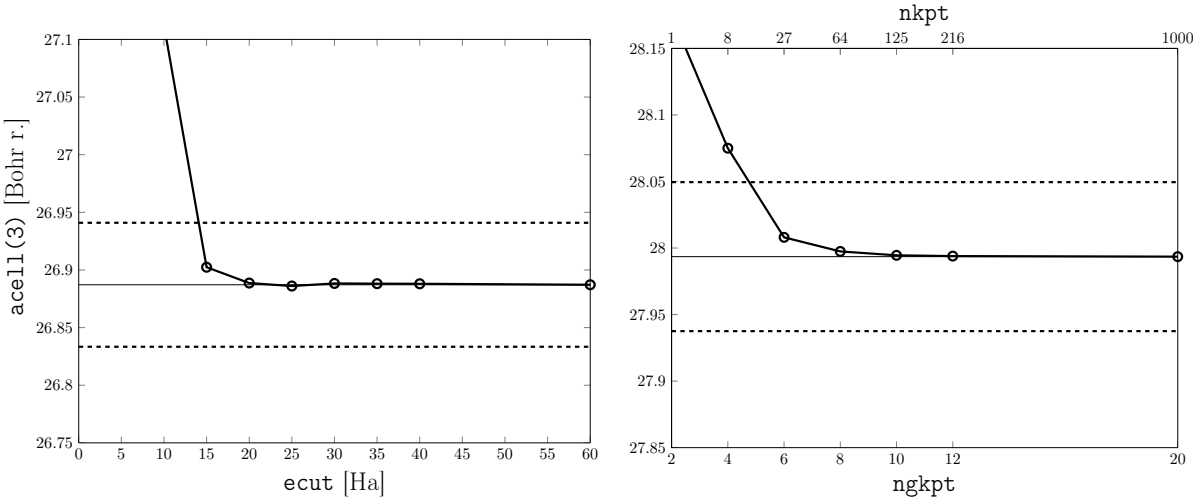

(e) (f)

Figure B.1: Convergence of $Ca_5Al_2Sb_6$ lattice constants `acell(1)-(2)-(3)` in cut-off energy `ecut` (a)-(c)-(e) and in number of k-points `ngkpt` (b)-(d)-(f). Asymptotic values were calculated with `ecut` 20 Ha and a 20×20×20 grid.

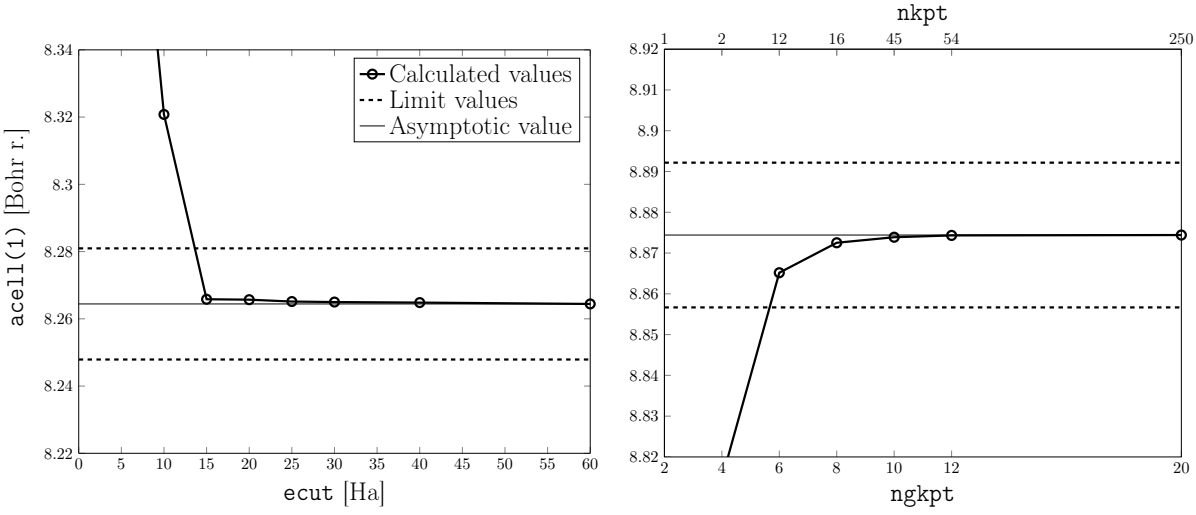

(a) (b)

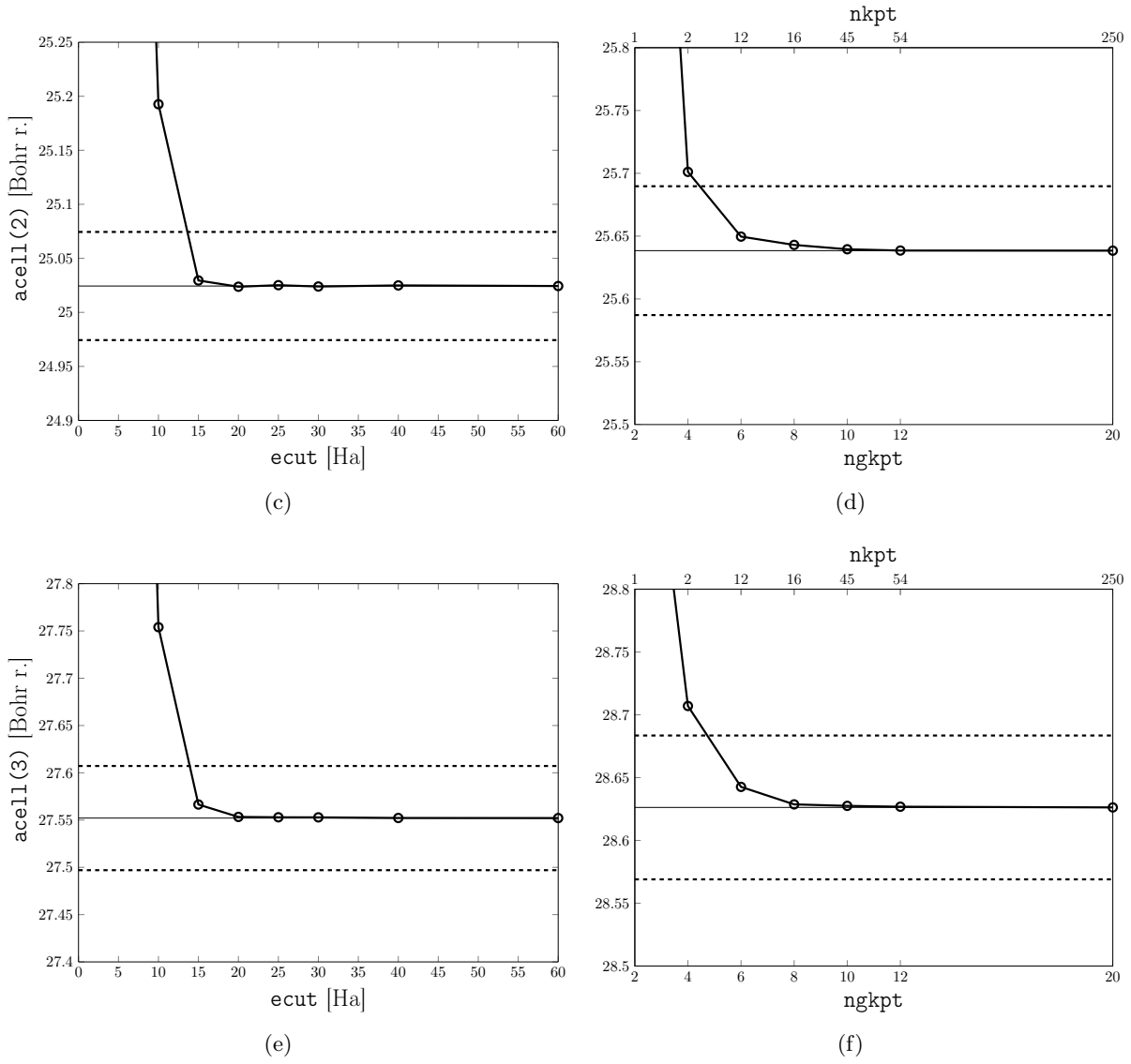

Figure B.2: Convergence of Ca_3AlSb_3 lattice constants `acell(1)-(2)-(3)` in cut-off energy `ecut` (a)-(c)-(e) and in number of k-points `ngkpt` (b)-(d)-(f). Asymptotic values were calculated with `ecut` 20 Ha and a 20×20×20 grid.

Atomic positions

Table B.1: Positions of atoms of $Ca_5Al_2Sb_6$ in reduced coordinates after a relaxation under the BFGS algorithm.

Unit cell atom	Position vector in reduced coord. (`xred`)		
Ca_1	0.500000	0.907436	0.252328
Ca_2	0.500000	0.095637	0.747671
Ca_3	0.500000	0.173088	0.013982
Ca_4	0.500000	0.673088	0.485016
Ca_5	0.500000	0.595637	0.752328
Ca_6	0.500000	-1.38E-17	0.500000
Ca_7	0.500000	0.407436	0.247671
Ca_8	0.500000	0.326911	0.513983
Ca_9	0.500000	0.826911	0.986016
Ca_{10}	0.500000	0.500000	2.77E-17
Al_1	0.000000	0.330656	0.711204
Al_2	0.000000	0.830656	0.788795
Al_3	0.000000	0.169343	0.211204
Al_4	0.000000	0.669343	0.288795
Sb_1	0.000000	0.156322	0.593484
Sb_2	0.000000	0.523764	0.600399
Sb_3	0.500000	0.339060	0.820920
Sb_4	0.500000	0.839060	0.679079
Sb_5	0.000000	0.476235	0.399960
Sb_6	0.500000	0.160939	0.320920
Sb_7	0.000000	0.976235	0.100039
Sb_8	0.000000	0.656322	0.906515
Sb_9	0.000000	0.843677	0.406515
Sb_{10}	0.000000	0.343677	0.093484
Sb_{11}	0.000000	0.023764	0.899960
Sb_{12}	0.500000	0.660939	0.179079

Table B.2: Positions of atoms of Ca_3AlSb_3 in reduced coordinates after a relaxation under the BFGS algorithm.

Unit cell atom	Position vector in reduced coord. (`xred`)		
Ca_1	0.250000	0.558039	0.611758
Ca_2	0.750000	0.441960	0.388241
Ca_3	0.250000	0.058039	0.888241
Ca_4	0.750000	0.941960	0.111758
Ca_5	0.250000	0.350351	0.430472
Ca_6	0.750000	0.649648	0.995695
Ca_7	0.250000	0.850351	0.495695
Ca_8	0.750000	0.149648	0.504304
Ca_9	0.750000	0.728525	0.279326
Ca_{10}	0.250000	0.271474	0.720673
Ca_{11}	0.750000	0.228525	0.220673
Ca_{12}	0.250000	0.771474	0.779326
Al_1	0.250000	0.568718	0.203449
Al_2	0.750000	0.431281	0.796550
Al_3	0.250000	0.0687184	0.296550
Al_4	0.750000	0.931281	0.703449
Sb_1	0.250000	0.756552	0.118393
Sb_2	0.750000	0.243447	0.881606
Sb_3	0.250000	0.256552	0.381606
Sb_4	0.750000	0.743447	0.618393
Sb_5	0.250000	0.614609	0.390314
Sb_6	0.750000	0.385390	0.609685
Sb_7	0.250000	0.114609	0.109685
Sb_8	0.750000	0.885390	0.890314
Sb_9	0.250000	0.539088	0.850219
Sb_{10}	0.750000	0.460911	0.149780
Sb_{11}	0.250000	0.390887	0.649780
Sb_{12}	0.750000	0.960911	0.350219

Appendix C

Experimental fitting of electrical resistivities

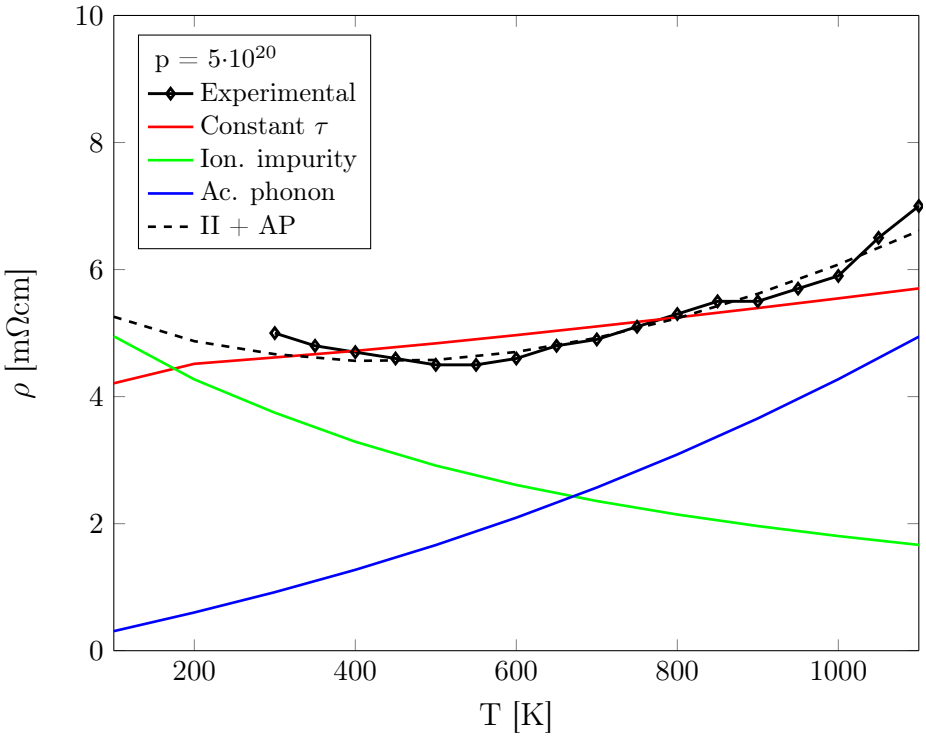

Figure C.1: Experimental fitting of the electrical resistivity of $Ca_5Al_2Sb_6$ at a $5{\cdot}10^{20}$ cm^{-3} doping level based on ionized impurity and acoustic phonon scattering mechanisms.

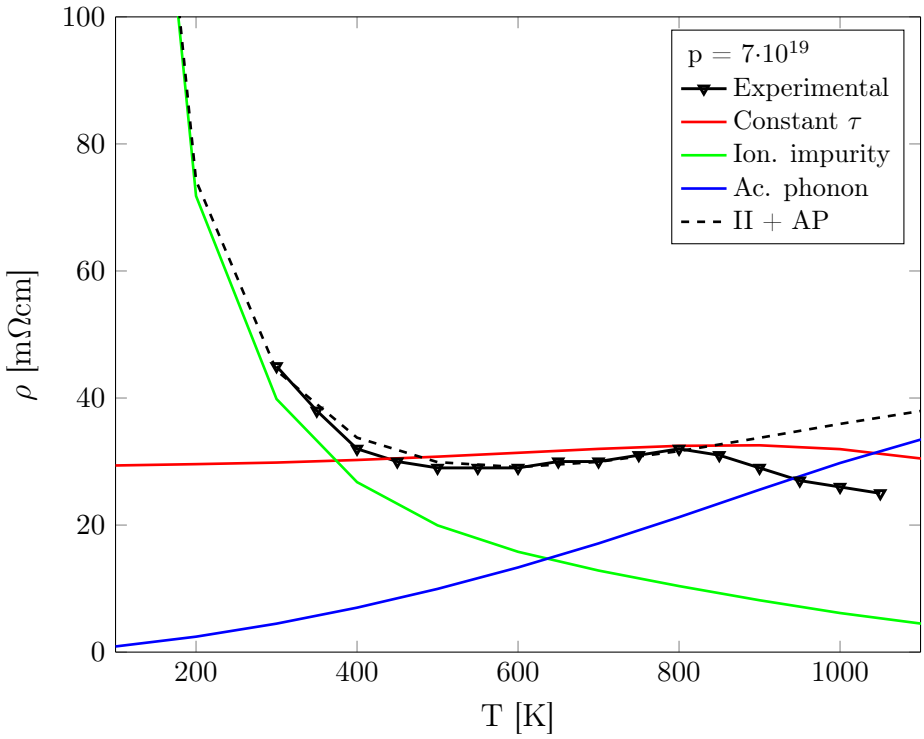

Figure C.2: Experimental fitting of the electrical resistivity of $Ca_5Al_2Sb_6$ at a $7{\cdot}10^{19}$ cm^{-3} doping level based on ionized impurity and acoustic phonon scattering mechanisms.

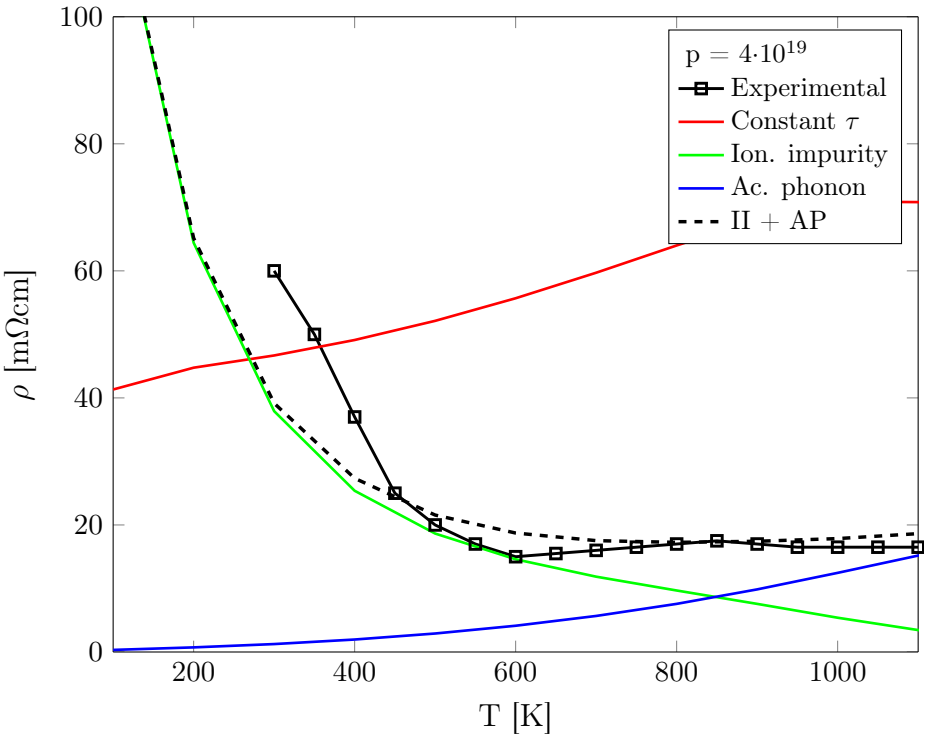

Figure C.3: Experimental fitting of the electrical resistivity of Ca_3AlSb_3 at a $4{\cdot}10^{19}$ cm^{-3} doping level based on ionized impurity and acoustic phonon scattering mechanisms.

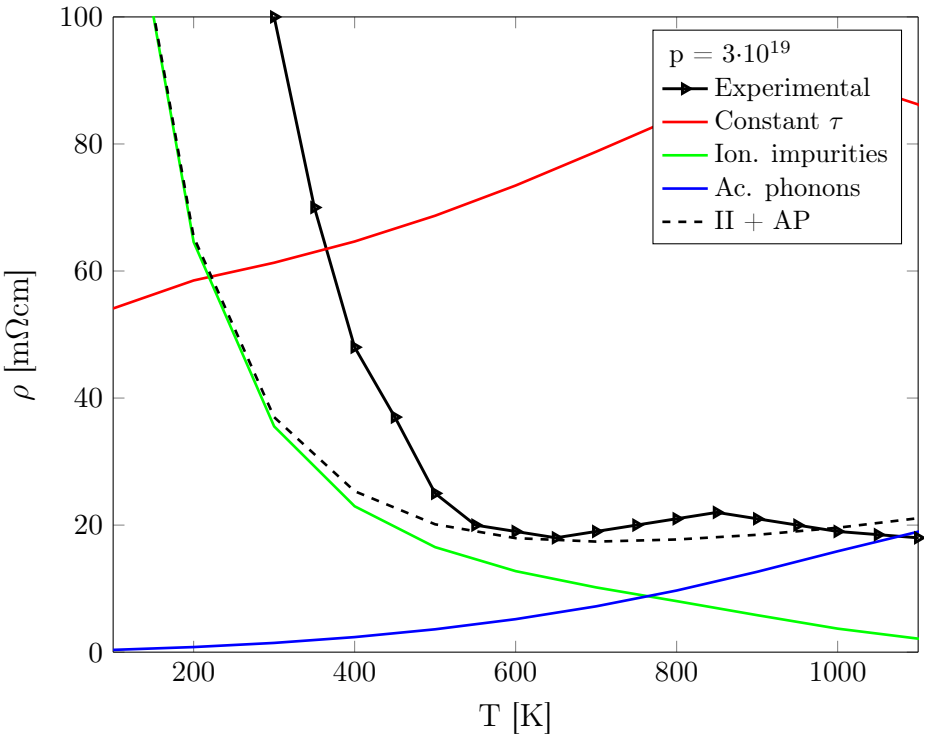

Figure C.4: Experimental fitting of the electrical resistivity of Ca_3AlSb_3 at a $3{\cdot}10^{19}$ cm^{-3} doping level based on ionized impurity and acoustic phonon scattering mechanisms.

Appendix D

Strain response-function convergence studies

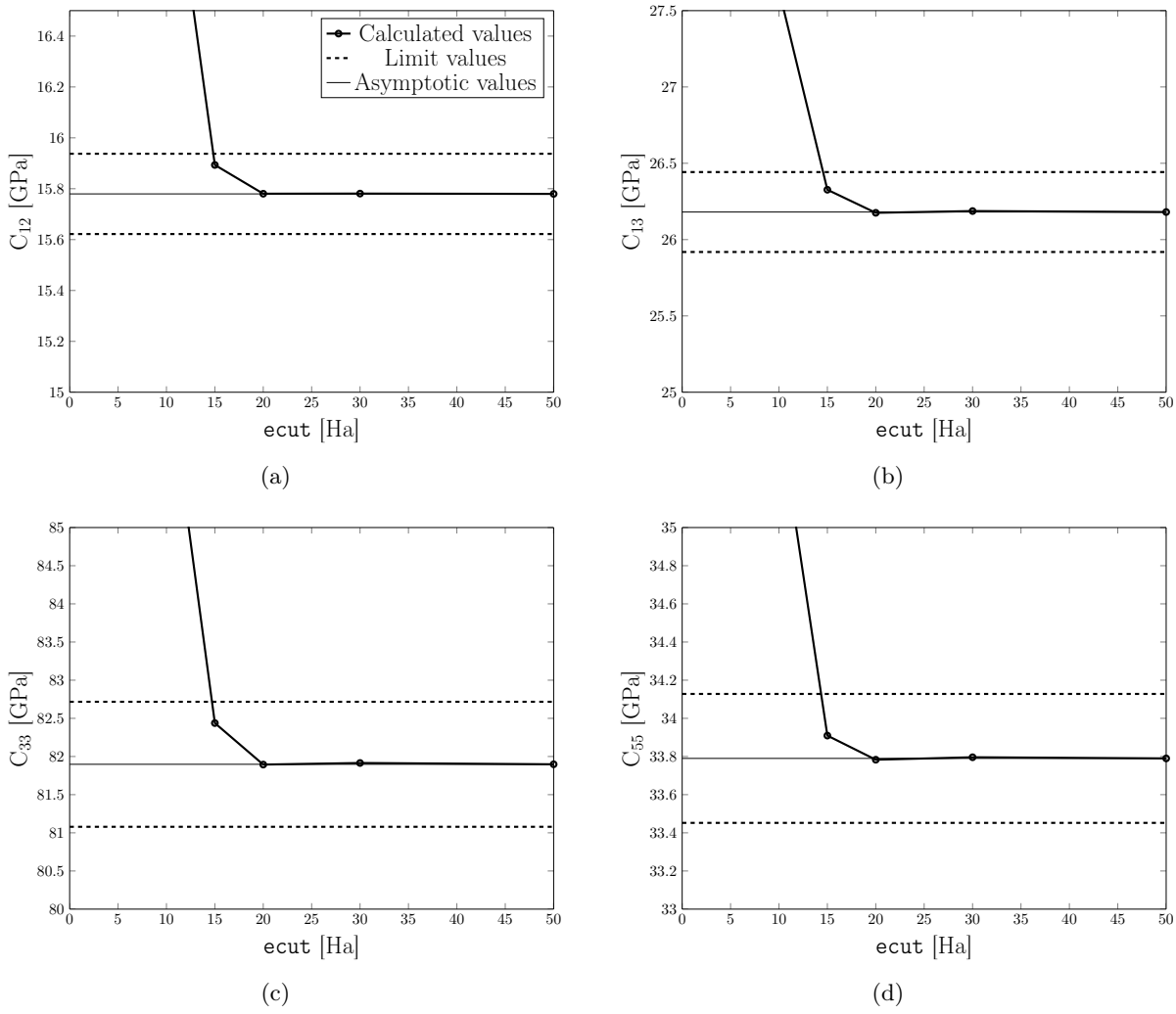

Figure D.1: Convergence of some of the $Ca_5Al_2Sb_6$ elastic constants in cut-off energy. Asymptotic values were calculated with cut-off energy of 50 Ha.

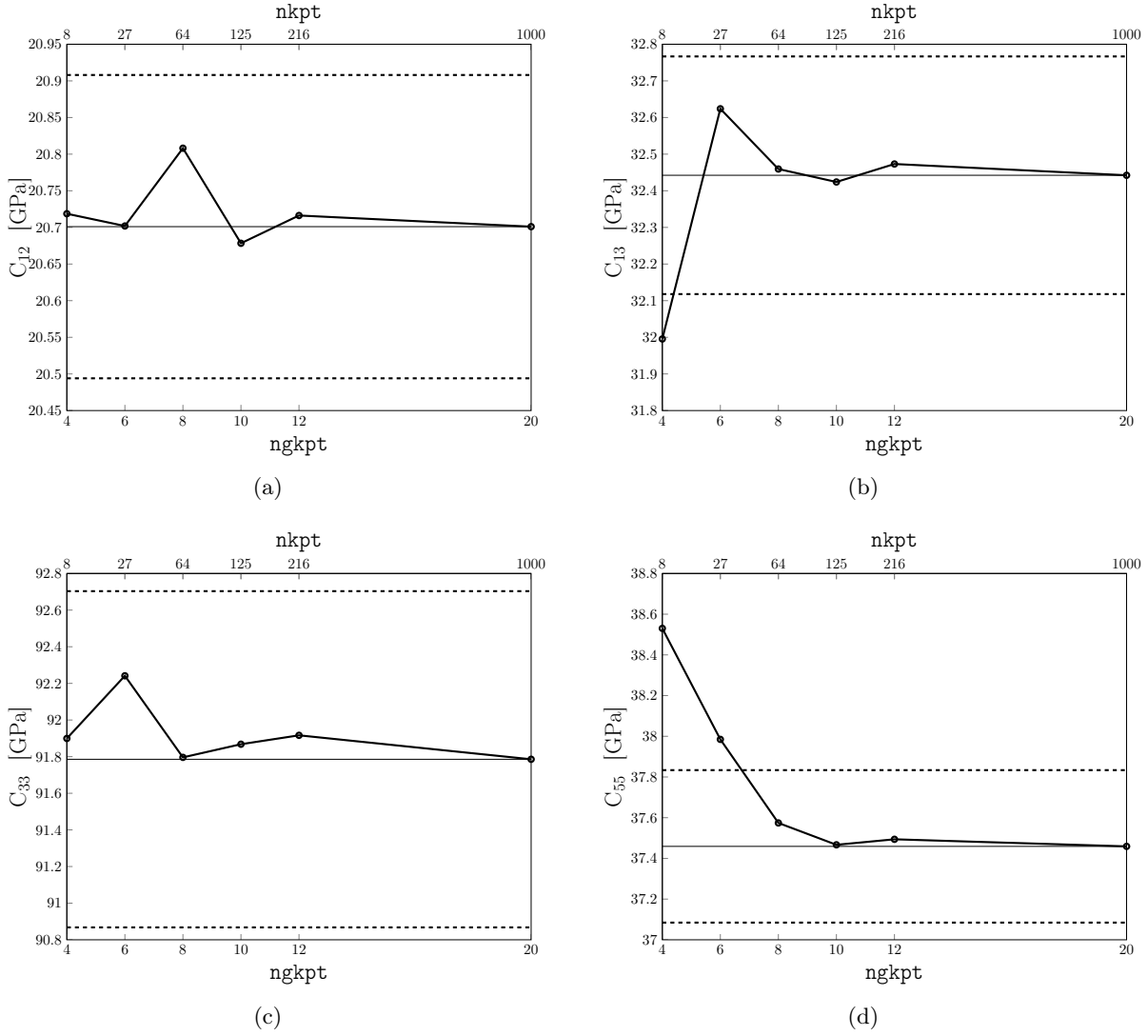

Figure D.2: Convergence of some of the $Ca_5Al_2Sb_6$ elastic constants in number of k-points. Asymptotic values were calculated with a 20×20×20 grid.

Appendix E

Anisotropy of the transport properties in Ca_3AlSb_3

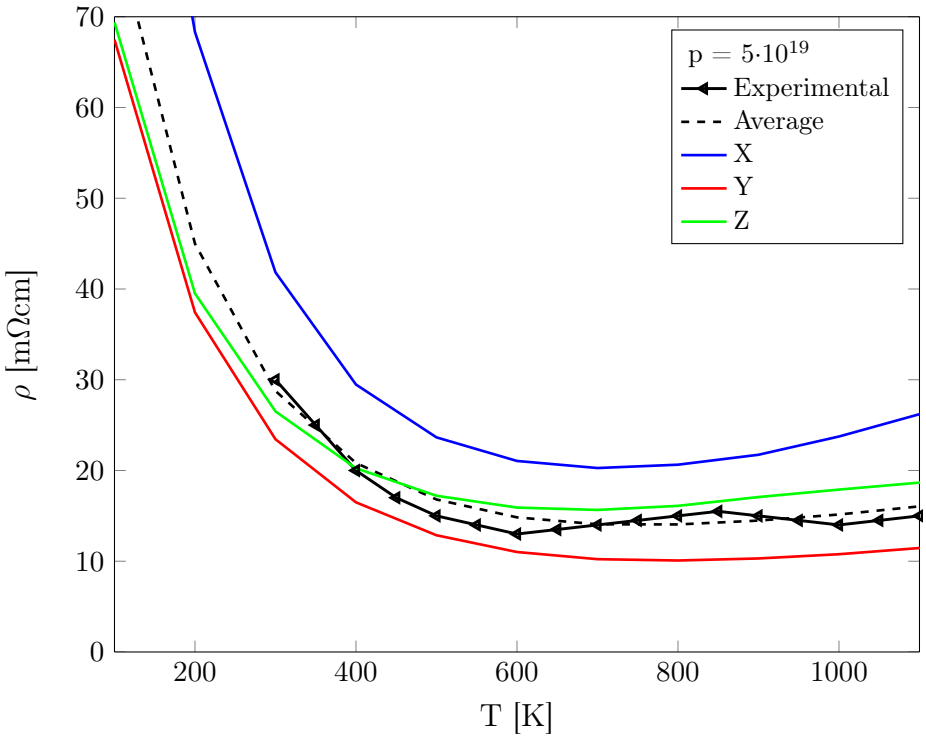

Figure E.1: Anisotropy of the electrical resistivity of Ca_3AlSb_3 based on ionized impurity and acoustic phonon scattering mechanisms.

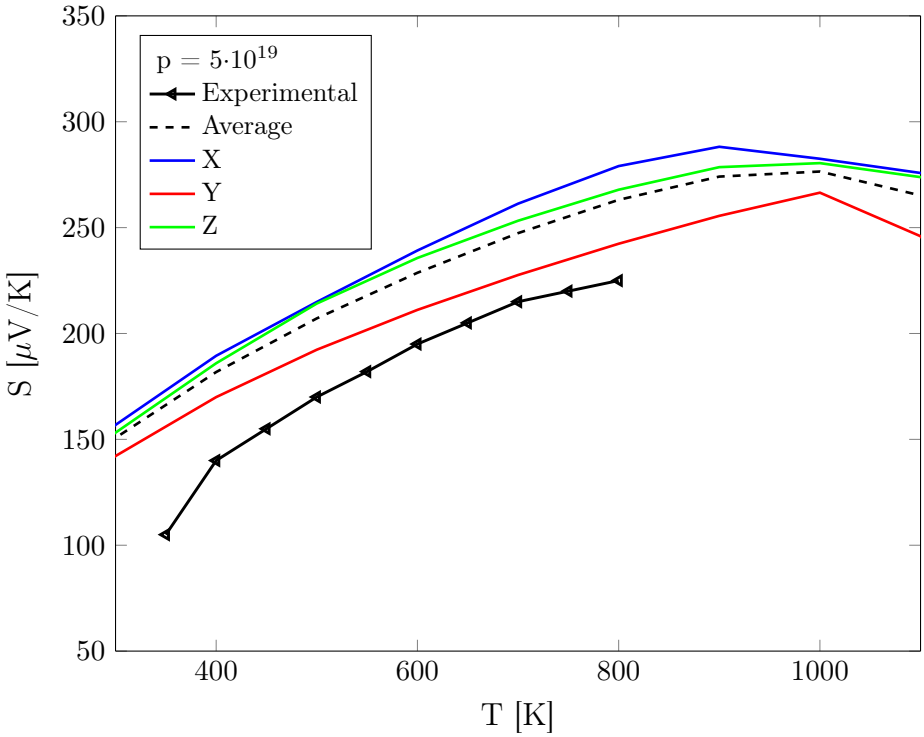

Figure E.2: Anisotropy of the Seebeck coefficient of Ca_3AlSb_3.

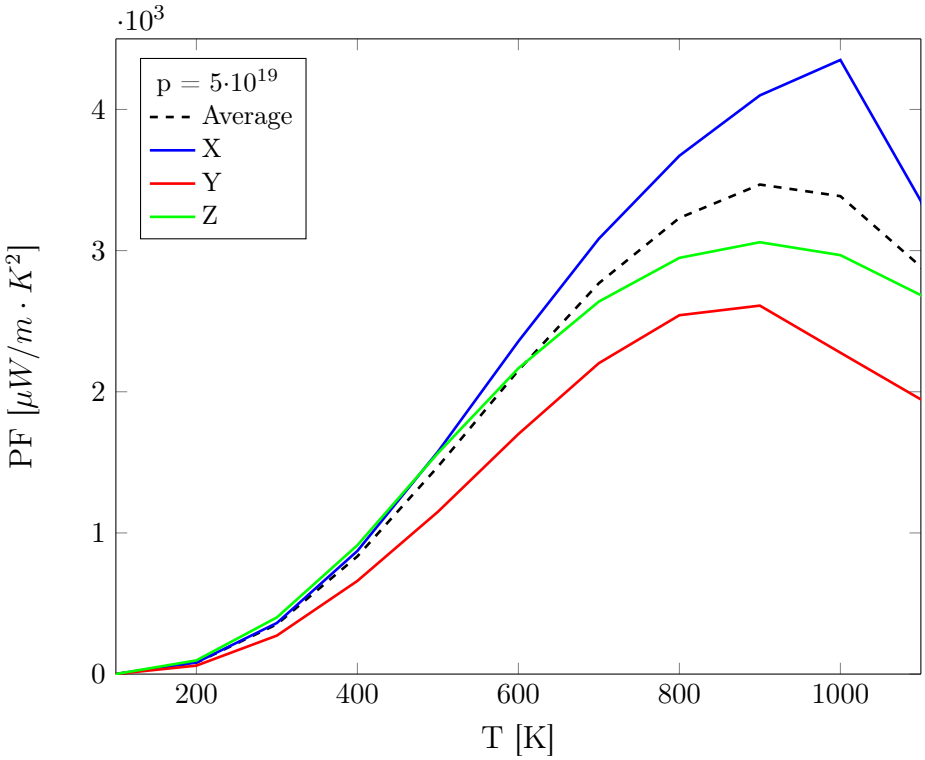

Figure E.3: Anisotropy of the power factor of Ca_3AlSb_3.

Rue Archimède, 1 bte L6.11.01, 1348 Louvain-la-Neuve **www.uclouvain.be/epl**